Simultaneous Measurement of Fluctuating Velocity and Pressure in Turbulent Free Shear Flows

March 2009

Yoshitsugu Naka

School of Science for Open and Environmental Systems

Graduate School of Science and Technology
Keio University

Acknowledgements

This research has been financially supported by Japan Society for the Promotion of Science (JSPS), Grant-in-Aid for JSPS Fellows, 19·5711, 2007.

I am truly grateful to my supervisor Professor Shinnosuke Obi. Since I was an undergraduate student, he has always encouraged me to take a challenging step forward. Thanks to his intuitive and stimulating advice, I have been able to keep myself concentrate on this study. I deeply appreciate Professor Kuniyasu Ogawa, Professor Koichi Hishida and Professor Satoshi Honda for invaluable discussions on the present thesis. I would like to show my gratitude to Professor Koji Fukagata for fruitful discussions on various topics especially the numerical simulation, and to Professor Shigeaki Masuda for teaching me nice tricks of experiments. In addition, I have a great sense of appreciation to Professor Kuniaki Toyoda of Hokkaido Institute of Technology and Professor Yoshiyuki Tsuji of Nagoya University for giving me many substantial advices for the fluctuating pressure measurement every time we meet in conferences.

I would like to thank the members of Masuda-Obi-Fukagata laboratories for making my research life enjoyable. In particular, I would like to show my deep gratitude to Takeshi Omori, Suguru Azegami and Takuya Kawata who I spent much time in front of the wind-tunnel together and to Rio Yokota for discussions in any kinds of topics with a lot of fun.

Of course, I do appreciate to my family for supporting me all the time.

Abstract

The scope of this thesis is to establish the technique for the simultaneous measurement of fluctuating velocity and pressure and to investigate the relationship between the turbulent vortical structure and the statistical characteristics including the pressure fluctuation. The measurements have been performed in the turbulent mixing layer and the wing-tip vortex as the test cases for simple and complex free shear flows, respectively.

Two different combinations of probes are developed: either the total pressure probe (TP-probe) or the static pressure probe (SP-probe) is combined with the X-type hot-wire probe (X-probe). Fundamental performances of these techniques have been investigated.

In the turbulent mixing layer, the results obtained by the SP-probe show good agreement with the available data of Direct Numerical Simulation in the downstream region where the mixing layer achieves the self-similar state. The pressure-diffusion terms evaluated in the upstream region where the distinct vortical structure is found exhibit the departure from the analogous relationship with the turbulent-diffusion unlikely in the downstream location. The spatial resolution of the technique using the SP- and X-probes is improved by using the TP- and X-probes. The results obtained by the TP-probe show satisfactory agreement with those by the SP-probe.

In the wing-tip vortex, it is shown that using the TP-probe can reduce the probe interference compared to the use of the SP-probe. The present results indicate that the meandering of the vortex takes place, and the relationship between the turbulent- and pressure-diffusion terms are related to the unsteady motion of the wing-tip vortex.

Contents

List of Figures

List of Tables

Nomenclature

Roman Symbols

a_0	speed of sound
b	span of the wing
C	electric capacitance of the condenser microphone
c	chord length of the wing
C_{ij}, D^p_{ij}, D^t_{ij}, D^v_{ij}, P_{ij}, ϕ_{ij}, ε_{ij}	convection, pressure-diffusion, turbulent-diffusion, viscous diffusion, production, re-distribution, dissipation terms of RSTE
C_k, D^p_k, D^t_k, D^v_k, P_k, ε_k	terms in the transport equation of turbulent kinetic energy
C_p	pressure coefficient
C_{xy}, Q_{xy}	real and imaginary parts of the cross spectra
c_v, c_p	specific heat at constant volume / pressure
D	diameter of the TP-probe
f	frequency
g	gravity constant
G_{xx}, G_{yy}	auto spectra
G_{xy}	cross spectra
h	arbitrary physical quantity

i, j	$\left(= \sqrt{-1}\right)$ imaginary unit
J_n	Bessel function
k	turbulent kinetic energy
k_p	polytropic constant
L	tube length
$\mathcal{L}$	integral length scale
L_x, L_y, L_z	spatial resolution of the simultaneous measurement of velocity and pressure
N	number of samples
p, p_t	static and total pressure
p_1, p_2	measured pressure
p_A, p_B	pressure fluctuation at the tip of the pressure probe and at the place of diaphragm A and B
Pr	$\left(= \frac{\mu g c_p}{\lambda}\right)$ Prandtl number
p_s	pressure signal
P_t	time-averaged total pressure
P_{t0}	time-averaged total pressure at zero angle of attack
R	resistance of the condenser microphone circuit
R	tube radius
R_0	gas constant
$\mathbf{r_{dx}}$	cross-correlation vector
Re_T	turbulence Reynolds number

Re_c	$(= U_\infty c/\nu)$ Reynolds number based on the free stream velocity and the chord length
$R_{uu}, R_{uv}, R_{up}, R_{vp}$	correlation coefficient
$\mathbf{R_x}$	auto-correlation matrix
S	expansion factor of free shear flows
s	coordinate along with streamline
St	$(= fd/U_s)$ Strouhal number
T	temperature
t	time
Tu_f	free stream turbulence intensity
U, V, W	time-averaged velocity component in streamwise, transverse and spanwise directions
u, v, w	fluctuating velocity component in streamwise, transverse and spanwise directions
U_c	$\left(= \frac{U_h+U_l}{2}\right)$ convection velocity
U_i	time-averaged velocity
U_∞	free stream velocity
$\overline{u_i u_j}$	the Reynolds stress
U_s	$(= U_h - U_l)$ free stream velocity difference
$\overline{u^2}, \overline{v^2}, \overline{w^2}, \overline{uv}, \overline{uw}, \overline{vw}$	the Reynolds stress
v_1, v_2	noise
v_s	velocity component along with streamline
V_t	$(= \pi R^2 L)$ tube volume

V_v	volume of microphone cavity
$\mathbf{w}$	coefficient of Wiener-filter
x, y, z	the Cartesian Coordinate in streamwise, transverse and spanwise directions
x_i	coordinate

Greek Symbols

α	yaw-angle of the pressure probe
β	$\left(= i^{3/2} R \sqrt{\frac{\rho_s \omega}{\mu}}\right)$ shear wave number
δ	thickness of the mixing layer
δ_b	99% thickness of turbulent boundary layer
δ_{ij}	Kronecker delta
Δt	sampling interval
Δx	streamwise distance between probes
Δz	center to center distance between probes
η	$(= y/\theta)$ non-dimensional transverse coordinate
γ	$(= \frac{c_p}{c_v})$ specific heat ratio
γ_c	coherence
Γ	circulation
λ	thermal conductivity
μ	fluid viscosity
ν	fluid kinematic viscosity
ω	$(= 2\pi f)$ angular frequency
Ω_x	streamwise vorticity component

ϕ_p	phase
ρ	fluid density
σ	dimensionless increase in microphone volume due to diaphragm deflection normalized by V_v
θ	momentum thickness of the turbulent mixing layer at $x = 150$ mm
θ_d	phase-lag due to the electric circuit of condenser microphone

Superscripts

$()^e$	estimated value
$\hat{}$	indicating instantaneous value
$\tilde{}$	indicating small perturbation

Subscripts

$()_c$	quantities at the wing-tip vortex center
$()_h$	quantities in high speed side
$()_{ijk}$	indexing subscripts
$()_l$	quantities in low speed side
$()_s$	mean quantity

Acronyms

CDS	Central Differencing Scheme
CTA	Constant Temperature Anemometer
DNS	Direct Numerical Simulation
FST	Free Stream Turbulence
HWA	Hot-Wire Anemometer

HWP	Hot-Wire Probe
K-H	Kelvin-Helmholtz
LDV	Laser Doppler Velocimetry
LES	Large Eddy Simulation
MEMS	Micro-Electro Mechanical Systems
PDF	probability density function
PIV	Particle Image Velocimetry
PSD	Power Spectral Density
PSP	Pressure Sensitive Paint
RANS	Reynolds Averaged Navier-Stokes
RSM	Reynolds Stress Model
SP-probe	Static Pressure probe
TP-probe	Total Pressure probe
UDS	Upwind Differencing Scheme

Chapter 1

Introduction

1.1 Background

Turbulent flows are ubiquitous in our life. Toward understanding, prediction and control, turbulent flow phenomena have been one of challenging research targets for more than 100 years. Turbulent flows consist of various scales of vortices, which are large-scale coherent vortices, and a large number of fine-scale eddies. The interactions of these variety scales of vortices are essentially non-linear phenomena and this is one reason that turbulent flows are difficult to be fully understood. In a quantitative point of view, such vortical motions of turbulent flows create the fluctuating pressure and three components of the fluctuating velocity, and these quantities correlate each other. It is well recognized that the fluctuating pressure and the velocity-pressure correlation reflect the non-local information representing the vortical structures. In a statistical point of view, the correlation of fluctuating velocity and pressure appears in the transport equation of turbulence properties such as the turbulent kinetic energy and the Reynolds stress. The velocity-pressure correlation plays a role of diffusion.

Although the pressure-fluctuation and the velocity-pressure correlation are known as one of important and fundamental characteristics of turbulent flows, the knowledge has been rather limited compared to that of the velocity fluctuation. One main reason is that the appropriate experimental techniques have not been available especially for complex flows. Most of difficulties come from the intrusive nature in measurements of the fluctuating pressure. Simultaneous measurements of fluctuating velocity and pressure in turbulent flows have long been one of most challenging problems in experimental fluid dynamics even though numerous efforts have been devoted to it.

The problems in the current models for prediction of turbulent flows based on the time-averaged momentum equation lie in the representation of the effect of the fluctuating pressure: the treatments of the pressure-related terms, e.g. re-distribution and pressure-diffusion terms, are always troublesome in the framework of the Reynolds Averaged Navier-Stokes (RANS) model. Understanding the physical process of the pressure-related terms is meaningful in view of improving the predictability of turbulent flows using turbulence models. Since no appropriate experimental technique is available, reliable data of the fluctuating pressure and the velocity-pressure correlation have been provided only by Direct Numerical Simulation (DNS). Although DNS can provide the full data of turbulent flows including pressure, its applicability is still restricted relatively low Reynolds number simple geometry flows, and it is difficult to obtain a large number of samples for statistical evaluation especially for spatially developing flows. Hence, complementary experimental investigations of the pressure-related statistics are demanded and it will help to improve the applicability and performance of RANS models.

1.2 Previous work

1.2.1 Statistical theory of the pressure fluctuation and the velocity-pressure correlation

Studies on the characteristics of pressure fluctuations began from the theoretical description of turbulence from a stochastic sense. Statistical theory, which was firstly proposed by Taylor (1935), was developed on the correlation function of the pressure fluctuation and the velocity-pressure correlation under the assumption of an idealized condition, i.e., the homogeneous isotropic turbulence. These theoretical descriptions were well documented in Batchelor (1951) and Hinze (1975). Experimental attempts to confirm these theories were made by Uberoi (1954) and Gylfason et al. (2004) using the fluctuating velocity measured by hot-wire anemometry (HWA). These theories were evaluated by using DNS data (Gotoh and Rogallo, 1999) and statistical characteristics of the fluctuating pressure and the velocity-pressure correlation were investigated by Gotoh and Fukayama (2001) and Gotoh and Nakano (2003). In addition, the applicability of these theories were extended by Alvelius and Johansson (2000) and Yakhot (2003).

Although the knowledge on the statistical theories are useful to understand the fundamental characteristics of turbulence, the application of these statistical theories is still limited in the idealized turbulence, and it is difficult to apply them to practical and complex turbulent flows.

1.2.2 Vortical structure and the statistical characteristics of turbulent shear flows

Quasi-coherent structures of turbulent flows were firstly reported in the boundary layer (Kline et al., 1967) and the turbulent mixing layer (Brown and Roshko, 1974). After these epoch-making discoveries, a great number of contributions have been devoted to the study on coherent vortical structures. Some reviews on this topic are available, for instance, Cantwell (1981), Hussain (1983), Ho and Huerre (1984) and Hussain and Zaman (1985). Here, important articles relating to the present study are picked up in following sections.

1.2.2.1 Turbulent mixing layer

The turbulent mixing layer has been extensively studied for a long time because it is geometrically simple but it contains the essence of turbulence. As Brown and Roshko (1974) firstly visualized, the quasi-coherent structure of vortex is formed in the shear layer due to Kelvin-Helmholtz (K-H) instability. Statistical features of the turbulent mixing layer were investigated by Wygnanski and Fiedler (1970) and Dimotakis and Brown (1976). Dziomba and Fiedler (1985) reported the receptivity of several different periodic excitations on the development of the mixing layer. Huang and Ho (1990) investigated the process of vortex pairing and transition to turbulence. (Bell and Mehta, 1990) reported the effect of inlet boundary layers, i.e., laminar or turbulent. Braud et al. (2004) investigated the effect on the splitter plate thickness, i.e., the effect of the K-H instability on the wake. Tanahashi et al. (2008) performed PIV measurements to capture the structure of coherent fine eddies. The vortical structure was revealed by full data of the flow provided by DNS: Rogers and Moser (1994) performed the DNS of temporally developing turbulent mixing layer, and Wang et al. (2007) investigated the small-scale transition and the structure of the fine eddies.

1.2.2.2 Wing-tip vortex

The wing-tip vortex has also been studied since long time ago from practical demands: the wing-tip vortex causes an induced drag, a long interval time of take-off, hazards for small airplanes and the noise of helicopters.

For turbulence researchers, the wing-tip vortex can be classified as a complex swirling flow formed from the three-dimensional boundary layer on the wing. Theoretically, Batchelor (1964) predicted the excess of the axial velocity on the centerline due to the strong radial pressure gradient developing in the streamwise direction. The development of mean velocity profile in the wing-tip vortex was investigated and the flow visualization was carried out by Chigier and Corsiglia (1971), Orloff (1974), Thompson (1983) and Green and Acosta (1991). Chow et al. (1997) performed the extensive experiment on the flow around a NACA 0012 half-wing. More recently, numerical predictions of the development of the wing-tip vortex was performed by Craft et al. (2006), Revelly et al. (2006) and Uzun et al. (2006).

1.2.2.3 Other turbulent shear flows

Numerous contributions have been devoted to investigate physics of various turbulent shear flows. A common way to characterize turbulent flows is to investigate the statistical features of the flow, e.g. the mean velocity, the Reynolds stress, the power spectra, the balance of the transport equation of turbulence quantities. Recently, the balance of transport equation of turbulence properties including the pressure-related terms can be evaluated in various flows using data obtained by numerical simulations, e.g. a turbulent channel flow (Kim, 1989), a backward facing step flow (Le et al., 1997), the wake of a thick rectangular plate (Yao et al., 2001), a wall jet (Dejoan and Leschziner, 2006; Dejoan et al., 2006) and two opposing wall jets (Johansson and Andersson, 2005).

1.2.3 Turbulence modeling

For the prediction of engineering turbulent flows, the RANS methodology solving the time-averaged equations is now widely used although the unsteady flow simulation methods such as Large Eddy Simulation (LES) are becoming popular with the growth of computational power. When solving RANS equations, the Reynolds stress appears in the time-averaged momentum equation should be correctly treated. The representation of the Reynolds stress can be categorized into two main types, e.g. the Eddy Viscosity Model (EVM) and the Reynolds Stress Model (RSM). Differences among various turbulence models are noted in Pope (2000) and Durbin and Reif (2001). The EVM represents the Reynolds stress by the eddy viscosity and mean velocity gradient. Although a number of representations of the eddy viscosity have been proposed, the details of difference among various EVMs are not mentioned here. On the other hand, when using RSM, the Reynolds stress in the mean momentum equation is provided as the solution of the transport equation of the Reynolds stress. Some terms in the Reynolds stress transport equation should be modeled in order to close the systems of equations, and the reliability of the results strongly depends on the performance of the modeling of the pressure-related terms. Recent progress of the efforts on the turbulence modeling is available in the book of Launder and Sandham (2002), and details of some turbulence models are noted in Section 2.3.1.

1.2.4 Efforts to measure pressure fluctuations

The measurement of the fluctuating pressure away from the wall has been considered to be extremely difficult due to the intrusive nature of the pressure measurement using any types of pressure probes unlikely the fact that the measurement of the pressure fluctuation on the wall is a standard technique (Willmarth, 1975) and (Eckelmann, 1989). Recently, the array of wall pressure sensors have also been applied to obtain the field of wall pressure fluctuation (Lee and Sung, 2002), (Hudy et al., 2007) and (Aditjandra et al., 2009). For the fluctuating pressure measurement on the wall, the pressure sensor is usually equipped inside of the wall so that the distance between the pinhole on the wall surface and the diaphragm of the pressure sensor can be minimized in order to obtain better frequency response. However, in the case of the pressure measurement at arbitrary position in the flow, it is inevitable to use the tube-type probe to avoid the flow disturbance. Fuchs (1972) presented the possible sources of measurement error in the fluctuating pressure measurement using a Pitot-tube and George et al. (1984) briefly summarized:

1. *acoustic contamination due to spurious disturbances superimposed on the flow and originating exterior to it;*
2. *wind noise arising from the flow over the aerodynamic body containing the pressure-sensitive orifice;*
3. *acceleration response to flow-induced vibrations of the probe;*
4. *flow-affected sensitivity arising from, for example, directional effects;*
5. *resolution error due to averaging over the surface of the probe;*
6. *error due to fluctuating cross-flow;*
7. *response to axial-velocity fluctuations;*

Shirahama and Toyoda (1993) also showed the requirements for accurate fluctuating pressure measurement:

1. *small flow disturbance with inserting the probe;*
2. *small pressure sensing area;*
3. *small cross-flow error;*
4. *wide range of frequency response;*

Major contributions for the history of the fluctuating pressure measurement are illustrated in Fig. 1.1 and the specifications of pressure probes used in previous studies are summarized in Table 1.1

Attempts to measure pressure fluctuations were firstly made by Rouse (1953, 1954). They used a spherically tipped, upstream-oriented tube of 6.35 mm diameter. Kobashi (1957) and Kobashi et al. (1960) firstly performed a simultaneous measurement of fluctuating velocity and pressure using a 1.5 mm diameter static pressure probe with a condenser microphone and evaluated the contribution of the pressure diffusion term in the wake of a circular cylinder. Strasberg (1963) and Strasberg and Cooper (1965) reported the fluctuating pressure measured by a 2.4 mm diameter probe with ring slit 12.7 mm behind the nose. Sami et al. (1967) improved the probe of Rouse (1954) and used a 3.175 mm diameter piezo-electric ceramic tube. In addition, Sami (1967) made a slight modification to his static probe: the tip of the static pressure probe was removed for the measurement of the fluctuating total pressure and tried to evaluate the fluctuating pressure indirectly.

Siddon (1969) used a specially designed static pressure probe and investigated the effect of turbulence. Based on his success, Fuchs (1970, 1972) and Michalke and Fuchs (1975) used a shrouded condenser microphone; Arndt and Nilsen (1971), Arndt

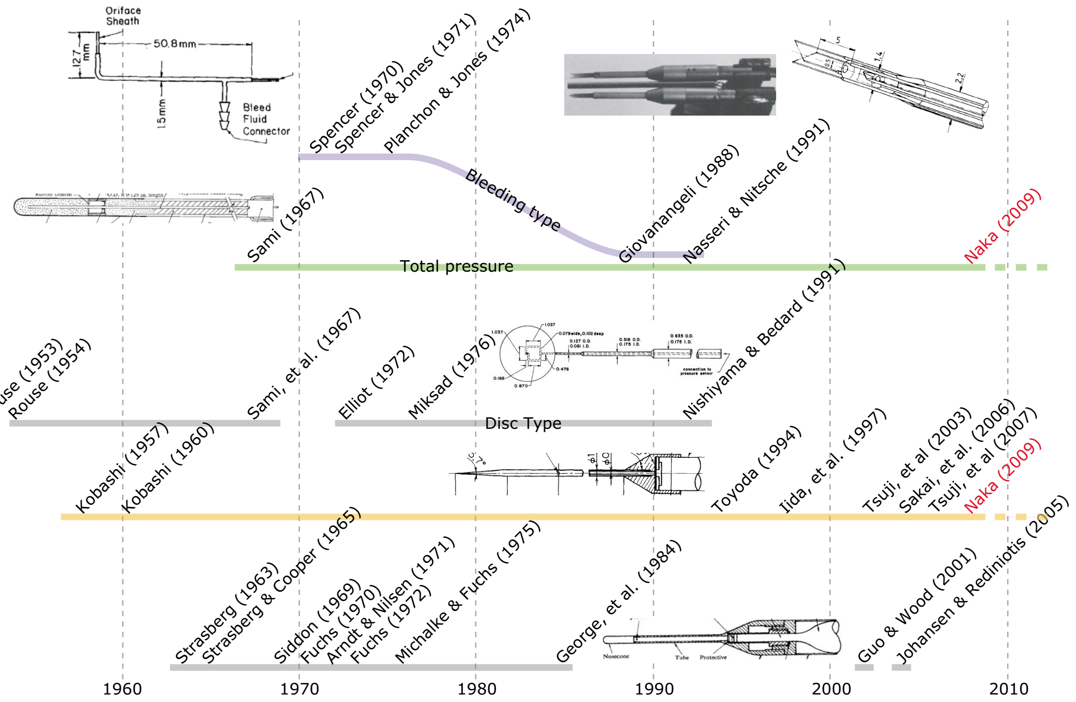

Figure 1.1: History of pressure measurement.

et al. (1974) and George et al. (1984) employed similar types of static pressure probes as Siddon (1969) used.

Spencer (1970), Spencer and Jones (1971) and Planchon and Jones (1974) developed a bleeding-type fluctuating static pressure probe, which actually measured the flow velocity in a thin pipe using a hot-film probe. The pressure was calculated from the volume flow rate being proportional to the velocity in the pipe. The advantage of this probe lay in the better spatial resolution but the sensitivity was rather limited. Using the bleeding-type fluctuating pressure probe, Giovanangeli (1988) and Nasseri and Nitsche (1991) developed probes for indirect measurement of the fluctuating pressure: the static pressure was calculated from the total and dynamic pressure.

The disc type fluctuating pressure probe, which had the 2D omni-directional sensitivity, was developed for the fluctuating pressure measurement in atmospheric flows, e.g. a single disc probe based on fluctuating lift principle by Elliot (1972), a dual-disc probe by Miksad (1976) and a “Quad-Disc” probe by Nishiyama and Bedard (1991) though these probes had a poor yaw-angle response against the disc plane.

Guo and Wood (2001) used a commercially available cobra probe and performed the simultaneous measurement of velocity and pressure, and reported that the velocity-pressure correlation was poorly measured. Johansen and Rediniotis (2005a,b,c) developed a multi-hole pressure probe fabricated by micro-electro mechanical systems (MEMS) technology and it was combined with conventional miniature pressure transducers. The dynamic calibration of the probe was performed.

Based on the work done by Kobashi (1957), Shirahama and Toyoda (1993) and Toyoda et al. (1994) developed a thin static pressure probe for the accurate measurement of pressure fluctuation, and the possibility of the simultaneous measurement of velocity and pressure was demonstrated. This technique was successfully extended to several applications. Iida et al. (1999) investigated the aerodynamic sound source in the wake of a circular cylinder. Tsuji and Ishihara (2003) measured pressure spectra and the probability density function (PDF) in a turbulent jet. Tsuji et al. (2007) also evaluated scaling parameters of the fluctuating pressure and the velocity-pressure correlation in a turbulent boundary layer. Sakai et al. (2007) applied this technique to a rectangular jet.

Tsuji and Ishihara (2003) and Tsuji et al. (2007) used a miniature piezo-resistive pressure transducer in addition to a condenser microphone. Generally, the microphone does not sense the pressure perturbation lower than 20 Hz but it can detect the small amplitude of pressure fluctuation. On the other hand, the transducer has the frequency response from DC but it cannot detect the small perturbation (typically less than 10 Pa).

The flat-frequency response, high sensitivity and high S/N ratio are crucial to capture the pressure fluctuation with broad dynamic and frequency range. Tsuji and Ishihara (2003) introduced a post-processing technique for compensating non-flat frequency response (amplitude and phase) of the pressure fluctuation inside the probe.

Several attempts have been reported calculating the pressure field by solving the Navier-Stokes equation or the Poisson equation for pressure using velocity field obtained by PIV. Obi and Tokai (2006) and Ishii et al. (2008) calculated the pressure field by solving the Poisson equation for pressure. Obi and Tokai (2006) applied this technique to the oscillatory flow between two bluff bodies in tandem, and Ishii et al. (2008) extended this technique to the wing-tip vortex. Liu and Katz (2006) calculated pressure field of the flow inside a cavity by solving the Navier-Stokes equation. Murai et al. (2007) tested these two methods, i.e., solving the Navier-Stokes equation and the Poisson equation for pressure, and pointed out advantages and disadvantages of these two methods: solving the Navier-Stokes equation requires the time derivative of the velocity field and the pressure field obtained by solving the Poisson equation is sensitive to the boundary condition. Because extraordinary efforts, e.g. Herpin et al. (2008), are necessary to have a sufficient spatial resolution to capture the smallest scale of the turbulent flow by PIV, it is difficult to distinguish the contribution of fine vortical structure to pressure fluctuations.

Pressure Sensitive Paint (PSP) has become popular as a relatively new technique for the surface imaging of the pressure distribution (Tropea et al., 2007). The PSP has advantage for obtaining the surface distribution of pressure. However, PSP is still under development to capture the small and fast perturbation of the pressure fluctuation. Presently, PSP tends to be applied high-speed flow (including compressible flows), and it has not been applied to the fluctuating pressure measurement in turbulent free shear flows yet.

1.3 Scope and organization of this thesis

The scope and contribution of the present thesis are:

- To establish the technique for the simultaneous measurement of fluctuating velocity and pressure which is applicable to complex turbulent flows
- To investigate the effect of the distinct structure of vortex on the statistical characteristics of the pressure fluctuation and the velocity-pressure correlation in the following test cases:
    - the developing region of a turbulent mixing layer;
    - the near field of a wing-tip vortex;

According to the literature reviews on the fluctuating pressure measurement, the only method successfully used now is the miniature static pressure probe developed by Toyoda et al. (1994). In the present thesis, a miniature static pressure probe according to Omori et al. (2003) following a work by Toyoda et al., and an X-wires hot-wire probe were applied to measure fluctuating velocity and pressure simultaneously. We also choose another method where total and dynamic pressure measurements are combined: the idea is similar to that in previous studies by Giovanangeli (1988) and Nasseri and Nitsche (1991). The novelty in the present study lies in a better sensitivity and spatial resolution accomplished by the use of the condenser microphone and an extremely thin pipe for the pressure probe: a miniature probe has been manufactured by means of precision machining, and combined with an X-wires hot-wire probe. In addition to using carefully designed pressure probes, the signal processing techniques for the phase correction and noise reduction of fluctuating pressure signals are introduced so that the difficulties in the fluctuating pressure measurement can be avoided. The assessment of techniques for the evaluation of the velocity-pressure correlation is addressed.

In Chapter 2, the theoretical basis of the present study is presented. In Chapter 3, the technique for the simultaneous measurement of fluctuating velocity and pressure is described in detail. In Chapter 4, results obtained in a turbulent mixing layer are presented. In Chapter 5, the techniques are applied to the measurement in the wing-tip vortex. In Chapter 6, the conclusion of this thesis is addressed.

Table 1.1: Specifications of pressure probes.

Author	Dimension [mm]	Transducer type	Frequency response [Hz]	Sensitivity [mV/Pa]
Rouse (1953, 1954)	6.4 (spherical)	piezometer		
Sami et al. (1967)	3.2	PZT-5 (Clevite corp.)	25–800	
Kobashi (1957)	1.5	condenser mic.	60–3 k	
Strasberg (1963)	4.8/2.4	condenser mic.	DC–800	0.51
George et al. (1984)	3.2	1/8 inch condenser mic. B&K 2801	20–1 k	
Spencer and Jones (1971)	0.89	bleeding type	DC–8 k	0.031
Elliot (1972)	0.51 (port dia.)	disc type probe	0.003–20	
Nasseri and Nitsche (1991)	1	bleeding type	20–1.5 k	
Shirahama and Toyoda (1993) and Toyoda et al. (1994)	1	1/4 inch condenser mic. Aco	5–2 k	4.02
Johansen and Rediniotis (2005c)	6.35, head dia.	Kulite XCS-062-5D	DC–20 k	
Tsuji et al. (2007)	0.5	condenser mic.	5–10 k	
	0.5	transducer	DC–10 k	
present	1	condenser mic.	20–1 k	4.5
	0.5 (TP-probe)	RION UC-29	20–600	

Chapter 2

Theoretical considerations

2.1 Governing equations

In the present thesis, since the low-speed air flows are handled, the property of fluid can be considered as the Newtonian, and the incompressible assumption is valid. The Cartesian coordinate system is considered.

The continuity equation of incompressible flow is written in the form:

$$\frac{\partial \hat{u}_i}{\partial x_i} = 0. \tag{2.1}$$

The Navier-Stokes equation for the Newtonian fluid under incompressible assumption is written as:

$$\rho \left(\frac{\partial \hat{u}_i}{\partial t} + \hat{u}_j \frac{\partial \hat{u}_i}{\partial x_j} \right) = -\frac{\partial \hat{p}}{\partial x_i} + \mu \frac{\partial \hat{u}_i}{\partial x_j x_j}. \tag{2.2}$$

The pressure field can be determined by the Poisson equation for pressure which can be obtained by taking divergence of Navier-Stokes equation Eq. (2.2) and the use of the continuity equation Eq. (2.1).

$$\frac{\partial^2 \hat{p}}{\partial x_i^2} = -\rho \frac{\partial^2 \hat{u}_i \hat{u}_j}{\partial x_i \partial x_j}. \tag{2.3}$$

The pressure can be obtained from the velocity field using either the Navier-Stokes equation Eq. (2.2) or the Poisson equation for pressure Eq. (2.3).

2.2 Time-averaged governing equations

To derive the equations for time-averaged quantities, instantaneous quantities are split into the time-averaged and fluctuating quantities, which is called Reynolds decomposition firstly proposed by Reynolds (1895):

$$\hat{h} = H + h, \tag{2.4}$$

where $\hat{h}$ is the instantaneous value of an arbitrary quantity, H stands for time-averaged value, and h means the fluctuating component.

After applying this procedure, the continuity equations for time-averaged and fluctuating velocity components are obtained as follows:

$$\frac{\partial U_i}{\partial x_i} = 0, \quad \frac{\partial u_i}{\partial x_i} = 0. \tag{2.5}$$

In the same manner, the Reynolds Averaged Navier-Stokes (RANS) equation can be obtained from N-S equation Eq. (2.2):

$$\rho\left(\frac{\partial U_i}{\partial t} + U_j\frac{\partial U_i}{\partial x_j}\right) = -\frac{\partial P}{\partial x_i} + \frac{\partial}{\partial x_j}\left(\mu\frac{\partial U_i}{\partial x_j} - \rho\overline{u_i u_j}\right). \tag{2.6}$$

The additional Reynolds stress term is found in the right hand side of the momentum equation Eq. (2.6). The Reynolds stress term represents the momentum transport by turbulence.

The transport equation of the Reynolds stress is obtained from the Navier-Stokes equation:

$$\begin{aligned}
&\underbrace{\rho\frac{\partial \overline{u_i u_j}}{\partial t}}_{\text{Unsteady}} + \underbrace{\rho U_k\frac{\partial \overline{u_i u_j}}{\partial x_k}}_{\text{Convection: } C_{ij}} = \\
&\underbrace{-\rho\frac{\partial}{\partial x_k}\overline{u_i u_j u_k}}_{\text{Turbulent Diffusion: } D^t_{ij}} \underbrace{-\frac{\partial}{\partial x_k}\left(\overline{p u_i}\delta_{jk} + \overline{p u_j}\delta_{ik}\right)+}_{\text{Pressure Diffusion: } D^p_{ij}} \underbrace{\mu\frac{\partial}{\partial x_k}\frac{\partial \overline{u_i u_j}}{\partial x_k}}_{\text{Viscous Diffusion: } D^v_{ij}} \\
&\underbrace{-\rho\left(\overline{u_j u_k}\frac{\partial U_i}{\partial x_k} + \overline{u_i u_k}\frac{\partial U_j}{\partial x_k}\right)}_{\text{Production: } P_{ij}} + \underbrace{\overline{p\left(\frac{\partial u_i}{\partial x_j} + \frac{\partial u_j}{\partial x_i}\right)}}_{\text{Re-distribution: } \phi_{ij}} \underbrace{-2\mu\overline{\frac{\partial u_i}{\partial x_k}\frac{\partial u_j}{\partial x_k}}}_{\text{Dissipation: } \varepsilon_{ij}}.
\end{aligned} \tag{2.7}$$

Terms in the Reynolds stress transport equation are classified according to their physical interpretation (see Section 2.3). Among these terms, the re-distribution and the pressure-diffusion terms which originally come from the velocity-pressure-gradient term contain the fluctuating pressure.

The transport equation of the turbulent kinetic energy, $k = \overline{{u_i}^2}/2$, can be obtained by taking the trace of the Eq. (2.7) and divided by 2.

$$\frac{\partial k}{\partial t} + \underbrace{U_j \frac{\partial k}{\partial x_j}}_{C_k} = \underbrace{-\frac{1}{\rho}\frac{\partial \overline{u_i p}}{\partial x_i}}_{D_k^p} \underbrace{-\frac{\partial u_j (u_i^2/2)}{\partial x_j}}_{D_k^t} + \underbrace{\nu \frac{\partial^2 k}{\partial {x_i}^2}}_{D_k^\nu} \underbrace{-\frac{\partial U_i}{\partial x_j}\overline{u_i u_j}}_{P_k} \underbrace{-\nu \overline{\left(\frac{\partial u_i}{\partial x_j}\right)^2}}_{\varepsilon_k}. \tag{2.8}$$

The re-distribution term in Eq. (2.7) mathematically turns to be zero.

The Poisson equation of fluctuating pressure p can be derived from Eq. (2.3) with applying Reynolds decomposition and subtracting time averaged one:

$$\frac{1}{\rho}\frac{\partial^2 p}{\partial {x_i}^2} = -2\frac{\partial u_j}{\partial x_i}\frac{\partial U_i}{\partial x_j} - \frac{\partial u_i}{\partial x_j}\frac{\partial u_j}{\partial x_i} + \frac{\partial^2 \overline{u_i u_j}}{\partial x_i \partial x_j}. \tag{2.9}$$

The fluctuating pressure can be decomposed into two main contributions, rapid and slow terms. The rapid pressure $p^{(r)}$ satisfies:

$$\frac{1}{\rho}\frac{\partial^2 p^{(r)}}{\partial {x_i}^2} = -2\frac{\partial U_i}{\partial x_j}\frac{\partial u_j}{\partial x_i}. \tag{2.10}$$

The slow pressure $p^{(r)}$ satisfies:

$$\frac{1}{\rho}\frac{\partial^2 p^{(s)}}{\partial {x_i}^2} = -\frac{\partial u_i}{\partial x_j}\frac{\partial u_j}{\partial x_i} + \frac{\partial^2 \overline{u_i u_j}}{\partial x_i \partial x_j}. \tag{2.11}$$

The rapid term immediately reflects the change of the mean velocity gradient and the slow term indicates the interaction of turbulence. The fundamental solution of Eq. (2.9) for an infinite domain without boundaries becomes:

$$p(\mathbf{x},t) = \frac{\rho}{4\pi}\int_{\mathcal{R}^3} \left(-2\frac{\partial u_j}{\partial x_i}\frac{\partial U_i}{\partial x_j} - \frac{\partial u_i}{\partial x_j}\frac{\partial u_j}{\partial x_i} + \frac{\partial^2 \overline{u_i u_j}}{\partial x_i \partial x_j}\right) \frac{1}{|\mathbf{x}-\mathbf{x}'|} d\mathcal{V}. \tag{2.12}$$

This expression is a basis on developing the turbulence model of the re-distribution and the pressure-diffusion terms.

2.3 Explanation of the Reynolds stress transport equation

The physical interpretation of each term in the transport equation of the Reynolds stress Eq. (2.7) is noted below. The balance of these terms inside the infinitesimal control volume is depicted in Fig. 2.1 (Bradshaw, 1978).

- Convection: C_{ij}
  This term indicates the convection transport of the Reynolds stress on a infinitesimal control volume. It can also be regarded as the residual of the balance among other terms in the transport equation.

- Production: P_{ij}
  This term shows the production of the Reynolds stress due to the mean velocity gradient. In RSM, since this term only consists of known quantities, i.e., the Reynolds stress and the mean velocity gradient, this term does not need to be modeled.

- Turbulent-diffusion: D^t_{ij}
  This term represents the diffusion of the Reynolds stress due to the fluctuating velocity in the control volume. This term is modeled based on the idea of “gradient diffusion” (Shir, 1973) or the transport equation of triple velocity moment (Hanjalić and Launder, 1972).

- Pressure-diffusion: D^p_{ij}
  This term is originated from the velocity-pressure-gradient term and representing the diffusion of the Reynolds stress caused by the fluctuating pressure. As noted in Section 1.2.3, this term is considered to be small in the conventional RSM and it is implicitly modeled as the part of the turbulent diffusion effect. Since the effect of the fluctuating pressure is non-local, i.e., different from the effect of the fluctuating velocity, it is not appropriate to model this term by the gradient-diffusion hypothesis.

- Viscous-diffusion: D^v_{ij}
  This term indicates the diffusion of the Reynolds stress due to the viscosity. As

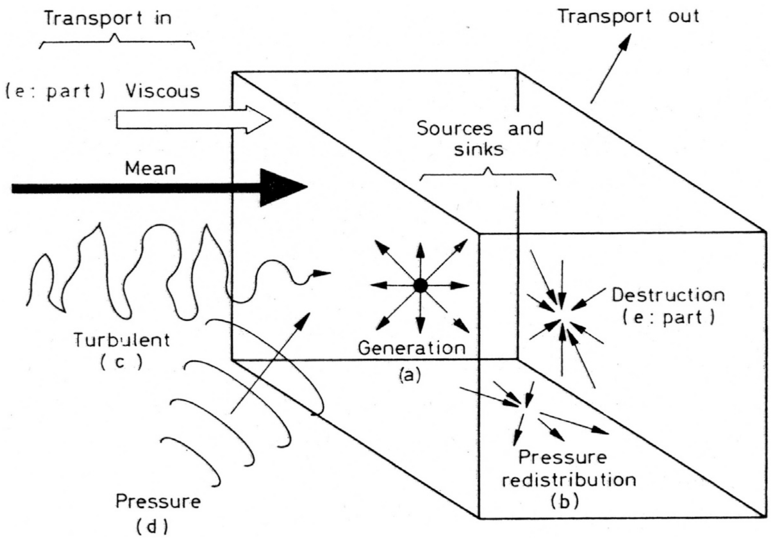

Figure 2.1: The balance of the Reynolds stress transport equation inside infinitesimal control volume (Bradshaw, 1978).

for the high Reynolds number free shear flows, this term can usually be negligible.

- Re-distribution: ϕ_{ij}
  This term is also derived from the velocity-pressure-gradient term. Since for the incompressible flow, $\phi_{ii} = 0$, this term represents the energy transfer among the different components. This effect always acts as the Reynolds stress tensor to be isotropic, i.e., for the normal components, this term affects the difference among the components small, and the shear component always decreases the Reynolds stress. This term is modeled based on the idea called "return to isotropy" (Rotta, 1951) traditionally, and many sophisticated models are now available (cf. Section 2.3.1).

- Dissipation: ε
  This term indicates the dissipation of the Reynolds stress to the heat. The normal components of this term become always positive and it always plays the negative contribution to the energy balance. The starting point to model this term is the transport equation of the dissipation rate ε. The model of the dissipation tensor

ε_{ij} is also available to take into account of the anisotropic nature of this term especially near the wall.

2.3.1 Modeling of the pressure-related terms

As noted in Section 1.2.3, the performance of modeling the pressure-related terms seriously affects the results. For the re-distribution term which plays a role to equalize the energy among the different components, numerous efforts have been devoted. Launder et al. (1975) proposed a model which is linear to the Reynolds stress. This model is currently widely used since this is validated in the simple shear flows and easy to implement. Speziale et al. (1991) introduced the non-linear terms and reported the improvement of the applicability to the complex flows, e.g. swirling flows and impinging flows. Durbin (1993) proposed the 'elliptic relaxation' method to cope with the difficulty near the wall. This method solves the elliptic equation about the re-distribution term including the representing length scale.

On the contrary to the active contributions on the modeling of the re-distribution term, another pressure-related term, the pressure-diffusion term, is less emphasized in the currently available turbulence models. The conventional RSM treats this term together with the turbulent-diffusion term. An explicit model for the pressure-diffusion term has been proposed by Lumley (1978):

$$\frac{\overline{u_i p}}{\rho} = -\frac{1}{5}\overline{u_i u_k^2}. \tag{2.13}$$

This model is derived from the realizability constraints on the solutions of the Poisson equation of the fluctuating pressure Eq. (2.9). This model assumes homogeneous turbulence and represents only slow part of pressure fluctuation. The representation of this model indicates that the effect of the pressure-diffusion is analogous to the turbulent-diffusion. Attempts to improve the near wall behavior of the pressure-diffusion terms were proposed by (Nagano and Tagawa, 1990) and (Sauret and Vallet, 2007).

Although it is true that this term is considerably small in simple shear flows except near the wall, the term can be comparable or even larger than other terms in some complex flows. Yao et al. (2001) reported that the pressure-diffusion term of the turbulent kinetic energy in the near-wake of the thick rectangular plate becomes equally important to other terms. Yoshizawa (2002) pointed out the importance of the effect of

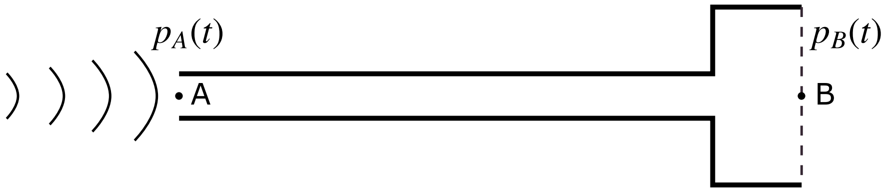

Figure 2.2: A model of the pressure probe.

the mean velocity gradient on the pressure-diffusion term. Suga (2004) proposed the model which takes into account the effect of the rapid part of the pressure fluctuation and reported the improvement of the results.

It is often claimed that the RANS model often gives substantially different results from experiment for complex flows. Currently available RSM still has the room for improving its applicability in the pressure-diffusion term which includes the velocity-pressure correlation.

2.4 Response of the air inside of the pressure probe

The response of the air inside of the model of pressure probe shown in Fig. 2.2 is analytically described. The cylindrical coordinates x, r and θ are used in this section, and the flow is assumed to be axi-symmetric. The pressure fluctuation at the end of the probe (position A) is transmitted to the diaphragm of the pressure transducer (position B). When considering the propagation of pressure fluctuation through a thin pipe, the flow should be treated as compressible. Therefore, the equation of continuity and Navier-Stokes equation for compressible flow are considered. In addition, the equation of state and the energy equation are also considered as follows;

The Navier-Stokes equation:

$$\begin{aligned}\tilde{\rho}\frac{\partial \tilde{u}}{\partial t}+\tilde{u}\frac{\partial \tilde{u}}{\partial x}+\tilde{v}\frac{\partial \tilde{u}}{\partial r} = -\frac{\partial \tilde{p}}{\partial x}+\mu\left\{\left[\frac{\partial^2 \tilde{u}}{\partial x^2}+\frac{\partial^2 \tilde{u}}{\partial r^2}+\frac{1}{r}\frac{\partial \tilde{u}}{\partial r}\right]\right. \\ \left.+\frac{1}{3}\frac{\partial}{\partial x}\left[\frac{\partial \tilde{u}}{\partial x}+\frac{\partial \tilde{v}}{\partial r}+\frac{\tilde{v}}{r}\right]\right\},\end{aligned} \tag{2.14}$$

$$\tilde{\rho}\frac{\partial \tilde{v}}{\partial t} + \tilde{u}\frac{\partial \tilde{v}}{\partial x} + \tilde{v}\frac{\partial \tilde{v}}{\partial r} = -\frac{\partial \tilde{p}}{\partial r} + \mu\left\{\left[\frac{\partial^2 \tilde{v}}{\partial r^2} + \frac{1}{r}\frac{\partial \tilde{v}}{\partial r} - \frac{\tilde{v}}{r^2} + \frac{\partial^2 \tilde{v}}{\partial x^2}\right]\right.$$
$$\left. + \frac{1}{3}\frac{\partial}{\partial r}\left[\frac{\partial \tilde{u}}{\partial x} + \frac{\partial \tilde{v}}{\partial r} + \frac{\tilde{v}}{r}\right]\right\}; \qquad (2.15)$$

The continuity equation:

$$\frac{\partial \tilde{\rho}}{\partial t} + \tilde{u}\frac{\partial \tilde{\rho}}{\partial x} + \tilde{v}\frac{\partial \tilde{\rho}}{\partial r} + \tilde{\rho}\left[\frac{\partial \tilde{u}}{\partial x} + \frac{\partial \tilde{v}}{\partial r} + \frac{\tilde{v}}{r}\right] = 0; \qquad (2.16)$$

The equation of state for an ideal gas:

$$\tilde{p} = \tilde{\rho} R_0 \tilde{T}; \qquad (2.17)$$

The energy equation:

$$\tilde{\rho} g c_p \left[\frac{\partial \tilde{T}}{\partial t} + \tilde{u}\frac{\partial \tilde{T}}{\partial x} + v\frac{\partial \tilde{T}}{\partial r}\right] =$$
$$\lambda\left[\frac{\partial^2 \tilde{T}}{\partial r^2} + \frac{1}{r}\frac{\partial \tilde{T}}{\partial r} + \frac{\partial^2 \tilde{T}}{\partial x^2}\right] + \frac{\partial \tilde{p}}{\partial t} + u\frac{\partial \tilde{p}}{\partial x} + v\frac{\partial \tilde{p}}{\partial r} + \mu\Phi, \qquad (2.18)$$

where Φ is the dissipation function that represents the heat transfer caused by internal friction:

$$\Phi = 2\left[\left(\frac{\partial \tilde{u}}{\partial x}\right)^2 + \left(\frac{\partial \tilde{v}}{\partial r}\right)^2 + \left(\frac{\tilde{v}}{r}\right)^2\right] + \left[\frac{\partial \tilde{v}}{\partial x} + \frac{\partial \tilde{u}}{\partial r}\right]^2 - \frac{2}{3}\left[\frac{\partial \tilde{u}}{\partial x} + \frac{\partial \tilde{v}}{\partial r} + \frac{\tilde{v}}{r}\right]^2. \qquad (2.19)$$

Here we can put the quantities as the wave form, and following assumptions are made:

- the sinusoidal disturbances are very small;
- the internal radius of the tube is small in comparison with its length;
- the flow is laminar throughout the system;

$$\left.\begin{aligned}
\tilde{p} &= p_s + p\exp(i\omega t)\\
\tilde{\rho} &= \rho_s + \rho\exp(i\omega t)\\
\tilde{T} &= T_s + T\exp(i\omega t)\\
\tilde{u} &= u\exp(i\omega t)\\
\tilde{v} &= v\exp(i\omega t)
\end{aligned}\right\} \qquad (2.20)$$

where ω is angular frequency; γ is specific heat ratio; a_0 is speed of sound; c_p is specific heat at constant pressure; λ is thermal conductivity.

Substituting Eq. (2.20), Eqs. (2.14)–(2.18) can be simplified to:

$$i\omega u = -\frac{1}{\rho_s}\frac{\partial p}{\partial x} + \frac{\mu}{\rho_s}\left[\frac{\partial^2 u}{\partial r^2} + \frac{1}{r}\frac{\partial u}{\partial r}\right], \tag{2.21}$$

$$0 = -\frac{\partial p}{\partial r}, \tag{2.22}$$

$$i\omega \rho = -\rho_s\left[\frac{\partial u}{\partial x} + \frac{\partial v}{\partial r} + \frac{v}{r}\right], \tag{2.23}$$

$$\rho = \frac{\gamma}{a_o^2}\left(1 + \frac{\rho_s}{T_s}\frac{T}{\rho}\right), \tag{2.24}$$

$$i\omega \rho_s g c_p T = \lambda\left[\frac{\partial^2 T}{\partial r^2} + \frac{1}{r}\frac{\partial T}{\partial r}\right] + i\omega p. \tag{2.25}$$

The detailed procedure for solving Eqs. (2.21)–(2.25) is described in Bergh and Tijdeman (1965). Following boundary conditions are imposed on the unknown quantities p, ρ, T, u and v:

At the wall of the tube $(r = R)$:

- zero radial and axial velocity, i.e.: $u = 0$; $v = 0$
- the conductivity of the wall is supposed to be so large that the variation in temperature at the wall will be zero: $T = 0$

At the center of the tube $(r = 0)$:

- due to the axial-symmetry of the problem: $v = 0$
- a further requirement is that the values of u, T, p and ρ remain finite

In addition, following assumptions are made:

- the pressure and the density in the instrument volumes are only time dependent
- the pressure expansion in the instrument volume is a polytropic process, described by $\frac{p_v}{\rho_v}k_p = \text{const}$.

The complex response of the pressure fluctuation against the sinusoidal perturbation p_A at the end of the pressure tube is considered. When considering the simple model of pressure measurement system shown in Fig. 2.2, the pressure fluctuation at the diaphragm p_B is calculated following equations derived from the solution of Eqs. (2.21)–(2.25).

$$\frac{p_A}{p_B} = \left[\cosh(\phi L) + \frac{V_v}{V_t}(\sigma + \frac{1}{k_p})n\phi L \sinh(\phi L)\right]^{-1}. \tag{2.26}$$

$$\phi = \frac{\omega}{a_0}\sqrt{\frac{J_0(\beta)}{J_2(\beta)}}\sqrt{\frac{\gamma}{n}}, \quad \beta = i\sqrt{i}R\sqrt{\frac{\rho_s\omega}{\mu}},$$
$$n = \left[1 + \frac{\gamma-1}{\gamma}\frac{J_2(\beta\sqrt{Pr})}{J_0(\beta\sqrt{Pr})}\right]^{-1}, \quad Pr = \frac{\mu g c_p}{\lambda}, \tag{2.27}$$

where L is the length of the pipe; V_v is volume of cavity; V_t is volume of tube; σ is dimensionless increase of cavity volume; k_p is polytropic constant; J_n is Bessel function.

Chapter 3

Measurement technique

3.1 Fluctuating pressure probes

A thin static pressure probe (SP-probe) as sketched in Fig. 3.1 was used for the fluctuating static pressure measurements. The probe was set parallel to the flow direction so that the static pressure fluctuation can be sensed at the four 0.4 mm holes on the side of the 1.0 mm thick pipe. The inner diameter of the SP-probe is 0.75 mm: the thickness of the tube wall is 0.125 mm. The wall thickness affects the yaw-angle performance: the thinner pipe wall brings better performance. According to the systematic tests checking the effects of the distance from tip to the pressure holes, the size of the pressure holes and the number of holes (Toyoda, 2007), Toyoda et al. (1994) decided the geometry of the static pressure probe. The static pressure probe employed in the present study adopted the same design except the thickness of the wall of the tube; Toyoda et al. (1994) used the probe with the wall thickness 0.1 mm.

The TP-probe illustrated in Fig. 3.2 was used to measure the fluctuating total pressure. An extremely thin pipe with inner- and outer-diameters of 0.4 mm and 0.5 mm, respectively, was attached to the condenser microphone. The tip of the TP-probe was rounded in order to minimize the flow disturbance as well as to obtain a good yaw-angle performance.

The pressure fluctuation was converted to an electric signal by a condenser microphone (RION UC-29) which was mounted on the end of the pressure probe. The condenser microphone was connected to a conversion adapter (RION UA-12), a pre-amplifier (RION NH-05) and a main-amplifier (RION UN-04). The combination of the

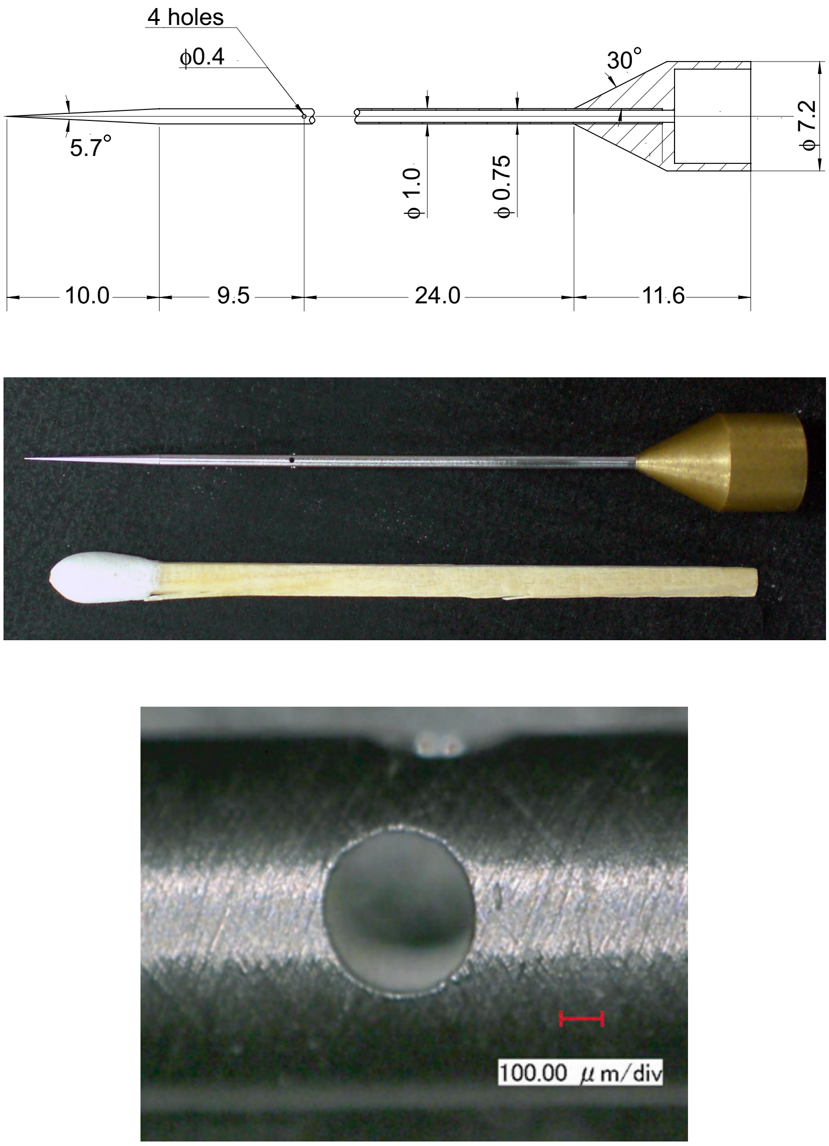

Figure 3.1: Schematic of the static pressure probe (dimensions in mm).

condenser microphone and pre-amplifier has the flat frequency response from 20 Hz to 100 kHz. The self noise level is 42 dB SPL (2.5×10^{-4} Pa) and the sensitivity level is -47 dB rel. 1 V/Pa (4.5 mV/Pa). The range of the main amplifier was set to 120 dB SPL rms which corresponds to 20 Pa rms throughout the experiments. The full scale output of the amplifier is 1 V rms and dynamic range is 85 dB; therefore, the smallest pressure perturbation of this amplifier is 0.055 mV rms which corresponds to

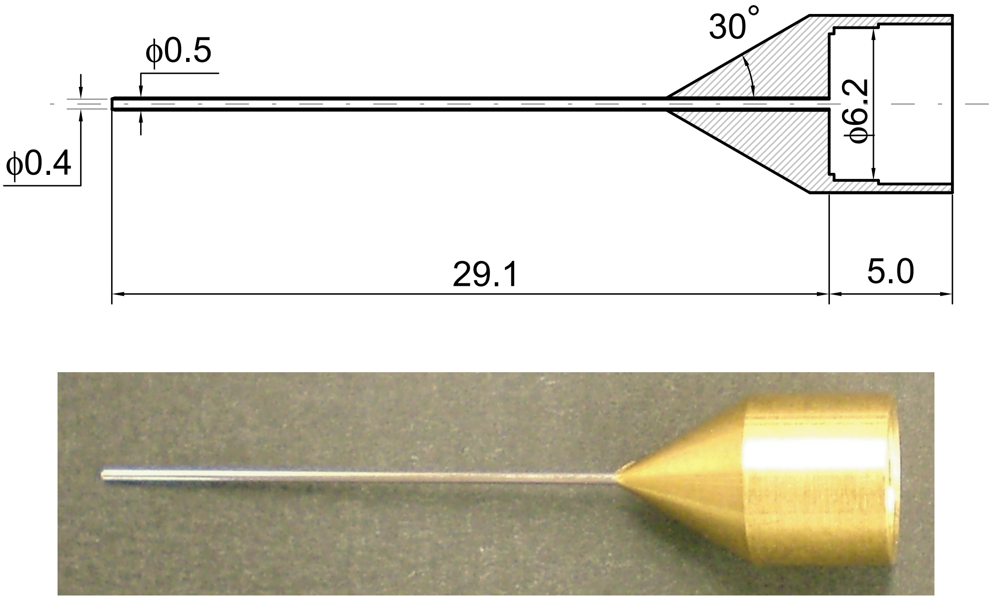

Figure 3.2: Schematic of the fluctuating total pressure probe (dimensions in mm).

1.1×10^{-3} Pa rms.

3.1.1 Calibration of yaw-angle effect

The flow direction varies in the turbulent flow; hence, the sensitivity of the TP-probe to the direction of the oncoming flow was investigated prior to the actual measurement. The TP-probe was placed in a uniform flow, and the direction of the probe axis was varied relative to the flow direction. The pressure variation was measured by a low range pressure transducer (Validyne DP45-18) that was connected to the probe in place of the condenser microphone.

The pressure coefficient C_p was calculated for various angles of attack α:

$$C_p(\alpha) = \frac{P_t(\alpha) - P_{t0}}{P_{t0}}, \tag{3.1}$$

with P_t being the mean total pressure measured as a function of the yaw-angles. P_{t0} is P_t at $\alpha = 0$. The value of C_p decreased with the increasing α as illustrated in Fig. 3.3. The C_p obtained by the TP-probe varies within 2% for $-20° \leq \alpha \leq 20°$, and the performance is better than the SP-probe which shows 7.5% variation in ±20°.

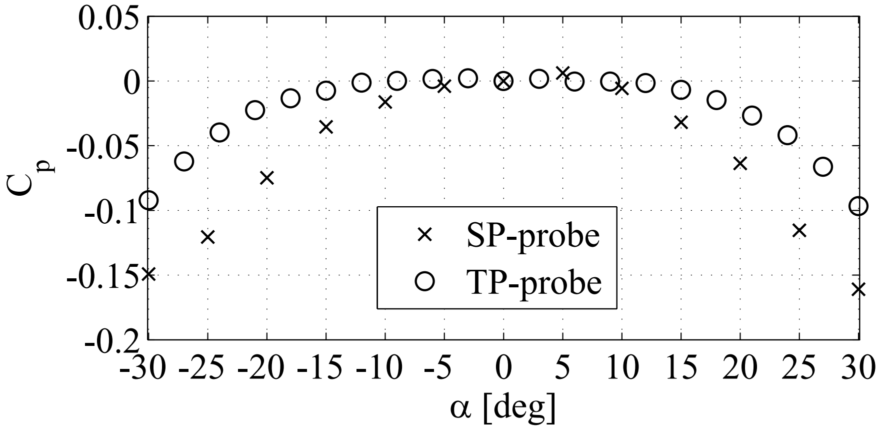

Figure 3.3: Effect of the flow angle of attack.

In the turbulent mixing layer case, the instantaneous flow angle calculated from the velocity data $\tan^{-1}(\hat{v}/\hat{u})$ is less than 20°. It is thus expected that the measurements of total pressure are not much affected by the fluctuation of the flow direction in that case. The effect in the case of the measurement in the wing-tip vortex is discussed in Chapter 5.

3.1.2 Frequency response

3.1.2.1 Effect of air inside pressure probes

The pressure probe has a non-flat frequency response due to the resonance of air inside of the probe and the effect of viscosity. For the measurement of the velocity-pressure correlation, the phase-lag between the velocity and pressure contaminates the result.

The frequency responses of the TP- and SP-probes were explored. The sound signal generated by a loudspeaker (YAMAHA HS80M) was measured by condenser microphones with and without the pressure probe simultaneously. The measurements were undertaken in a quasi-anechoic box shown in Fig. 3.4, and the frequency of the signal was varied from 100 Hz to 20 kHz. The reference data taken without the pressure probe exhibit the flat frequency response of the condenser microphone. The phase also remains unchanged for the entire frequency range as shown in Fig. 3.5. In contrast, mounting the TP-probe on the condenser microphone caused a gradual decrease in

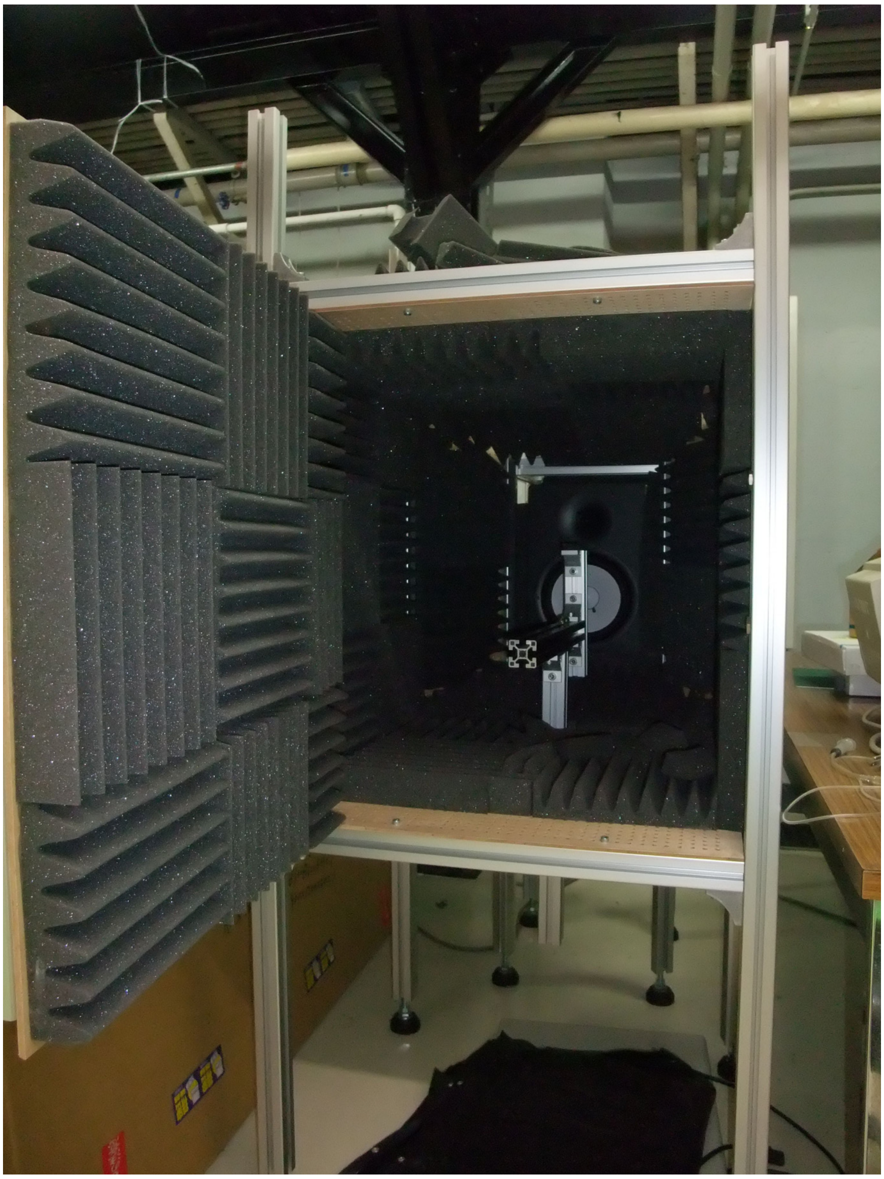

Figure 3.4: Photo of quasi-anechoic box.

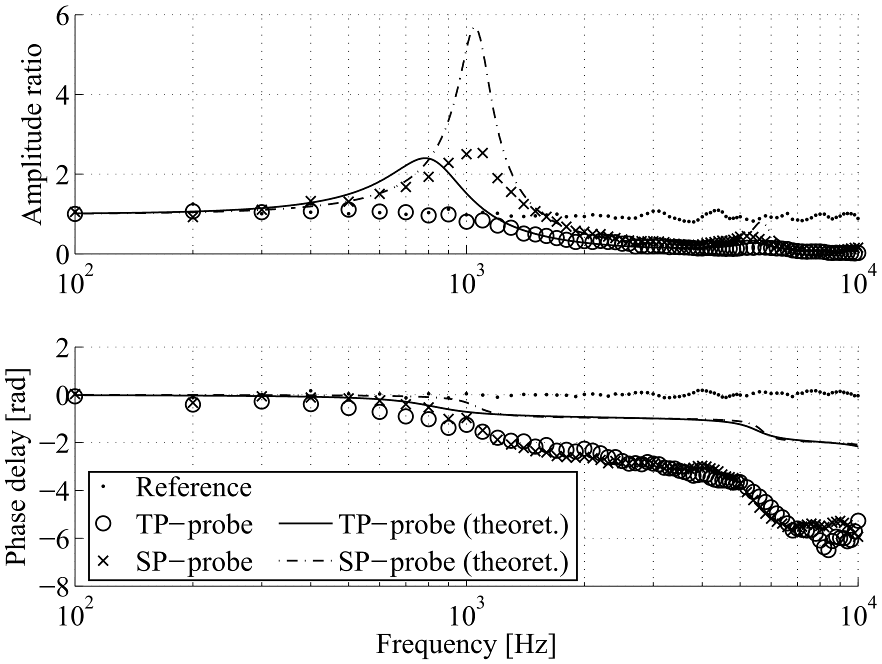

Figure 3.5: Frequency response of the SP- and TP-probes; Amplitude ratio (top), phase-lag (bottom).

amplitude for frequency higher than 1 kHz. There is an obvious phase difference for the entire frequency range examined here.

The theoretical prediction of the pressure fluctuation response based on Eq. (2.26) is presented in Fig. 3.5. Th resonance frequency shows good agreement with the experiment, but theoretical results show considerably high amplitude ratio at the resonance frequency. The difference may be related to the fact that the acoustic impedance at the inlet of the tube is not considered in the theoretical analysis.

In order to correct the above-mentioned phase delay, the measured phase delay was corrected by fitting to the cubic polynomial approximation. On the other hand, no correction is applied to the amplitude because no significant attenuation is found for the frequency range that corresponds to the experiment in the turbulent flow which is below 1 kHz in the present study.

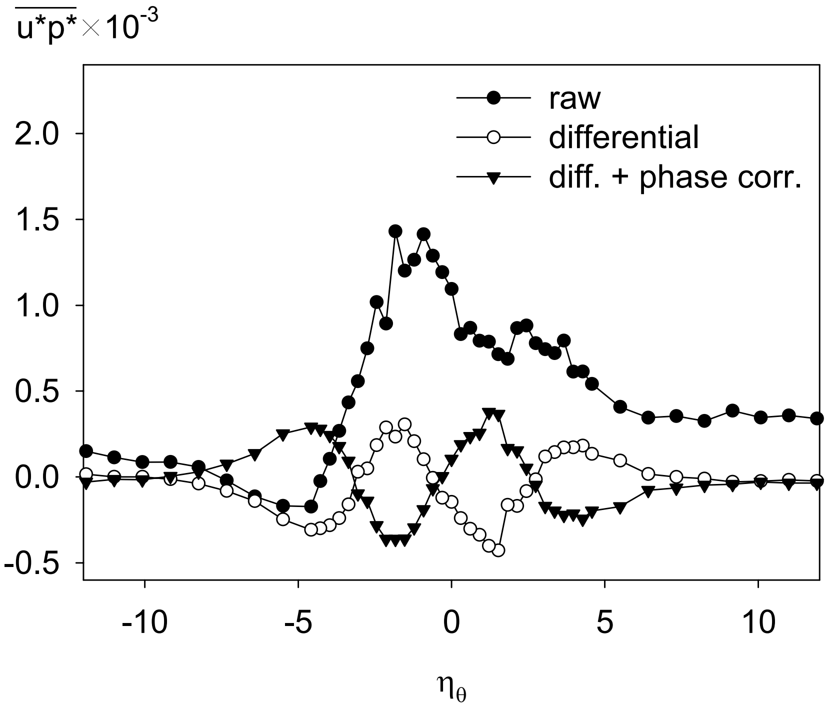

Figure 3.6: Corrected velocity-pressure correlations ($x = 100$ mm).

3.1.2.2 Condenser microphone

Another factor, which produces the phase delay of the pressure fluctuation lies in the electric circuit of the condenser microphone. The phase-lag that depends on the frequency is caused by the electric circuit of the condenser microphone system. In the present study, an analytical formula which was provided by the manufacturer was used to correct this phase-lag:

$$\theta_d = \pi - \tan^{-1}\left(\frac{1}{2\pi CRf}\right), \tag{3.2}$$

where C is electronic capacitance of the condenser microphone, R stands for the input resistance of main amplifier of the microphone, and f denotes the frequency of the fluctuating pressure. In the present study, C and R are 6 pF and 3 GΩ, respectively, according to the hardware specifications.

The effect of the correction is demonstrated in Fig. 3.6; the compensated velocity-pressure correlation shows a profile which takes a sign opposite to that of the value

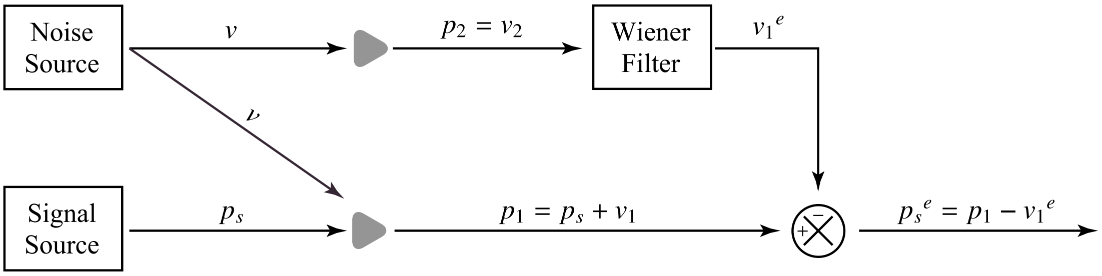

Figure 3.7: Diagram of noise reduction procedure using Wiener-filter.

without correction. It is rather surprising that the effect of the correction is not a slight fraction but remarkable in a qualitative manner.

3.2 Signal processing of fluctuating pressure

3.2.1 Noise reduction

In order to reduce the influence of background noise in the wind tunnel, the pressure signal outside the shear layer was monitored simultaneously by an auxiliary pressure probe which was identical as that used for the measurements in the shear layer. Firstly, the signal acquired by the auxiliary probe was simply subtracted from that obtained in the shear layer so that only the desired local pressure related to turbulent fluid motion could be extracted. The effect of such a practice is demonstrated in Fig. 3.6. The plots after the procedure (marked as ”differential”) show a remarkable reduction of background noise in the velocity-pressure correlation $\overline{up}$ in the free stream as compared to the raw data.

In addition to the simple subtraction scheme, the background noise due to the acoustic and vibration in the test section were reduced using the optimal filtering scheme similar to the one proposed by Naguib et al. (1996). The advantage of using this optimal filtering scheme is that the difference between noise signals measured by main and auxiliary probes can be considered. In Fig. 3.7, the whole procedure for the noise reduction is depicted. The pressure signal p_s is contaminated by the noise v_1. Signals obtained by the primary probe p_1 is the sum of the signal p_s and the noise v_1. On the other hand, the secondary probe only measures the noise component v_2 which is not exactly the same as v_1. Using the Wiener-filter, the noise v_1 buried in the signal

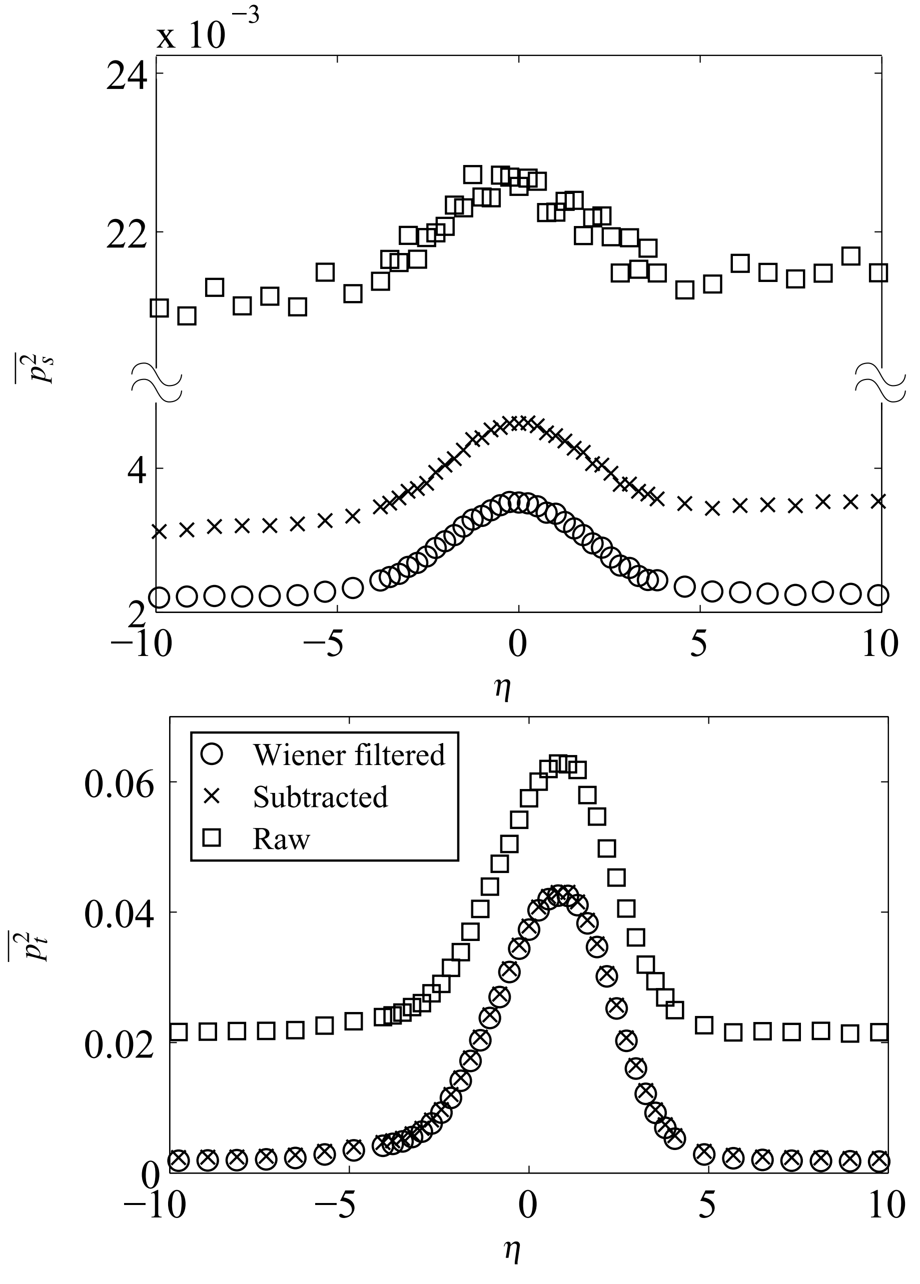

Figure 3.8: Effect of noise reduction practice; static pressure (top), total pressure (bottom).

p_1 is estimated from the noise v_2. When using this filter, it is assumed that the correlation between signal p_s and noise v_1, v_2 is zero. The signal from an auxiliary probe was used for determining the filter coefficients. The filter coefficients are determined by solving the linear equation called "Wiener-Hopf equation".

$$\mathbf{R_x}\mathbf{w} = \mathbf{r_{dx}}, \tag{3.3}$$

where $\mathbf{R_x}$ and $\mathbf{r_{dx}}$ are the auto-correlation matrix and the cross-correlation vector. $\mathbf{w}$ is a set of filter coefficients. $\mathbf{w}$ is obtained by solving Eq. (3.3). Intuitively, when the cross correlation vector $\mathbf{r_{dx}} = 0$, the filter becomes *no-pass filter*; when the cross correlation vector is identical to the auto correlation vector, it acts as *all pass filter*. In real application, the situation becomes somewhere in the middle of above mentioned two extreme conditions. Detailed description about the noise canceling technique using Wiener-filter is available in Hayes (1996).

The effect of the noise correction practices are demonstrated in Fig. 3.8. As for the performance of Wiener-filter (noted as "Wiener-filtered"), 58.1% of static pressure fluctuation and 5.6% of total pressure fluctuation, both in magnitude, were reduced at $y = 0$ mm, $x = 100$ mm in the mixing layer case. Since Wiener-filtering gives less pressure fluctuation in the free stream region, the noise reduction procedure using Wiener-filter achieves better performance than the simple subtraction.

3.3 Velocity measurements

The fluctuating velocity was measured by a hot-wire anemometer. Several different types of hot-wire probes, e.g. self-fabricated I-type Hot-wire; Kanomax, 0251R-T5 (I-type); Dantec, 55P64 (X-type); Dantec, 55P54(X-type); Dantec, 55R91(triple hot-film probe), were used for different purposes. Each hot-wire probe was connected to a Constant Temperature Anemometer (CTA, Kanomax 1010, 1011). A temperature measurement unit (Kanomax 1020) was used if the effect of the temperature variation during the experiment was needed to be corrected.

3.3.1 Calibration of hot-wire probes

Calibration of each hot-wire probe was performed before and after every run of the measurement. As for the I-type probe, fourth order polynomial curve fit was used

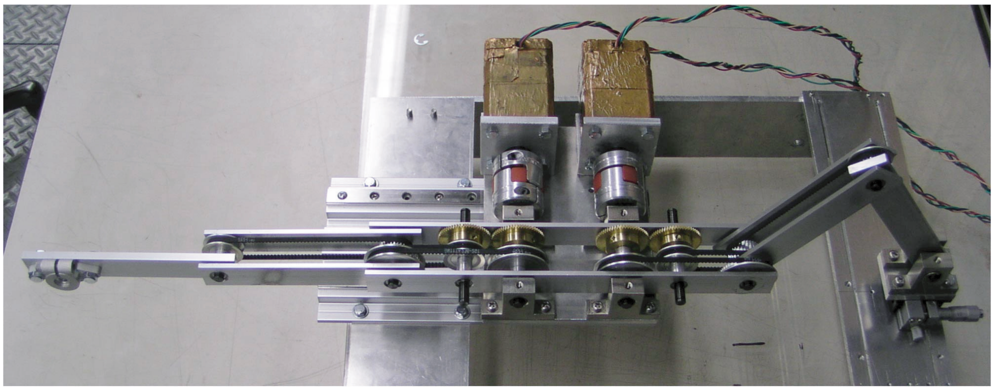

Figure 3.9: Traversing mechanism for look-up table calibration.

(Bruun, 1995). In order to obtain two velocity components from the signal of the X-probe, we used the look-up table method by Lueptow et al. (1988) and the effective angle calibration method by Browne et al. (1989). In the case of the mixing layer experiment, the look-up table calibration was performed using traversing gear shown in Fig. 3.9. In the wing-tip vortex, the effective-angle calibration method was extended so that the effect of the velocity component out of the X-probe plane could be taken into account. The apparent increase of the velocity due to the contribution of the out of X-probe plane component was reduced using the result of the pitch-angle calibration. Signals from the triple-probe were converted into three velocity components using equations in Jørgensen (2002).

3.4 Basic theory for fluctuating static pressure calculation

The fluctuating static pressure is calculated by subtracting the dynamic pressure from the total pressure. We assume viscous effects to be negligible in determining the pressure, and apply the Euler equation to the instantaneous flow pattern around the end of a tube as shown in Fig. 3.10. The points A and B in the figure are considered to represent the location where measurements are undertaken for velocity and total pressure, respectively. The point A$'$ is defined along the streamline that impinges onto point B

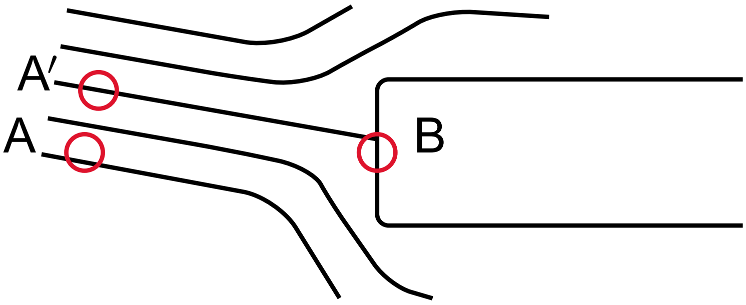

Figure 3.10: Streamlines near the total pressure probe.

at an arbitrary instant. Integrating the Euler equation from point A′ to B, we obtain:

$$\int_{A'}^{B}\left(v_s\frac{\partial v_s}{\partial s}+\frac{1}{\rho}\frac{\partial p}{\partial s}\right)ds=-\int_{A'}^{B}\frac{\partial v_s}{\partial t}ds, \tag{3.4}$$

where v_s is the instantaneous velocity in the s-direction, with s being the coordinate defined along the streamline. ρ and p represent fluid density and pressure, respectively.

A convenient form to express the relationship between velocity, total and static pressures can be obtained:

$$\hat{p}=\hat{p}_t-\frac{\rho}{2}\hat{u}^2+\frac{\rho}{2}\frac{\partial \hat{u}}{\partial t}\Delta x, \tag{3.5}$$

where p, p_t and u are the static pressure, the total pressure and the streamwise velocity component, and $\hat{}$ indicates the instantaneous variables. Δx stands for the distance between the points A and B. Equation (3.5) is valid when [1] the time-derivative of fluctuating velocity linearly approaches to zero at the end of the TP-probe; [2] the two streamlines passing through points A and A′ are nearly parallel to each other; [3] the instantaneous velocity and pressure are nearly the same at points A and A′; and [4] the angle of attack of the stagnating streamline is not too large.

The relationship among the fluctuating components of these variables can be derived by applying the Reynolds decomposition to Eq. (3.5):

$$p=p_t-\frac{\rho}{2}\left(2Uu+u^2-\overline{u^2}\right)+\frac{\rho}{2}\frac{\partial u}{\partial t}\Delta x, \tag{3.6}$$

where the upper- and lower-cases indicate the mean and fluctuating quantities, respectively, and $\bar{}$ denotes time-averaging. We use Eq. (3.6) to calculate the static pressure fluctuation from the total pressure measured by the TP-probe and the dynamic pressure measured by the X-probe.

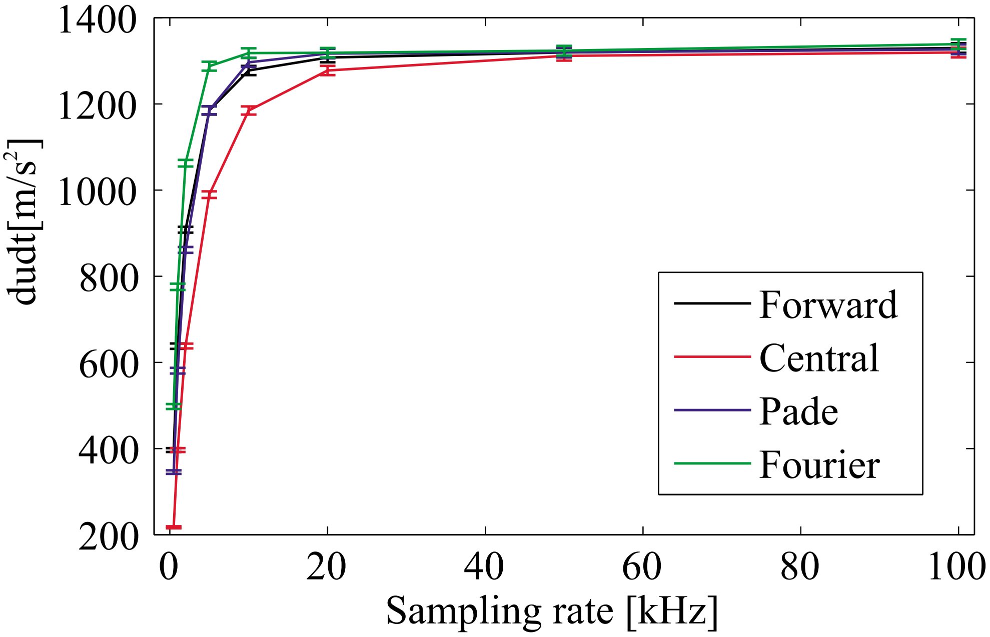

Figure 3.11: Effect of the sampling rate to estimated du/dt.

3.5 Calculation of time-derivative of velocity fluctuation

Using Eq. (3.6) to calculate fluctuating static pressure requires the time derivative of the velocity fluctuation $\partial u/\partial t$. The estimated time-derivative of the fluctuating velocity depends on the sampling rate and the differencing scheme. Here, four different schemes of numerical differentiation were tested: the upwind differencing scheme (UDS), the central differencing scheme (CDS), the padé approximation method and the spectral derivative (Moin, 2001). Figure 3.11 shows the rms of the estimated time-derivative of streamwise velocity against the sampling rate. The UDS exhibits slowest convergence and the Fourier derivative provides fastest convergence at 10 kHz. In following results, the spectral derivative was used to obtain the time-derivative.

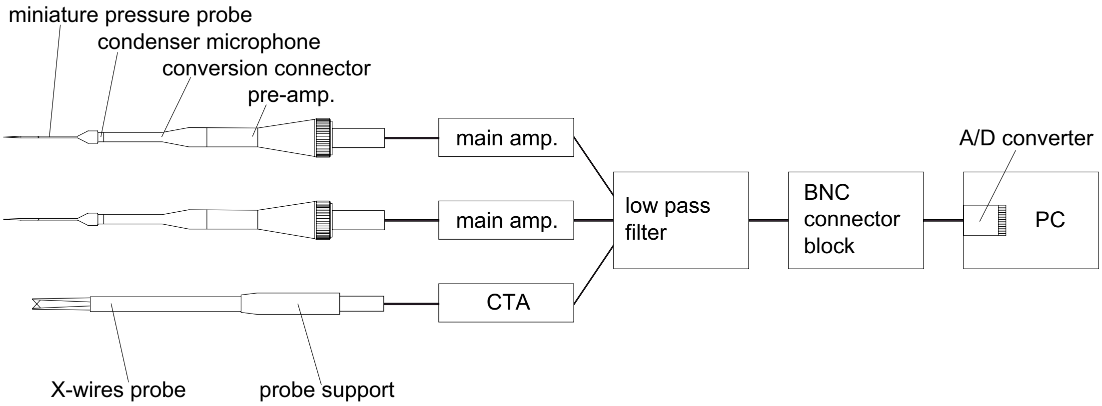

Figure 3.12: Diagram of measurement systems.

3.6 Data acquisition and data processing

The signals from the CTA and the main amplifier of the microphone were low-pass filtered by the analog-circuit low-pass filter (NF-3344) to avoid aliasing before the signals are transferred to a standard PC through a 16bit-A/D converter (NI PCI-6030E) and the connecting terminal (NI BNC-2120). Typically, the input voltage range of the A/D converter was set to ±5 V; the resultant quantization error can reach up to ±0.076 mV. The maximum sampling rate of this A/D converter is 100 kHz[1] All data acquisition was managed by LabView™(National Instruments) and further post data processing was handled by programs written in Matlab™(The Mathworks). The typical configurations of measurement systems are depicted in Fig. 3.12

3.7 Simultaneous measurements of velocity and pressure

3.7.1 Arrangement of the probes

The microphone and the hot-wire probe were mounted on a common unit to facilitate the traversing of them to arbitrary positions. The distance between the X-probe and

---

[1] Signals between two channel delays approximately 10 μs because one A/D converter is shared and multiplexed by 8 analog input channels.

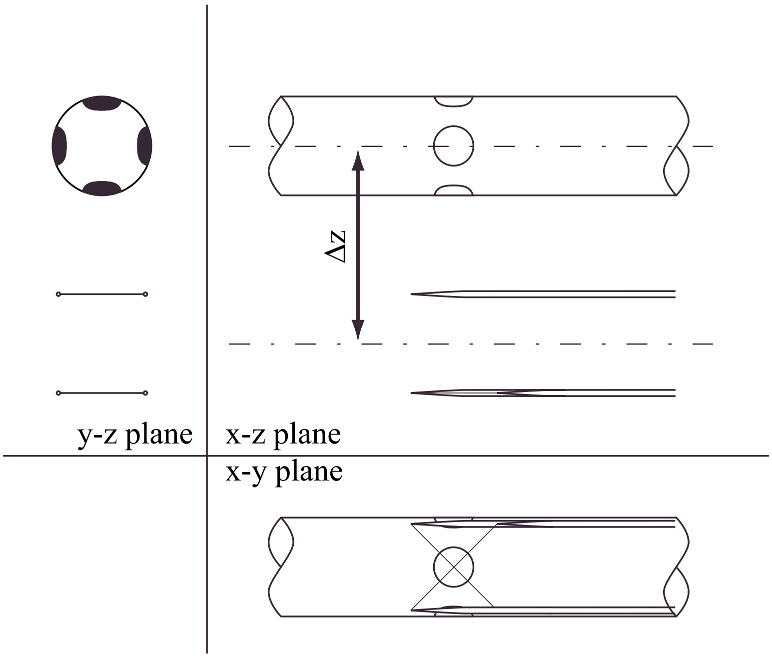

Figure 3.13: Spatial resolution of the SP- and X-probes.

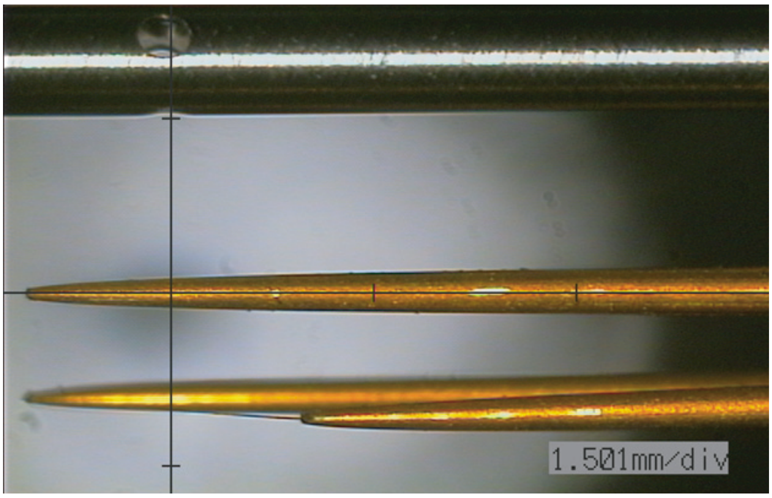

Figure 3.14: Probe arrangement view from bottom ($x-z$ plane).

either the SP- or TP-probes was adjusted by using a digital micro-scope (Keyence VH-6200) prior to every run.

3.7.2 Spatial resolution

A typical configuration of the SP- and X-probes is presented in Figs. 3.13 and 3.14. The distance between two probes noted as Δz is decided so that it can achieve both the velocity-pressure correlation as good as possible and the interference as small as possible based on the results in the turbulent mixing layer (see Section 4.3.2.2). In this case, the center-to-center probe distance Δz is determined to 2.5 mm. The spatial resolution of the simultaneous measurement using the SP- and X-probes is (L_x, L_y, L_z) = (0.88 mm, 0.88 mm, 2.5 mm).

Figures 3.15 and 3.16 illustrates the arrangement of the TP- and X-probes. The TP-probe was placed in between two sensors of the X-probe. The spatial resolution of the combined probe is (L_x, L_y, L_z) = (1.44 mm, 0.88 mm, 1.0 mm). The wire separation length in the z direction is 1.0 mm; the wire sensitivity length in the y direction is 0.88 mm; the streamwise distance between the virtual crossing point of the wires and the tip of the pressure probe is 1.0 mm. The streamwise distance was determined based on the consideration of the effect of probe proximity as described in Section 4.5.2.2.

3.7.3 Band-pass filtering

In the case of the indirect measurement of the fluctuating static pressure, the use of Eq. (3.6) requires the frequency response of the velocity and pressure signals to be identical. The condenser microphone does not have a flat response in frequencies lower than 20 Hz and the pressure fluctuations higher than 1 kHz are attenuated inside the TP-probe. In order to adjust the frequency characteristics of the measured total pressure and velocity, both signals were digitally band-pass filtered from 20 Hz to 600 Hz before applying Eq. (3.6). The filtering was achieved by the MATLAB™function “`filtfilt`” which can perform the digital filtering without introducing a phase-lag. Using this filtering procedure, the velocity and pressure fluctuations decreased to 88.2% and 92.0% of its level, respectively. In following sections, filtered signal was used only for calculating fluctuating static pressure by Eq. (3.6) while the velocity statistics were calculated from unfiltered signals.

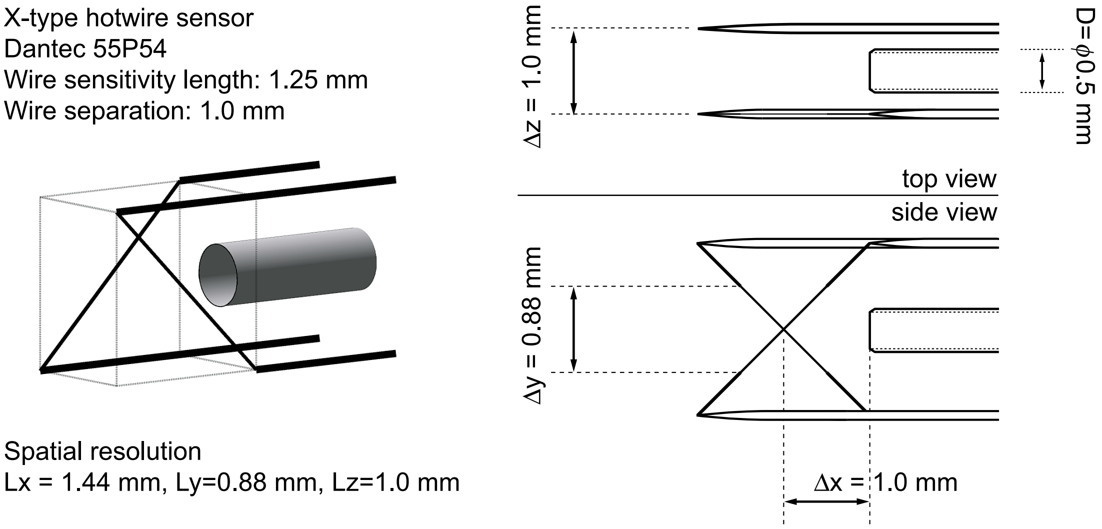

Figure 3.15: Spatial resolution of the combined probe.

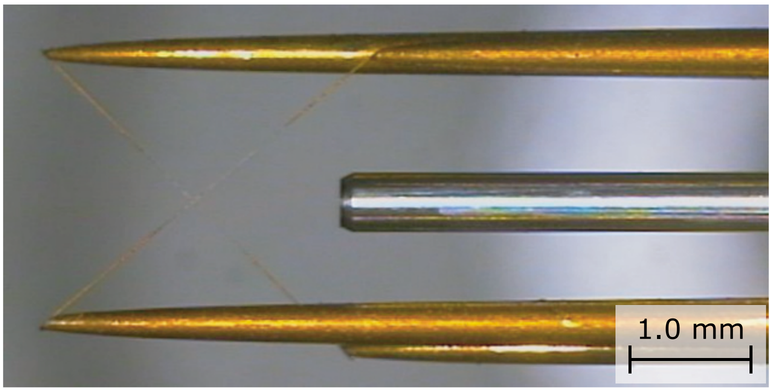

Figure 3.16: Side view of the arrangement photo ($x-y$ plane).

3.8 Other instruments

Figure 3.17 shows a self-fabricated precision manometer with 1:20 slanted tube and the position indicator of which minimum scale is 25 μm corresponding to the pressure head 3.3 Pa. This is used for the calibration of a low range pressure transducer (Validyne DP45-18), which is used with a standard Pitot-tube to obtain the reference velocity in the calibration of hot-wires. Instruments used in the present work are summarized in Appendix A.

Figure 3.17: Precision manometer.

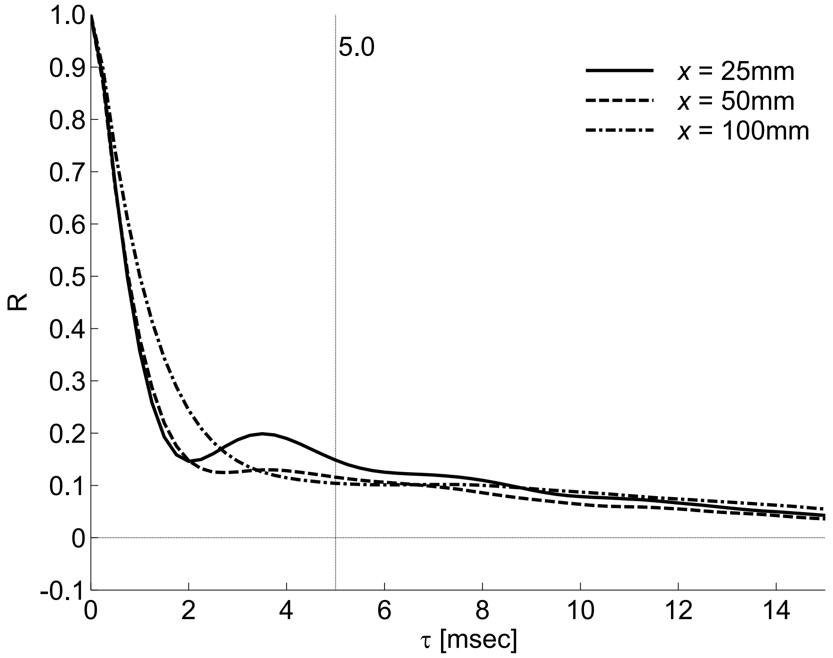

Figure 3.18: Auto correlation function of the streamwise velocity at the center of the turbulent mixing layer in different streamwise locations.

3.9 Uncertainty analysis

The evaluation of the measurement uncertainty is a requisite procedure. The source of the measurement uncertainty can be categorized into two groups: random error and systematic error. Several standards for the expression of the measurement uncertainty are available such as ASME PTC 19.1 (1986) and ISO GUM (1993)

3.9.1 Random error

The random error in the turbulence statistics, e.g. mean velocity, the Reynolds stress, pressure fluctuation and velocity-pressure correlation, depends on the number of samples to calculate the statistics. It is necessary to determine the appropriate number of samples to suppress the random error small enough. Here, a general procedure to estimate the random error is demonstrated using the data obtained in the center of the turbulent mixing layer. First, in order to check the independence of each sample, the auto-correlation function is checked. The typical distribution of the auto-correlation is

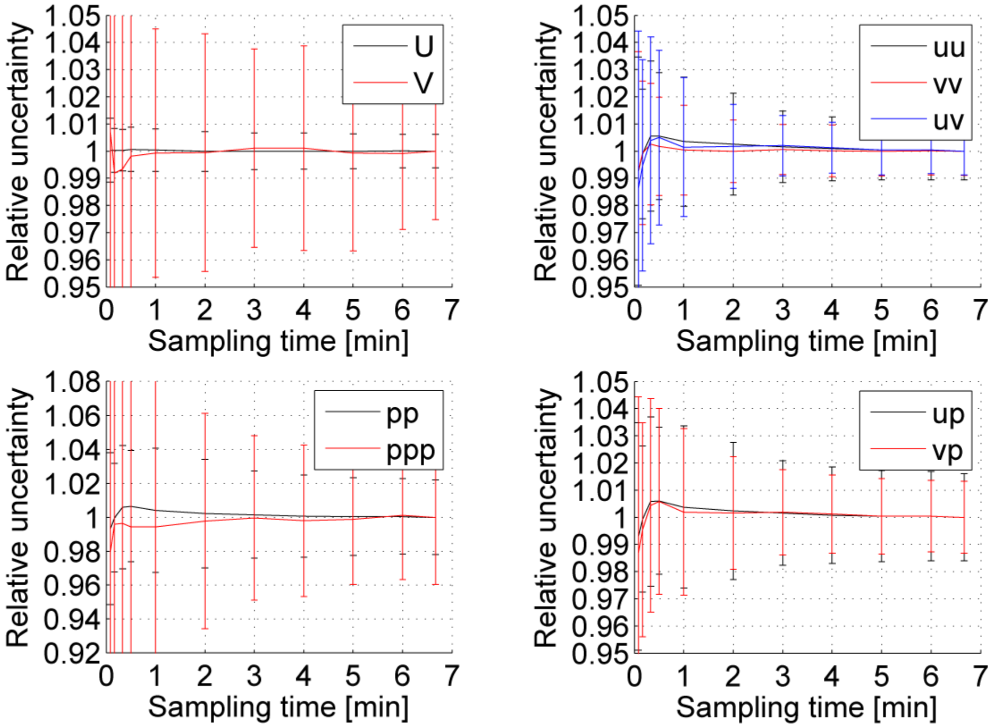

Figure 3.19: A typical graph for checking the random error as a function of the number of samples, N=15, Student *t*-value: 2.131.

shown in Fig. 3.18 at three different streamwise locations. In this case, sampling interval should be more than 5 ms to ensure the independence between adjacent samples in time.

Figure 3.19 indicates the typical variation of the random error against the sampling time checked in the middle of the mixing layer. When the sampling time was decided to three minutes, the corresponding relative random error is estimated to be 0.9% for the mean streamwise velocity, and 1.4% for the Reynolds stresses and 2.5% for the total pressure fluctuation.

The random error on each statistical value tS_X is calculated from the student t-value t and the precision index S_X. t for 95% confidence level is approximately 2 (it depends on the degrees of freedom) and the precision index is defined as:

$$S_X = \left[\frac{\sum_{k=1}^{N} \left(X_k - \overline{X_k} \right)}{N-1} \right]^{1/2}, \tag{3.7}$$

where X_k is the time averaged value calculated by the certain number of samples, and $\overline{X_k}$ is the grand average of many time averaged values.

3.9.2 Systematic error

The largest possible cause of systematic error on the velocity is the calibration error of hot-wire probes. This occurs due to the change of the environment, e.g., temperature change, drift of amplifier of pressure transducer. Figure 3.20(a) demonstrates a typical calibration curves of I-type hot-wire probe before and after the experiment. Although in the range of the velocity less than 2 m/s, the relative error caused in two calibration curve exceeds 2%, for the velocity higher than 2.5 m/s, two curves show very good agreement. Figure 3.20(b) presents the typical diagram of the relative error of the velocity magnitude and the yaw angle of the velocity vector obtained from the X-probe using the look-up table technique between calibrations before and after the measurement. The difference can be found in the distribution: basically, the larger error is found in the lower velocity range as for the velocity magnitude. On the other hand, for the angle of attack, no dependency for the velocity is found. In average, the errors in velocity magnitude and the angle of attack are approximately 0.95% and 0.07°, respectively.

Other possible reasons of measurement uncertainty are listed below:

- Fluctuating pressure measurement:
  - electric noise;
  - sensitivity mismatch;
  - frequency response of the system;
- Combined effect of velocity and pressure measurement:
  - disturbance due to probe proximity;
  - phase-lag between pressure and velocity;
  - insufficient spatial resolution;

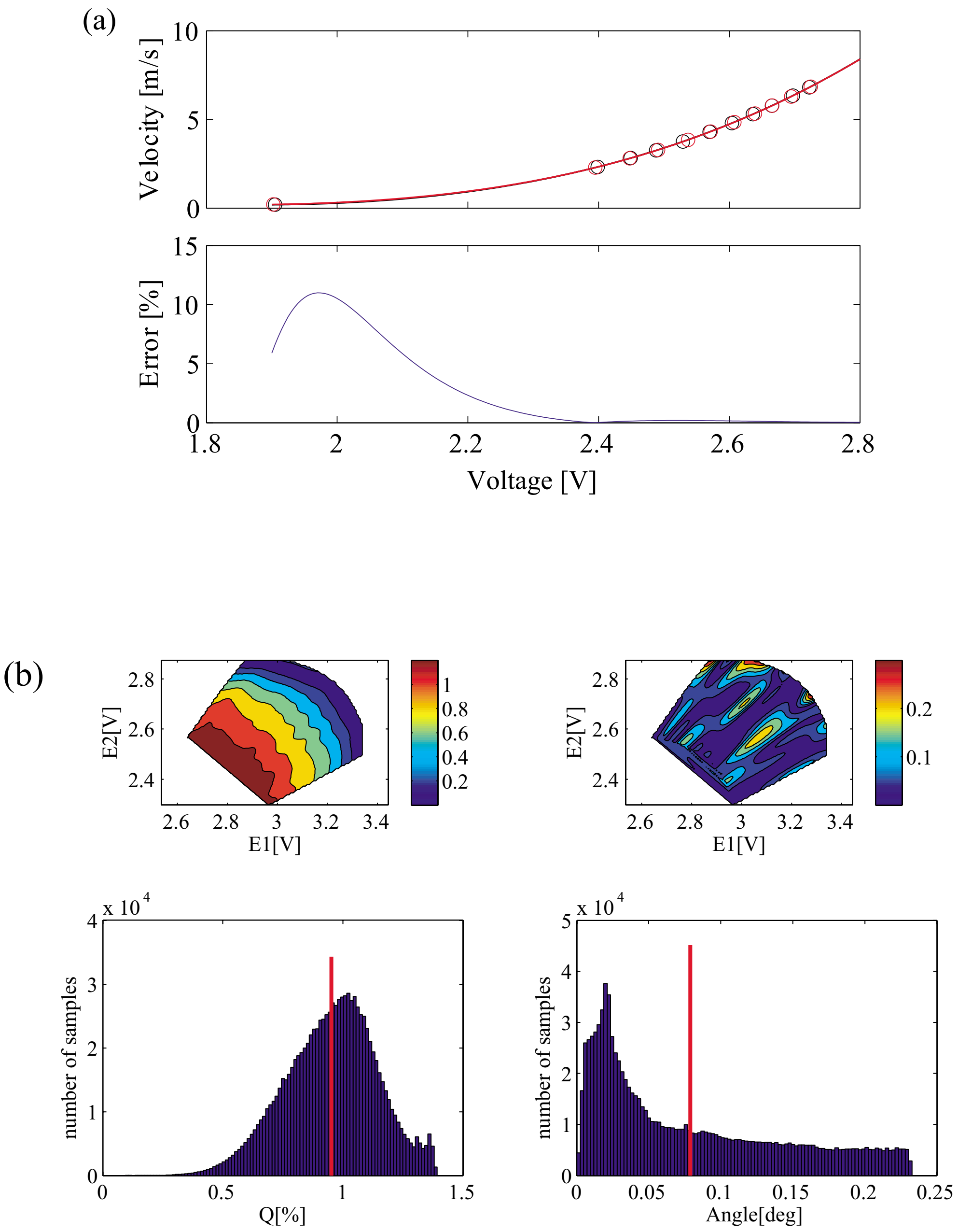

Figure 3.20: Effect of the time drift on the hotwire output; (a) I-type hot-wire probe, (b) X-probe.

Chapter 4

Measurements in a turbulent mixing layer

4.1 Analytical description of the turbulent mixing layer

In a statistical point of view, we can assume the two-dimensionality of the mixing layer. The spanwise mean velocity and the gradient in spanwise direction are negligible:

$$W \simeq 0, \quad \frac{\partial \overline{[]}}{\partial z} \simeq 0. \tag{4.1}$$

The correlation between spanwise velocity fluctuation is very small compared to $\overline{uv}$:

$$\overline{uw} \approx 0, \quad \overline{vw} \simeq 0. \tag{4.2}$$

When we look on the early developing region of the mixing layer, the following terms cannot be neglected unlikely the conventional thin-shear layer approximation:

$$\frac{V}{U} \neq 0, \frac{\partial []}{\partial x} \neq 0. \tag{4.3}$$

Based on the above mentioned considerations, the time-averaged continuity equations can be simplified as:

$$\frac{\partial U}{\partial x} + \frac{\partial V}{\partial y} = 0. \tag{4.4}$$

In addition to the simplification due to two-dimensionality, the viscous terms can be eliminated because the turbulent Reynolds number ($Re_T = uL/\nu$) is sufficiently high, where L is the representative length scale of large vortex. The RANS equations can be written as:

$$\rho\left(U\frac{\partial U}{\partial x}+V\frac{\partial U}{\partial y}\right)=-\frac{\partial P}{\partial x}+\mu\left(\frac{\partial^2 U}{\partial x^2}+\frac{\partial^2 U}{\partial y^2}\right)-\frac{\partial}{\partial x}(\rho\overline{u^2})-\frac{\partial}{\partial y}(\rho\overline{uv}), \tag{4.5a}$$

$$\rho\left(U\frac{\partial V}{\partial x}+V\frac{\partial V}{\partial y}\right)=-\frac{\partial P}{\partial y}+\mu\left(\frac{\partial^2 V}{\partial x^2}+\frac{\partial^2 V}{\partial y^2}\right)-\frac{\partial}{\partial x}(\rho\overline{uv})-\frac{\partial}{\partial y}(\rho\overline{v^2}). \tag{4.5b}$$

The transport equations of the Reynolds stress become:

$$\begin{aligned}\rho\left(U\frac{\partial\overline{u^2}}{\partial x}+V\frac{\partial\overline{u^2}}{\partial y}\right)=&-\left\{\frac{\partial}{\partial x}\left(\rho\overline{u^3}+2\overline{pu}\right)+\frac{\partial}{\partial y}\left(\rho\overline{u^2v}\right)\right\}\\&-2\rho\left(\overline{u^2}\frac{\partial U}{\partial x}+\overline{uv}\frac{\partial U}{\partial y}\right)+2\overline{p\frac{\partial u}{\partial x}}\\&-2\mu\left\{\overline{\left(\frac{\partial u}{\partial x}\right)^2}+\overline{\left(\frac{\partial u}{\partial y}\right)^2}+\overline{\left(\frac{\partial u}{\partial z}\right)^2}\right\},\end{aligned} \tag{4.6a}$$

$$\begin{aligned}\rho\left(U\frac{\partial\overline{uv}}{\partial x}+V\frac{\partial\overline{uv}}{\partial y}\right)=&-\left\{\frac{\partial}{\partial x}\left(\rho\overline{u^2v}+\overline{pv}\right)+\frac{\partial}{\partial y}\left(\rho\overline{uv^2}+\overline{pu}\right)\right\}\\&-\rho\left(\overline{u^2}\frac{\partial V}{\partial x}+\overline{v^2}\frac{\partial U}{\partial y}\right)+\overline{p\left(\frac{\partial u}{\partial y}+\frac{\partial v}{\partial x}\right)}\\&-2\mu\left(\overline{\frac{\partial u}{\partial x}\frac{\partial v}{\partial x}}+\overline{\frac{\partial u}{\partial y}\frac{\partial v}{\partial y}}+\overline{\frac{\partial u}{\partial z}\frac{\partial v}{\partial z}}\right),\end{aligned} \tag{4.6b}$$

$$\begin{aligned}\rho\left(U\frac{\partial\overline{v^2}}{\partial x}+V\frac{\partial\overline{v^2}}{\partial y}\right)=&-\left\{\frac{\partial}{\partial x}\left(\rho\overline{uv^2}\right)+\frac{\partial}{\partial y}\left(\rho\overline{v^3}+2\overline{pv}\right)\right\}\\&-2\rho\left(\overline{uv}\frac{\partial V}{\partial x}+\overline{v^2}\frac{\partial V}{\partial y}\right)+2\overline{p\frac{\partial v}{\partial y}}\\&-2\mu\left\{\overline{\left(\frac{\partial v}{\partial x}\right)^2}+\overline{\left(\frac{\partial v}{\partial y}\right)^2}+\overline{\left(\frac{\partial v}{\partial z}\right)^2}\right\}.\end{aligned} \tag{4.6c}$$

4.2 Inflow conditions of the turbulent mixing layer

The wind tunnel employed in the present study was specially designed for the turbulent mixing layer experiments. The schematic of the wind-tunnel is presented in Fig. 4.1. The inlet section of the tunnel is divided into two parallel parts, and the flow passes through a honeycomb, four fine meshes and the nozzle of which the contraction area ratio is 6.5. Then, the fully developed turbulent boundary layers with velocity difference merges at the test section of the 0.5 m × 0.5 m cross section. The free stream turbulence levels (FST) on high and low speed sides are approximately 1%. The inlet boundary layers are tripped by the wires located 150 mm upstream from the edge of the splitter plate. The thickness of the splitter plate edge is approximately 0.5 mm and it gradually becomes thicker with the angle 0.6°toward the upstream. The diameters of wires are 1.5 mm and 2.5 mm on high- and low-speed side, respectively so that the Reynolds number based on the free-stream velocity and the height of the tripping wire is approximately 600 (Barlow et al., 1999). The orthogonal coordinate system, originating from the trailing edge of the splitter plate, was defined, with the x- and y-axes taken in streamwise and transverse directions, respectively. The mixing layer was found to be uniform for at least 70% of the span, corresponding to 10 times of the mixing layer thickness.

Figures 4.2(a) and (b) show the profiles of the mean velocity and fluctuating velocity measured at $x = 0.5$ mm, respectively. Results are compared with DNS data of the turbulent boundary layer by Spalart (1988), and the measured distributions agree satisfactory with those of simulation. In the region near the wall, the time-averaged velocity and velocity fluctuation do not turn to be zero due to the vicinity of the wall (measurement location was at $x = 0.5$ mm).

Results of the boundary layer without the tripping wire are also shown. The distribution is quite different from that with the wire: the velocity gradient near the wall and the level of velocity fluctuation are small compared to the case with the wire. From the observations obtained here, it is fair to say that the inlet boundary layers were fully developed turbulent boundary layers.

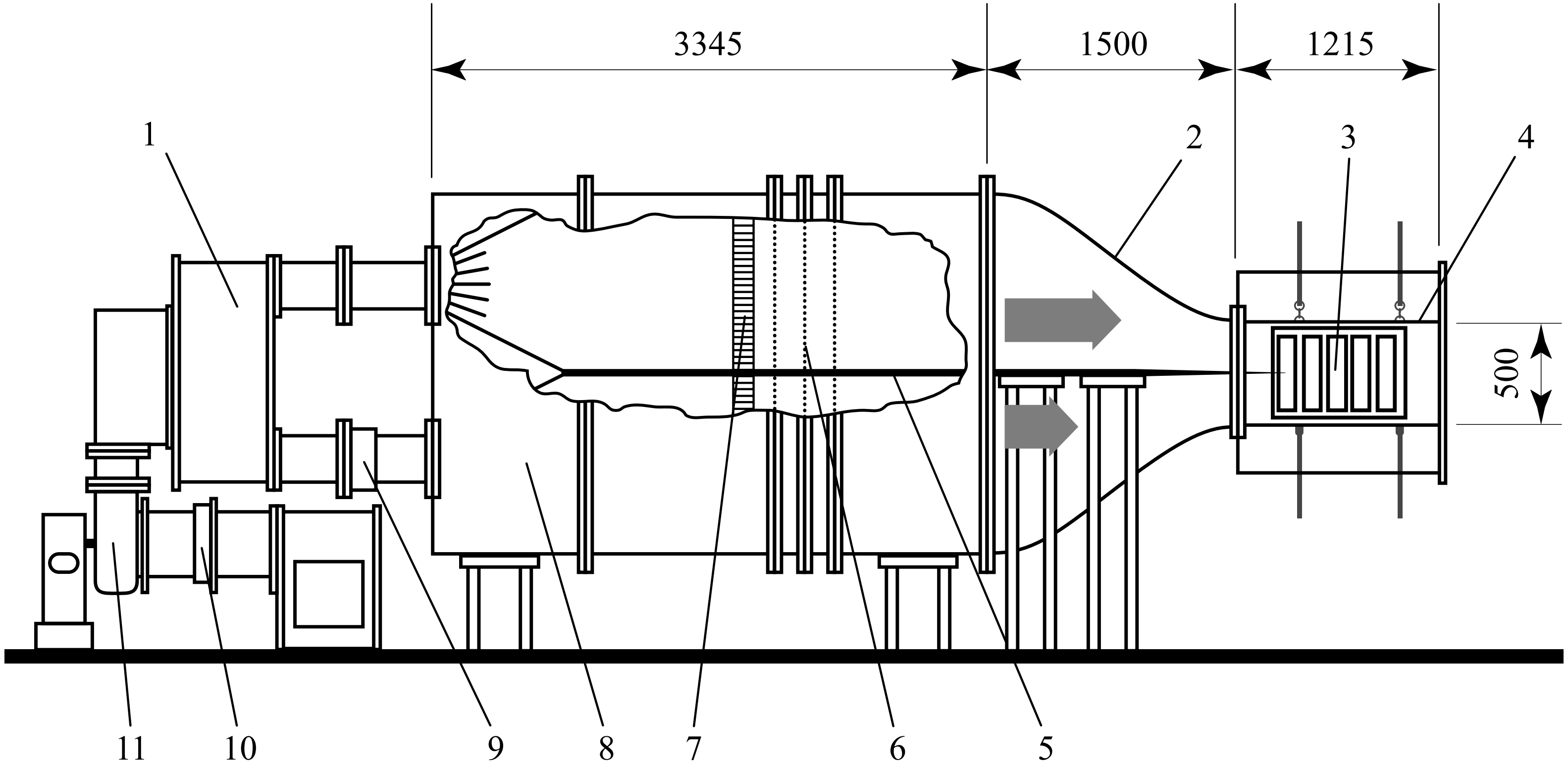

1	Dividing section	2	Nozzle	3	Test section	4	Variable wall
5	Splitter plate	6	Mesh	7	Honeycomb	8	Diffuser
9	Valve for lower duct	10	Main valve	11	Brower	12	Anti-vibration duct

Figure 4.1: Schematic of the mixing-layer wind tunnel.

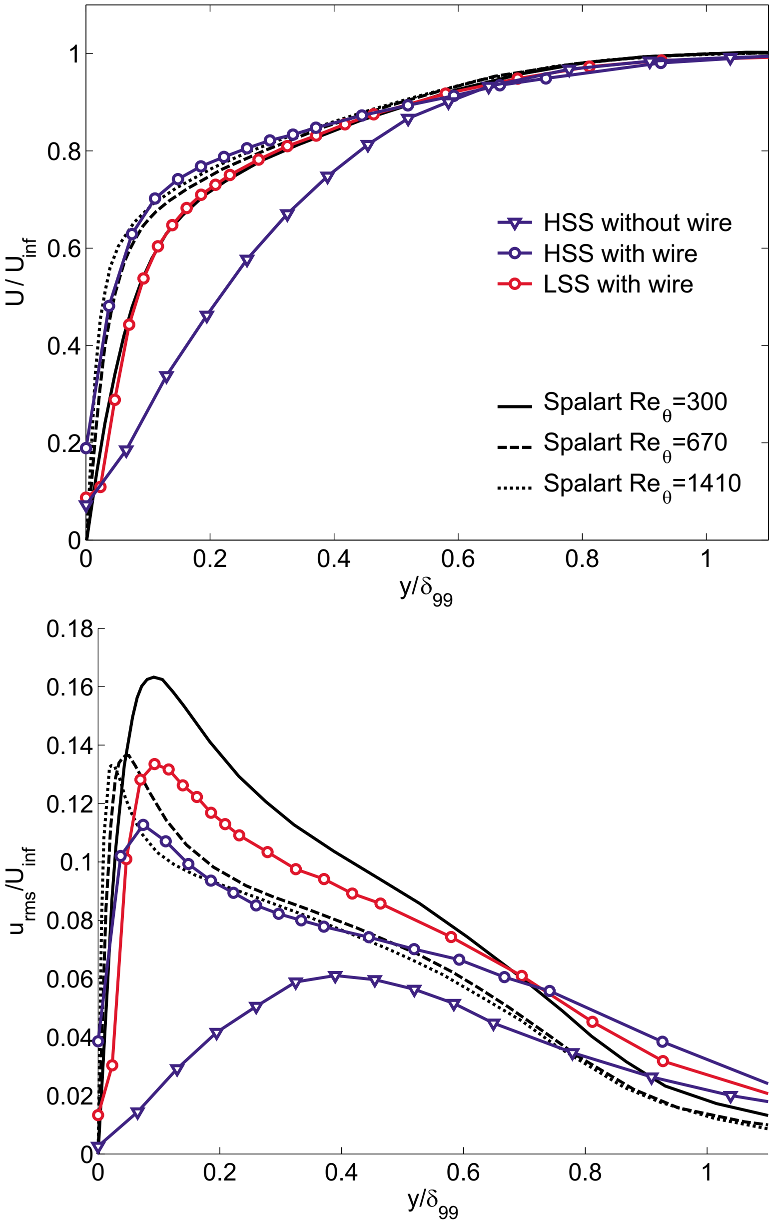

Figure 4.2: Inflow conditions at $x = 0.5$ mm in comparison with DNS results by Spalart (1988); (a) mean streamwise velocity, (b) streamwise velocity fluctuation.

4.3 Measurement by SP- and X-probes

4.3.1 Motivation

The importance of pressure fluctuation in turbulent flows has long been recognized and is still one of the unanswered questions in turbulence research. A number of experiments show that the correlation between fluctuating pressure and velocity, originating from large-scale vortex structures, plays a significant role in determining the budget of transport equations for turbulence properties. Numerous computational approaches have made great contributions toward the understanding of the dynamics of the inviscid flow and organized motion of vortices, but it is too complex to give the whole description of turbulent motions. Although there are lot of suggestions on the close relationships between pressure fluctuation and coherent turbulent fluid motion, the interaction of the velocity and pressure should be explored from various viewpoints.

Problems in the currently available turbulence models lie in the lack of physical characterization of the velocity-pressure correlation, particularly when the turbulence structure departs from the equilibrium state of turbulent kinetic energy. The conditions of flow out of the equilibrium state are far from ideal; one where calibrations of turbulence models are often undertaken, e.g. isotropic, homogeneous, or simple shear flows. As a consequence, the performance of existing models in predicting complex flows is not well established, unlike the case of simple shear flows. In order to develop better turbulence models for prediction of non-equilibrium flows, the key mechanism which is governed by the pressure-related turbulent motions must be addressed.

There are numerous efforts available for both experimental and computational approaches to understand the role of pressure fluctuation. Relatively little experimental researches about pressure-related statistics is available, mainly because of underlying technical difficulties in measuring static pressure fluctuation at arbitrary locations in the flow field. In his pioneering work, Kobashi (1957) combined the condenser microphone with a static pressure tube, and represents a step toward the evaluation of fluctuating pressure. With reference to his work, Toyoda et al. (1994) developed a probe to measure fluctuating pressure with sufficient accuracy in free shear flows. This type of pressure probe enabled an evaluation of fluctuating pressure, for example, Tsuji and

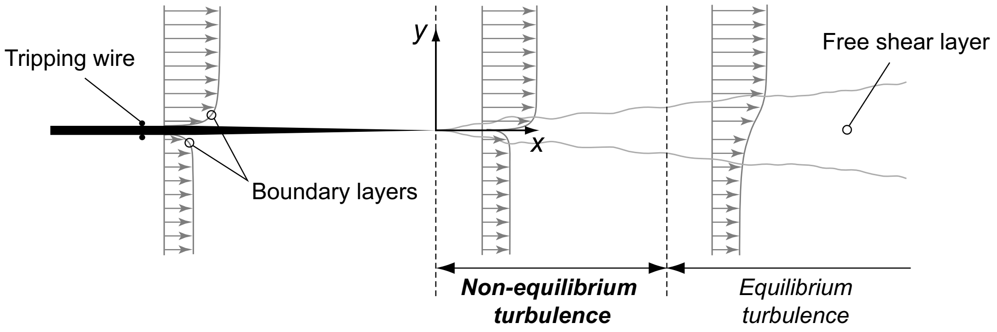

Figure 4.3: Schematic of the considered flow field.

Ishihara (2003) introduced this probe to reveal the power-law and proportional constant of normalized pressure spectrum. A recent study by Tsuji et al. (2007) reports a successful application of the technique in measuring the turbulent boundary layer.

The progress in computer technology has enabled direct numerical simulations (DNS) to be applied to increasingly complex flows with spatial development which contains remarkably large pressure fluctuation in contrast to simple flows. Yao et al. (2001) indicated in their DNS study on the transition from turbulent boundary layer along a flat plate to free shear layer that there are remarkable differences in the common features found in the fully developed channel flow. A temporally developing turbulent mixing layer was calculated by Rogers and Moser (1994) and it was indicated that both of the large scale rollers and finer scale ribs play an important role in representing the properties of the shear layer. Nevertheless, both computational and experimental approaches are required to better understand the role of pressure fluctuation in turbulent shear flows.

The present study focuses on the experimental approach to a relatively simple turbulent shear flow but out of an equilibrium state of turbulence. A spatially developing turbulent mixing layer is selected as the test case, where the gradual development of the oncoming turbulent boundary layer flow to the free shear flow is investigated. Particular attention is paid to the transitional stage of the kinetic energy balance through the non-equilibrium region before the shear layer develops to a self-similar state, as schematically shown in Fig. 4.3. An advanced technique for the simultaneous measurement of velocity and pressure is presented, which is based on our previous work (Omori et al., 2003), and discussions are presented on the existing simple model of

Table 4.1: Inlet conditions at $x = -50$ mm.

	U [m/s]	Tu$_f$ [%]	δ_b [mm]	Re
high speed side	7.2	0.76	18.8	610
low speed side	3.3	0.94	18.8	260

pressure-diffusion transport of Reynolds stresses.

Special attention is paid to retain the accuracy in the measurement of velocity-pressure correlation which is severely affected by temporal and spatial lags between two different signals. A phase-correction formula for the pressure signal, which is constructed by the information provided by the manufacturer, is introduced in the present study. Additionally, the inevitable effects of spatial interference between sensors is systematically investigated and explained in the following section, preceding the detailed discussion on the pressure-related turbulence statistics.

4.3.2 Experiments

4.3.2.1 Apparatus

Simultaneous measurements of fluctuating velocity and pressure have been performed using a thin static pressure probe and an X-type hotwire probe (Dantec 55P64) as described in Chapter 3. The calibration of the HWA signal was performed by a resolution of 0.3 m/s, ranging from 2.5 m/s to maximum speed; the resolution in direction was 3 degrees, covering from -30 to 30 degrees with respect to the main flow direction. Third-order polynomials were used to fit the curves on the plane composed of a pair of X-wires sensor voltage to obtain velocity variations for arbitrary angle of attack. The resulting look-up table had 80 intervals covering the full range in each sensor voltage, where the desired pair of velocity and angle was sought by use of a bi-linear interpolation function “`interp2`” available in the Matlab™library.

The conditions of the oncoming inlet boundary layers, measured at $x = -50$ mm, is summarized in Table 4.1. Tu$_f$ is the turbulence intensity outside the boundary layer and δ_b stands for the 99% thickness of the boundary layer. The Reynolds number Re is based on the free stream velocity U and the momentum thickness.

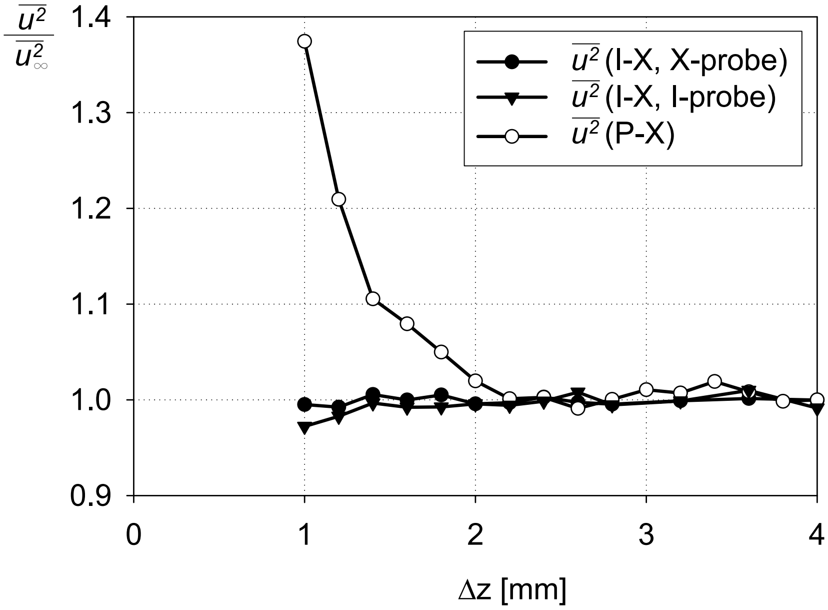

Figure 4.4: The interference of probe distance ($x = 100$ mm).

4.3.2.2 Interference of probes

The inevitable effects due to the departure of the pressure probe and the X-wires sensor on the measured velocity-pressure correlation have been investigated. In order to achieve a precise correlation, the two sensors used to measure each quantity should be set as close as possible to each other. On the other hand, using too close of a distance causes interference between the probes and eventually contaminates the signal. To determine the minimum distance between the probes where the sensors are free from the interference, we have measured the velocity fluctuation as a function of the probe distance Δz, where the z-coordinate is directed in the spanwise direction.

Figure 4.4 shows the streamwise velocity fluctuation measured by the X-wires probe, comparing those taken when the pressure probe is set aside (the plots ”P-X”) with those when the pressure probe is replaced by an I-type HWA sensor (”I-X, X-probe”), and, for reference, also with the data taken by the same I-type HWA in the proximity of the X-wires HWA (”I-X, I-probe”); the last plots may represent the disturbance due to the X-wires probe on the location of the pressure measurement. The measurements are undertaken at $x = 100$ mm and $y = 2.1$ mm where the velocity-pressure correlation $\overline{u^*p^*}$ is found to reach the maximum, as explained later. It is clear

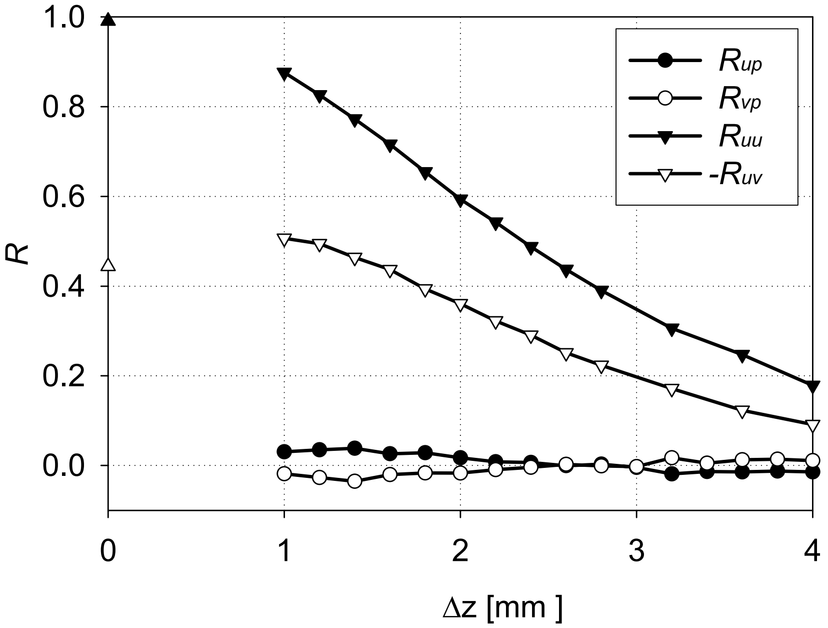

Figure 4.5: Correlation coefficient of velocity-velocity and velocity-pressure ($x = 100$ mm).

that the existence of the pressure probe strongly influences the velocity measurement by the X-wire sensor, as indicated by the steep increase of $\overline{u'^2}$ (P-X) for $\Delta z \leq 2$ mm. On the other hand, the data taken by the X- and I-type sensors in absence of the pressure probe show constant values down to $\Delta z \sim 1$ mm. It is inferred that the hot-wire sensors are small enough to prevent interference on the pressure measurements. Based on these arguments, the probe distance is fixed to 2 mm in the present study.

It is reasonable to consider that the measured velocity-pressure correlations are somewhat lower than the true values because of the finite distance between the probes. A rough estimation of this possible under-estimation is performed by referencing the two-point velocity correlation measured by the previously mentioned HWA-sensor combinations at the same location, see Fig. 4.5. The two-point correlation of the streamwise velocity fluctuation, R_{uu}, indicates a monotonic increase with the decreasing Δz. It should reach unity for the limit of $\Delta z = 0$, and the plots show a reasonable asymptotic tendency to this value. It should be noted that the distance between the sensors of X-wires itself is 1 mm, hence the data for Δz below 1 mm is not meaningful and not shown. The value of R_{uu} is about 0.6 at $\Delta z = 2$ mm, which implies that the velocity-

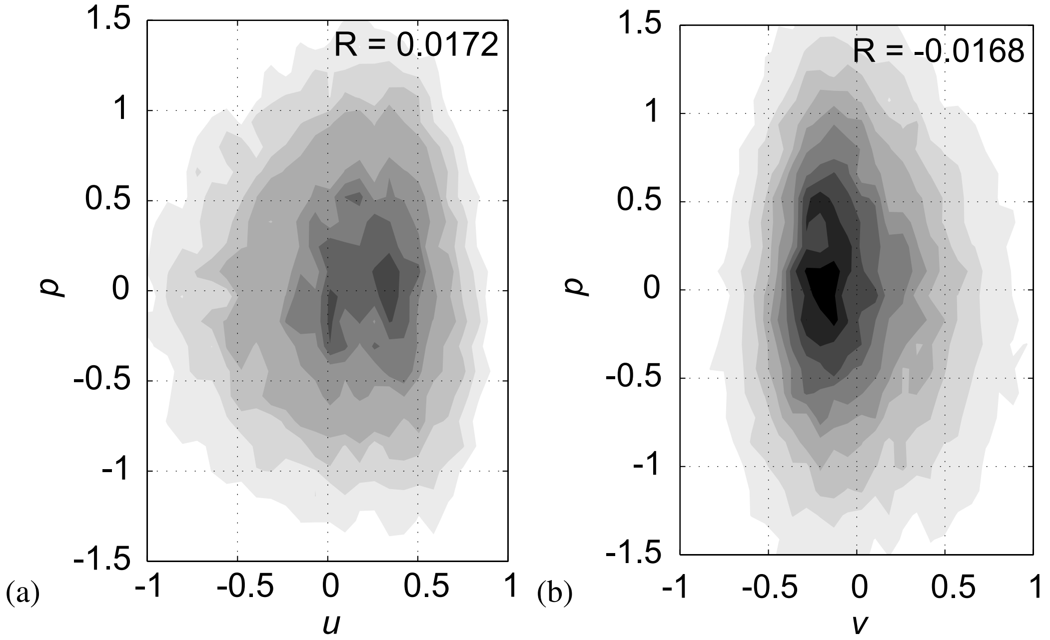

Figure 4.6: Joint-PDF of (a, u and p) and (b, v and p) ($x = 100$ mm).

pressure correlation measured for the probe distance of 2 mm may under-estimate the true value by 40%. On the other hand, the limiting value of the correlation between streamwise- and transverse-components of the fluctuating velocity, $-R_{uv}$, is approximately 0.45 at $\Delta z = 0$ in simple free shear layers (Bell and Mehta, 1990), and $-R_{uv}$ at $\Delta z = 2$ mm is smaller than this value by about 15%. From these observations, it is reasonable to conclude that the under-estimation of the velocity-pressure correlation measured in the present study may be on the order of 30%.

The plots for the variation of the velocity-pressure correlations, R_{up} and R_{vp}, drawn in the same figure indicate a slight increase of these quantities for Δz smaller than 2 mm, though these are a consequence of the increase in velocity fluctuation and do not necessarily indicate an increase in the correlation, i.e., the convergence to the true values. A closer investigation into the correlation map (joint probability density function) of the fluctuating velocity and pressure shown in Fig. 4.6 indicates that these quantities are not correlated as well as one might expect. A small fraction of the correlation coefficients, which are on the order of 10^{-2} as indicated in the figure, are due to the slight off set of the peak of the joint probability density function. It is easily understood that the small disturbance in velocity fluctuation alone results in an apparent increase in the correlation. The velocity-pressure correlation is a delicate quantity even in the highly turbulent flow regime.

4.3.2.3 Data processing

The statistics were calculated from 80,000 samples. A sampling rate of 4 kHz was selected to evaluate quantities that require high temporal resolution, such as energy spectra and derivatives with respect to time. For other statistics the sampling rate was fixed to 200 Hz which was found to be sufficiently high from the examination of auto-correlation of the velocity fluctuation. The resulting integration time was 400 s for turbulence statistics. Typically, it took about an hour by PC (Pentium4 2.8 GHz) to complete the post-processing of each measurement to draw a profile, comprising 49 points, across the mixing layer.

4.3.3 Results

4.3.3.1 Primary remarks

The velocity profiles across the shear layer are measured at three different streamwise locations, $x = 25$ mm, 50 mm and 100 mm. The development of the shear layer thickness, δ, was examined by means of the expansion factor of the free shear layer, $S = (U_c/U_s)(\Delta\delta/\Delta x)$ (Pope, 2000), with U_c being the convective velocity defined by $U_c = (U_h + U_l)/2$ where U_h and U_l are the free stream velocity of higher and lower velocity side, respectively, and U_s is the velocity difference, $U_s = U_h - U_l$. The value of S slightly decreases from 0.089, which is evaluated at the interval between 25 mm $\leq x \leq$ 50 mm, down to 0.086 at 50 mm $\leq x \leq$ 100 mm. The variation of S indicates that the shear layer is still under the development state.

4.3.3.2 Statistics of non-equilibrium turbulent mixing layer

The streamwise mean velocity profiles are shown in Fig. 4.7. The velocity U^* is normalized by the velocity difference U_s ($U^* = (U - U_l)/U_s$), and the non-dimensional coordinate η_θ is calculated using the momentum thickness of the shear layer at $x =$ 100 mm ($\eta_\theta = y/\theta$). It should also be noted that η_θ is geometrically fixed to the center

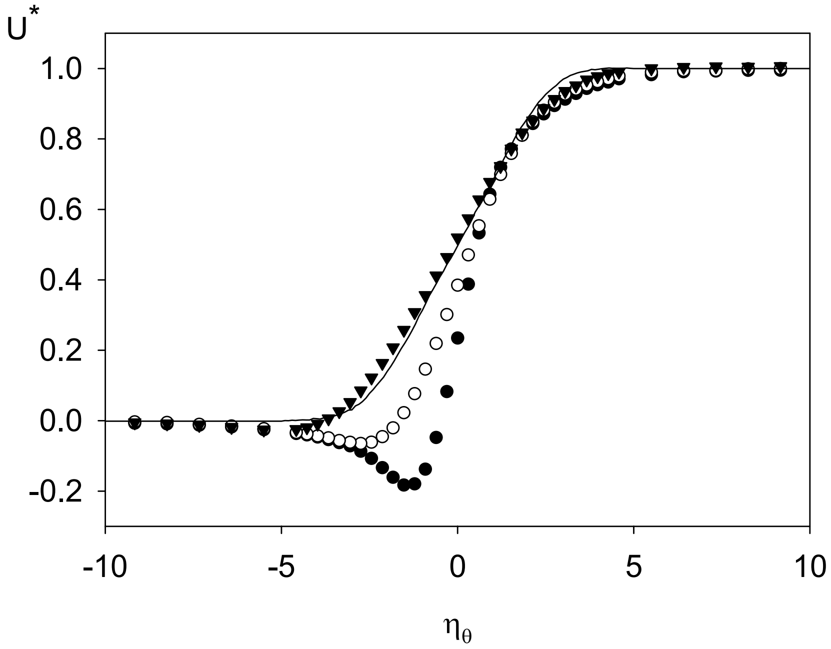

Figure 4.7: Profile of the streamwise mean velocity; Symbols • : $x = 25$ mm, ○ : $x = 50$ mm, ▼ : $x = 100$ mm, —— : DNS result of Rogers and Moser (1994).

of the splitter plate. The wake of the splitter plate is observed at all locations, in contrast to the profile of DNS by Rogers and Moser (1994) representing the self-similar state. The deficit in the velocity profile reaches $0.18U_s$ at $x = 25$ mm; it decreases down to $0.07U_s$ at 50 mm and still persists in the most downstream location, providing a slight under-shoot of the lower velocity side by $0.02U_s$ at $x = 100$ mm.

Figure 4.8 presents the profiles of the individual Reynolds stress component at the same location as for Fig. 4.7. It is shown that every component decreases downstream, with the $\overline{v^2}$-component indicating a slightly faster decrease when compared to the others. The values are still considerably higher than the reference DNS values even at the most downstream location. As the shear layer spreads in the direction of lower velocity side, or toward negative η_θ, the distribution becomes broader and asymptotes to symmetrical shape for all of the components. It is worth noting that the shear stress $\overline{uv}$ changes sign in the narrow region in accordance with the mean velocity distribution that exhibits a distinct wake-like shape.

The flow characteristics are further explored by means of the power spectrum den-

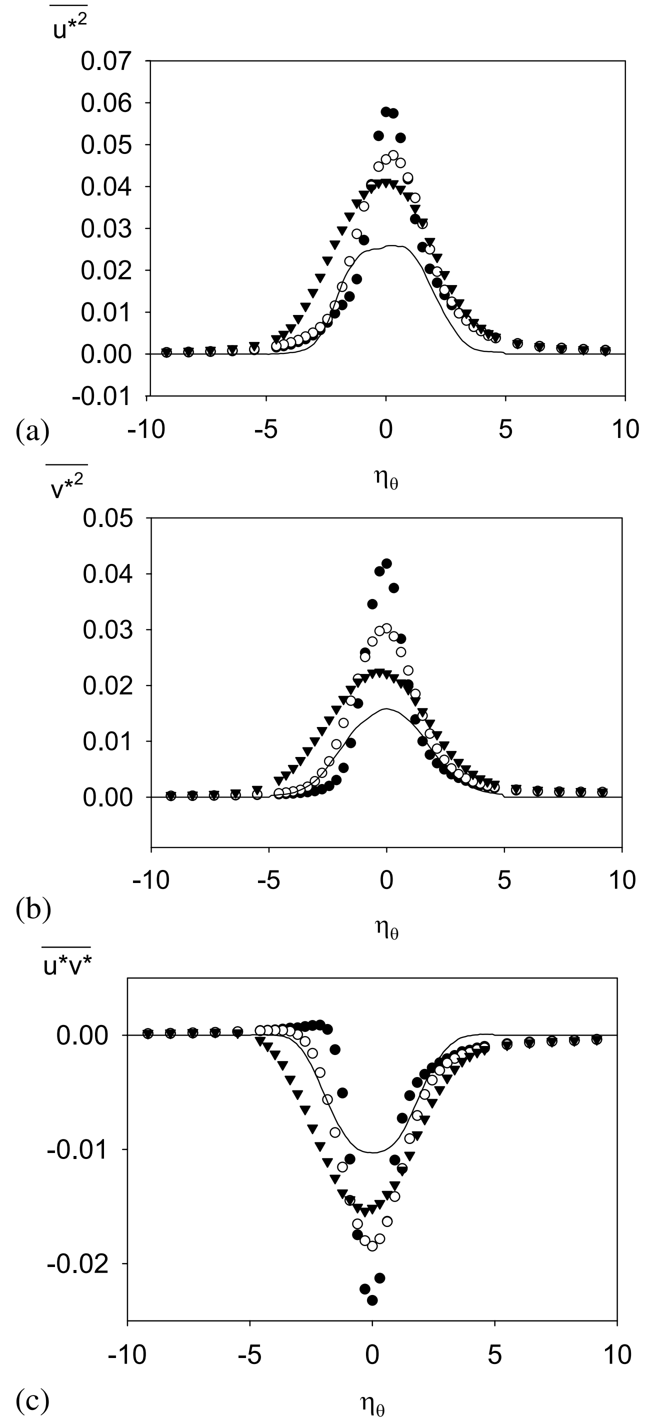

Figure 4.8: Components of Reynolds stress tensor; (a) $\overline{u^2}$, (b) $\overline{v^2}$, (c) $\overline{uv}$; Symbols • : $x = 25$ mm, ○ : $x = 50$ mm, ▼ : $x = 100$ mm, —— : DNS result of Rogers and Moser (1994).

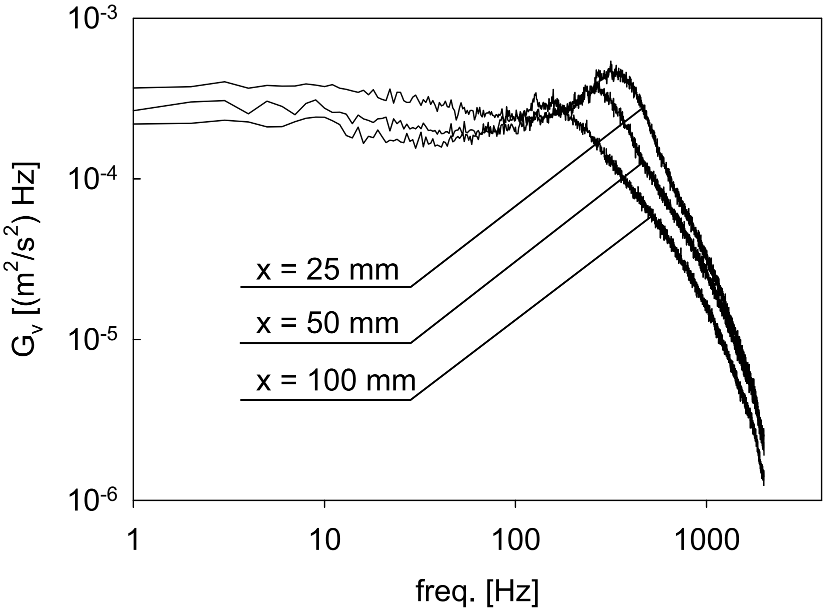

Figure 4.9: Power Spectrum of v.

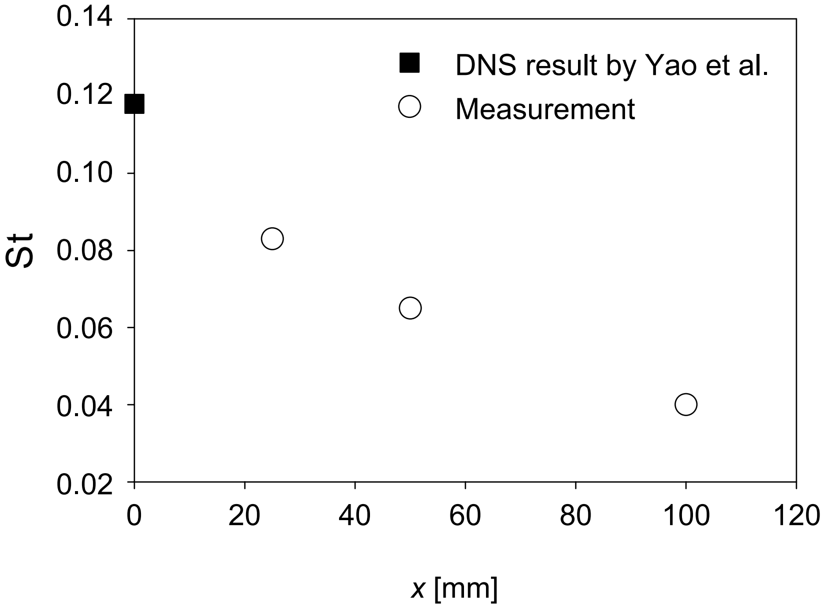

Figure 4.10: Variation of Strouhal number.

sity of the normal velocity component v, see Fig. 4.9, evaluated at $\eta_\theta = 0$. At the most upstream location, the distribution shows a peak near 330 Hz which corresponds to $St = 0.083$, with St being the Strouhal number based on the thickness of the splitter plate and U_s. Weaker peaks are also observed near 260 Hz and 160 Hz at $x = 50$ mm and 100 mm, respectively.

The characteristic frequency shown by the spectra is an indication of vortex shedding at a constant frequency, and the observed gradual decrease of the characteristic frequency is likely a consequence of vortex merging which occurs in the development stage. The DNS by Yao et al. (2001) reports a remarkable vortex shedding in the wake of a blunt body, with the Strouhal number 0.118 evaluated right behind the plate. Fig. 4.10 indicates streamwise variation of the characteristic frequency, and it is reasonable to consider that the periodic vortex shedding also exists in the present study especially near the trailing edge of the splitter plate. The influence of the vortex shedding gradually decays as the flow approaches to the self-similar state.

4.3.3.3 Velocity-pressure correlation in the shear layer

Figure 4.11 shows the velocity-pressure correlations $\overline{up}$ and $\overline{vp}$, which are directly measured by the present method, compared to those evaluated by the model by Lumley (1978) based on the triple-velocity correlation at the previously mentioned three streamwise locations:

$$\overline{up} \simeq -\frac{1}{5}\left(\overline{u^3} + \overline{uv^2}\right), \tag{4.7}$$

$$\overline{vp} \simeq -\frac{1}{5}\left(\overline{u^2 v} + \overline{v^3}\right). \tag{4.8}$$

It is shown that both $\overline{up}$ and $\overline{vp}$ significantly vary across the shear layer, changing their sign at the center, and $\overline{up}$ consistently exceeds $\overline{vp}$ in magnitude. The gradual decay of all quantities is also observed in downstream when comparing (a), (b) and (c).

Lumley's model provides relatively fair agreement for both components at the locations shown in Fig. 4.11 (b) and (c). An obvious departure is, however, evident in Fig. 4.11 (a) that is measured at the most upstream location, where Lumley's model yields an opposite sign for $\overline{up}$, and the magnitude of $\overline{vp}$ is over-estimated. These disagreements may be related to the existence of the characteristic frequency in the power density of the velocity fluctuation v, see Fig. 4.9.

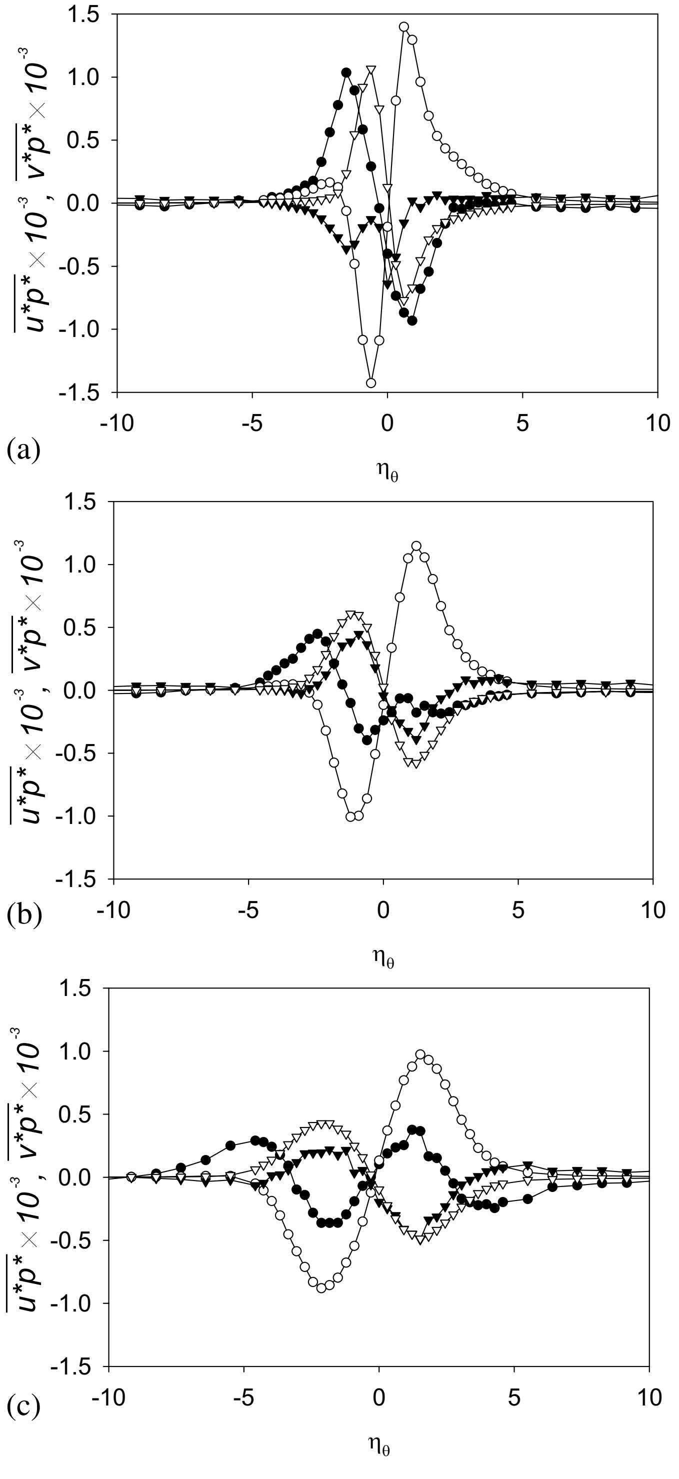

Figure 4.11: Profiles of $\overline{up}$ and $\overline{vp}$; (a) $x = 25$ mm, (b) $x = 50$ mm, (c) $x = 100$ mm; Symbols • : $\overline{up}$, ○ : $\overline{up}$ (Lumley model), ▼ : $\overline{vp}$, ▽ : $\overline{vp}$ (Lumley model).

Table 4.2: Terms of Reynolds stress transport equation.

	exact form	present form
P_{11}	$-2\rho\left(\overline{u^2}\frac{\partial U}{\partial x}+\overline{uv}\frac{\partial U}{\partial y}\right)$	$-2\rho\overline{uv}\frac{\partial U}{\partial y}$
Φ_{11}	$2\overline{p\frac{\partial u}{\partial x}}$	$-2\overline{p\frac{du}{dt}\frac{1}{\hat{u}}}$
P_{12}	$-\rho\left(\overline{u^2}\frac{\partial V}{\partial x}+\overline{v^2}\frac{\partial U}{\partial y}\right)$	$-\rho\overline{v^2}\frac{\partial U}{\partial y}$
D^t_{12}	$-\rho\left(\frac{\partial\overline{u^2v}}{\partial x}+\frac{\partial\overline{uv^2}}{\partial y}\right)$	$-\rho\frac{\partial\overline{uv^2}}{\partial y}$
D^p_{12}	$-\left(\frac{\partial\overline{pv}}{\partial x}+\frac{\partial\overline{pu}}{\partial y}\right)$	$-\frac{\partial\overline{pu}}{\partial y}$
P_{22}	$-2\rho\left(\overline{vu}\frac{\partial V}{\partial x}+\overline{v^2}\frac{\partial V}{\partial y}\right)$	$-2\rho\overline{v^2}\frac{\partial V}{\partial y}$
D^t_{22}	$-\rho\left(\frac{\partial\overline{u^3}}{\partial x}+\frac{\partial\overline{u^2v}}{\partial y}\right)$	$-\rho\frac{\partial\overline{u^2v}}{\partial y}$
D^p_{22}	$-2\frac{\partial\overline{pv}}{\partial y}$	$-2\frac{\partial\overline{pv}}{\partial y}$

4.3.4 Discussion

The significance of the velocity pressure correlation is further investigated in terms of the transport equation of the Reynolds stress:

$$\rho\frac{D\overline{u_iu_j}}{Dt}=P_{ij}+(D^t_{ij}+D^p_{ij}+D^v_{ij})+\Phi_{ij}-\varepsilon_{ij}, \tag{4.9}$$

where the terms on the right hand side, P_{ij}, D_{ij}, Φ_{ij}, and ε_{ij} represent production, diffusion, re-distribution and dissipation of the Reynolds stress $\overline{u_iu_j}$. Among the three diffusion transports, the molecular viscous transport D^v_{ij} may be neglected because of a large Reynolds number; the other two, i.e., the turbulent diffusion D^t_{ij} and the pressure diffusion D^p_{ij}, are of equal importance and primary concern. Table 4.2 summarizes some representative terms in the equation which are evaluated in the present study. Because of the restriction of the available quantities, only the terms on the right column of the table are evaluated. Also note that Taylor's hypothesis is applied to the estimation of the re-distribution term in the equation for the $\overline{u^2}$-component,

$$\Phi_{11} = 2\overline{p\frac{\partial u}{\partial x}} \simeq -2\overline{p\frac{du}{dt}\frac{1}{\hat{u}}}, \tag{4.10}$$

with $\hat{u}$ being the instantaneous streamwise velocity component.

Figure 4.12 presents the distribution of production and the re-distribution term in the $\overline{u^2}$-equation at three streamwise locations. The DNS result of Rogers and Moser (1994) are shown for reference to the equilibrium state. It is seen that the production rate far exceeds the re-distribution at $x = 25$ mm, though rapidly decreases in the downstream. At the most downstream location, $x = 100$ mm in (c), the measured values coincide well with the DNS result. It is found that the evaluated re-distribution term is consistently smaller than the production in magnitude. It should be noted that there is a narrow region, $-3 \leq \eta_\theta \leq -1$ at $x = 25$ mm (a), where the production and re-distribution show opposite signs.

The balance of the representative terms are also presented for the $\overline{uv}$- and $\overline{v^2}$-components in Figs. 4.13 and 4.14, respectively. For both components, the production P_{ij}, turbulent diffusion D^t_{ij} and pressure diffusion D^p_{ij} are compared. Similarly to the case for the $\overline{u^2}$-component, the production term is over-proportional to the others at the most upstream location, $x = 25$ mm, and rapidly decreases in the downstream. In particular, the production of $\overline{v^2}$, Fig. 4.14(a), exhibits remarkable magnitude, which is not the case for the self-similar state where the production P_{22} nearly vanishes.

The two diffusion terms, turbulent- and pressure-diffusion, of these two components indicate reasonable proportion; they are opposite in sign and the turbulent diffusion is consistently larger than its counterpart across the shear layer. Again, the situation at the most upstream location, $x = 25$ mm in Fig. 4.14, is a little different from the other two downstream locations, where the analogy between the turbulent- and pressure-diffusion is not likely to hold.

The above discussion points to the fact that the relatively simple approximation of the pressure diffusion by Lumley (1978) well represents the simple shear flow close to the self-similar state. However, the analogy between the turbulent- and pressure-diffusion gradually breaks down as the flow starts to exhibit certain characteristics such as the existence of vortex shedding, or the departure from the equilibrium state. The role of pressure fluctuation becomes more important as the complexity of turbulence structure increases.

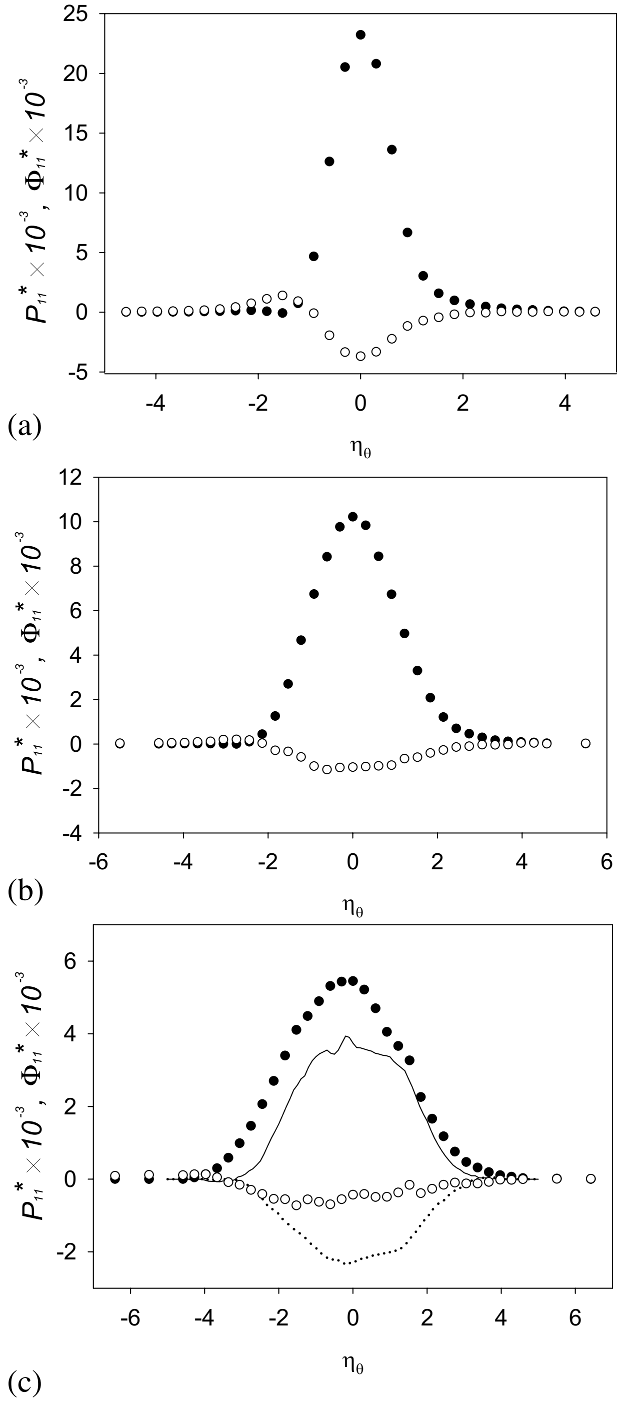

Figure 4.12: Estimated re-distribution Φ_{11}; (a) $x = 25$ mm, (b) $x = 50$ mm, (c) $x = 100$ mm; Symbols • : P_{11}, ○ : Φ_{11}, ——: P_{11} (DNS), ⋯⋯ : Φ_{11} (DNS), DNS data of Rogers & Moser (1994).

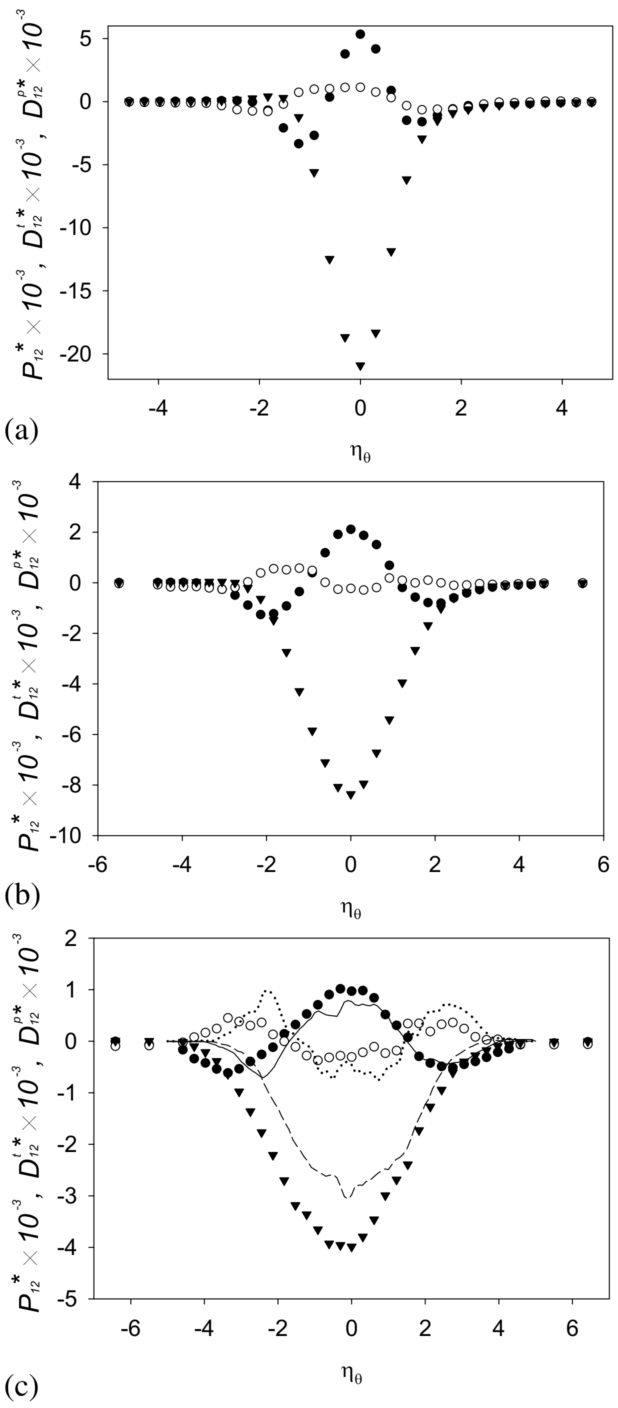

Figure 4.13: Estimated turbulent-diffusion D_{12}^t and pressure-diffusion D_{12}^p; (a) $x = 25$ mm, (b) $x = 50$ mm, (c) $x = 100$ mm; Symbols ● : D_{12}^t, ○ : D_{12}^p, ▼ : P_{12}, —— : D_{12}^t (DNS), ····· : D_{12}^p (DNS), - - - - - : P_{12} (DNS).

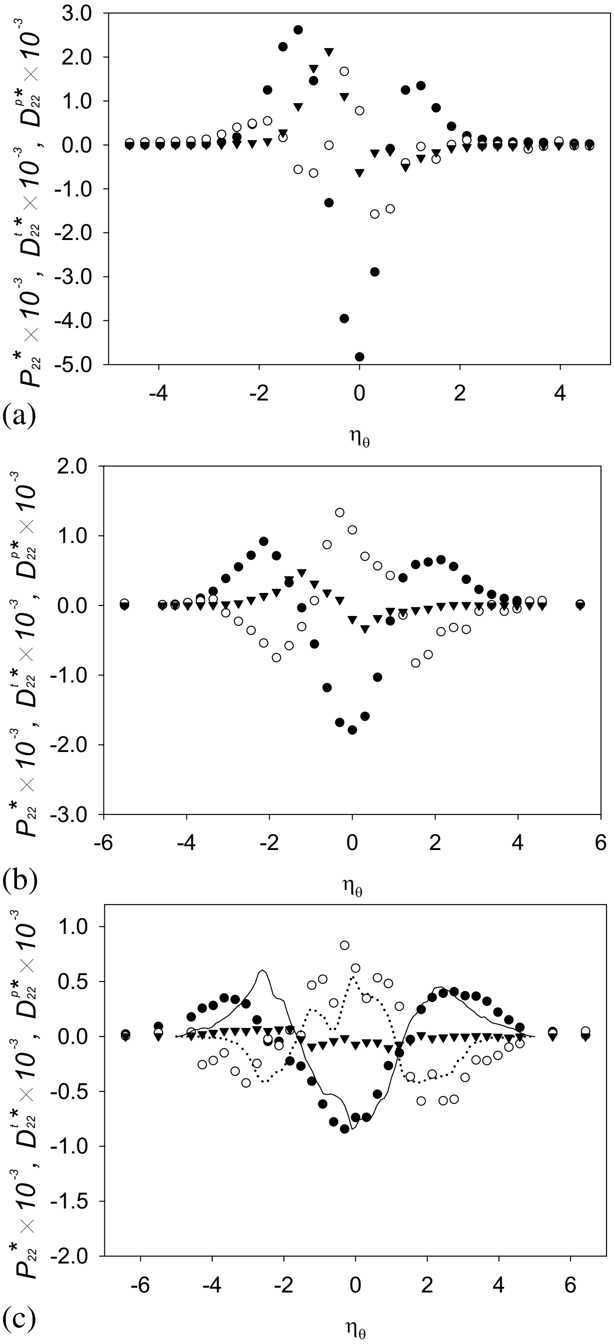

Figure 4.14: Estimated turbulent-diffusion D^t_{22} and pressure-diffusion D^p_{22}; (a) $x = 25$ mm, (b) $x = 50$ mm, (c) $x = 100$ mm; Symbols $\bullet$: D^t_{22}, $\circ$: D^p_{22}, $\blacktriangledown$: P_{22}, —— : D^t_{22} (DNS), $\cdots\cdots$: D^p_{22} (DNS).

4.3.5 Summary

The experimental evaluation of the pressure-related turbulence statistics has been undertaken in a free mixing layer out of equilibrium state. The noise reduction as well as phase-lag correction procedure is shown to be successful in evaluating the fluctuating pressure and the correlation between velocity and pressure. The distance between the pressure probe and X-wires has been carefully adjusted to minimize the interference and at the same time to retain the spatial resolution.

The characteristics of a spatial developing turbulent mixing layer were investigated with particular focus on the pressure-related quantities. Fundamental statistics are presented, and it is indicated that the flow characteristics are under development, showing remarkable velocity oscillation inherent to vortex shedding from the splitter plate. Velocity-pressure correlations are directly measured and compared with Lumley's model. The value of the Reynolds stress transport equation is examined, and the measured pressure-related terms were found to be in fair agreement with available DNS data. The analogy between the turbulent diffusion and pressure diffusion does not seem to hold in the region where the turbulence structure departs from that in the energy equilibrium state.

4.4 Integral length scale and coherence analysis

4.4.1 Motivation

Results of simultaneous measurement of the fluctuating velocity and pressure using the SP- and X-probes are presented in Section 4.3. As we demonstrated, the distance between the two probes was carefully chosen to achieve both interference free and as good correlation as possible. However, the required spatial resolution depends on the representative scale of the flow; therefore the spatial resolution of the present technique which corresponds to the probe distance of 2.5 mm as shown in Fig. 4.15 is compared to these scales.

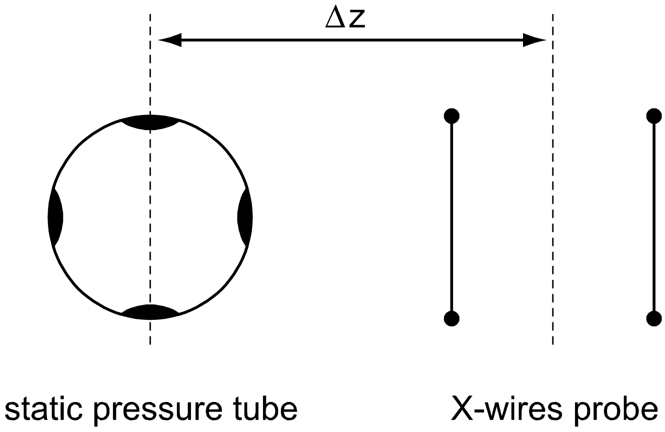

Figure 4.15: Arrangement of the SP- and X-probes.

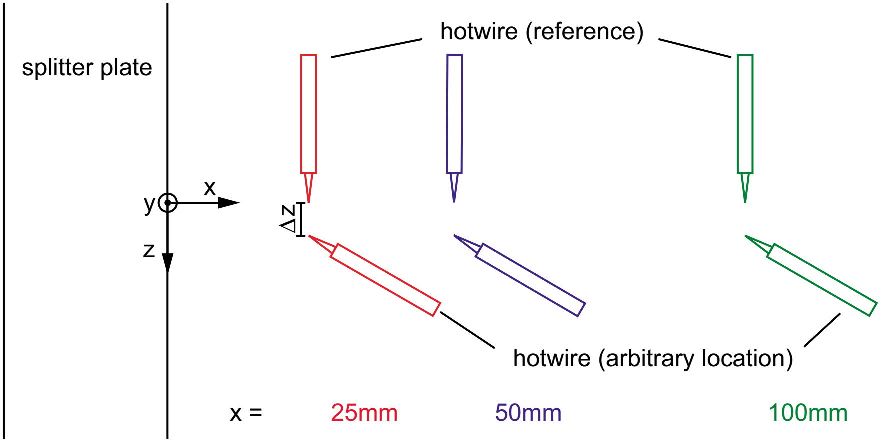

Figure 4.16: Probe arrangement for the velocity-velocity correlation measurement.

4.4.2 Measurement

Measurements were undertaken in the same mixing-layer wind-tunnel as described in the previous section. The simultaneous measurements of two streamwise velocity components with changing the spanwise distance Δz were performed at three different streamwise locations as described in Fig. 4.16 as well as the simultaneous measurement of the fluctuating velocity and pressure. Two I-type HWP sensors (Kanomax, 0251R-T5) were operated by CTA (Kanomax, 1011). The distance between the two probe ranged $0 \leq \Delta z \leq 8$ mm. The sampling rate of the measurement was chosen to be 4 kHz and the sampling time at each measurement position was 400 s.

4.4.3 Data processing

The integral length scale is evaluated from the distribution of correlation coefficient $R_{uu}(\Delta z)$.

$$\mathfrak{L} = \int_0^\infty R_{uu}(\Delta z) d\Delta z. \tag{4.11}$$

The integral length scale is the measure for the large-scale in the flow. For further understanding of the correlation, we evaluated cross spectra of the velocity-velocity and the velocity-pressure. Since the raw-cross spectra is complex number, the coherence and phase were evaluated for the physical interpretation of the cross spectra. Following equations were used to compute coherence, γ_c and phase, ϕ_p (Bendat and Piersol, 2000) (p.445):

$$\gamma_c{}^2(f) = \frac{|G_{xy}(f)|^2}{G_{xx}(f)G_{yy}(f)}, \tag{4.12a}$$

$$\phi_c(f) = \tan^{-1}[Q_{xy}(f)/C_{xy}(f)]. \tag{4.12b}$$

Here, cross spectra G can be defined as follows:

$$G_{xy}(f) = \frac{1}{N\Delta t}[X^*(f)Y(f)], \tag{4.13}$$

$$= C_{xy}(f) - jQ_{xy}(f), \tag{4.14}$$

where X and Y are the Fourier transformed signal. The cross-spectra is represented by its real- C_{xy} and imaginary- Q_{xy} part, respectively, in Eq. (4.14).

4.4.4 Results

Figure 4.17 indicates the profile of correlation coefficient between two streamwise velocity components as a function of the spanwise distance between the probes Δz at three different streamwise locations. The integral length scales $\mathfrak{L}$ are summarized in Table 4.3 to give a basic criteria for the spatial resolution. At the most downstream location, $\mathfrak{L}$ reaches 1.93 mm. It is fair to say that the spatial resolution is sufficient at this location because $\mathfrak{L}$ is nearly equal to the distance between the probes. However, at the most upstream location, $\mathfrak{L}$ decreases to 1.13 mm. This is only about the half of the distance between the probes. From the viewpoint of integral length scale, it can be said that the spatial resolution is insufficient at upstream locations.

Table 4.3: Integral length scale.

x [mm]	$\mathcal{L}$ [mm]
25	1.13
50	1.31
100	1.93

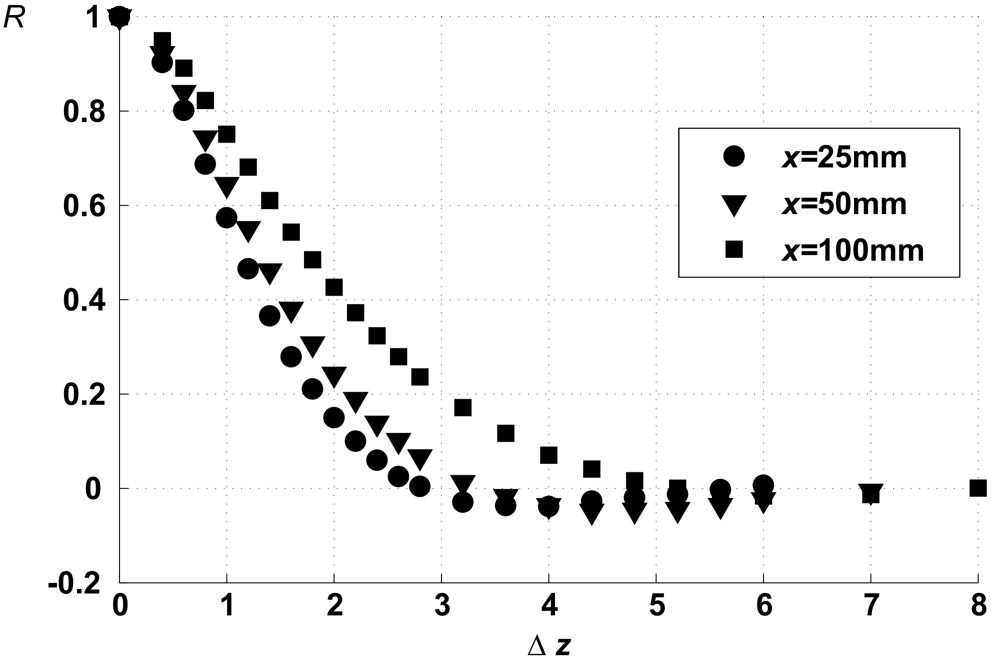

Figure 4.17: Spatial correlation function in the z direction at $y = 0$ mm.

Figures 4.18(a) and (b) show the distribution of the coherence of the velocity-velocity and velocity-pressure against spanwise distance and frequency at $x = 25$ mm, respectively. The velocity-velocity correlation is found that a highly coherent zone spreading over a broad frequency range where Δz is less than 1.0 mm as shown in Fig. 4.18(a). It is also noticeable that the indication of the organized motion as the distribution near 250 Hz. Figure 4.18(b) presents the coherence between velocity and pressure, and it is evaluated where velocity-pressure correlation takes maximum value. The distribution is quite different from that of velocity-velocity coherence. It is observed that the coherence between velocity and pressure near the characteristic frequency seems to be insensitive to the probe distance. As far as we are concerned with

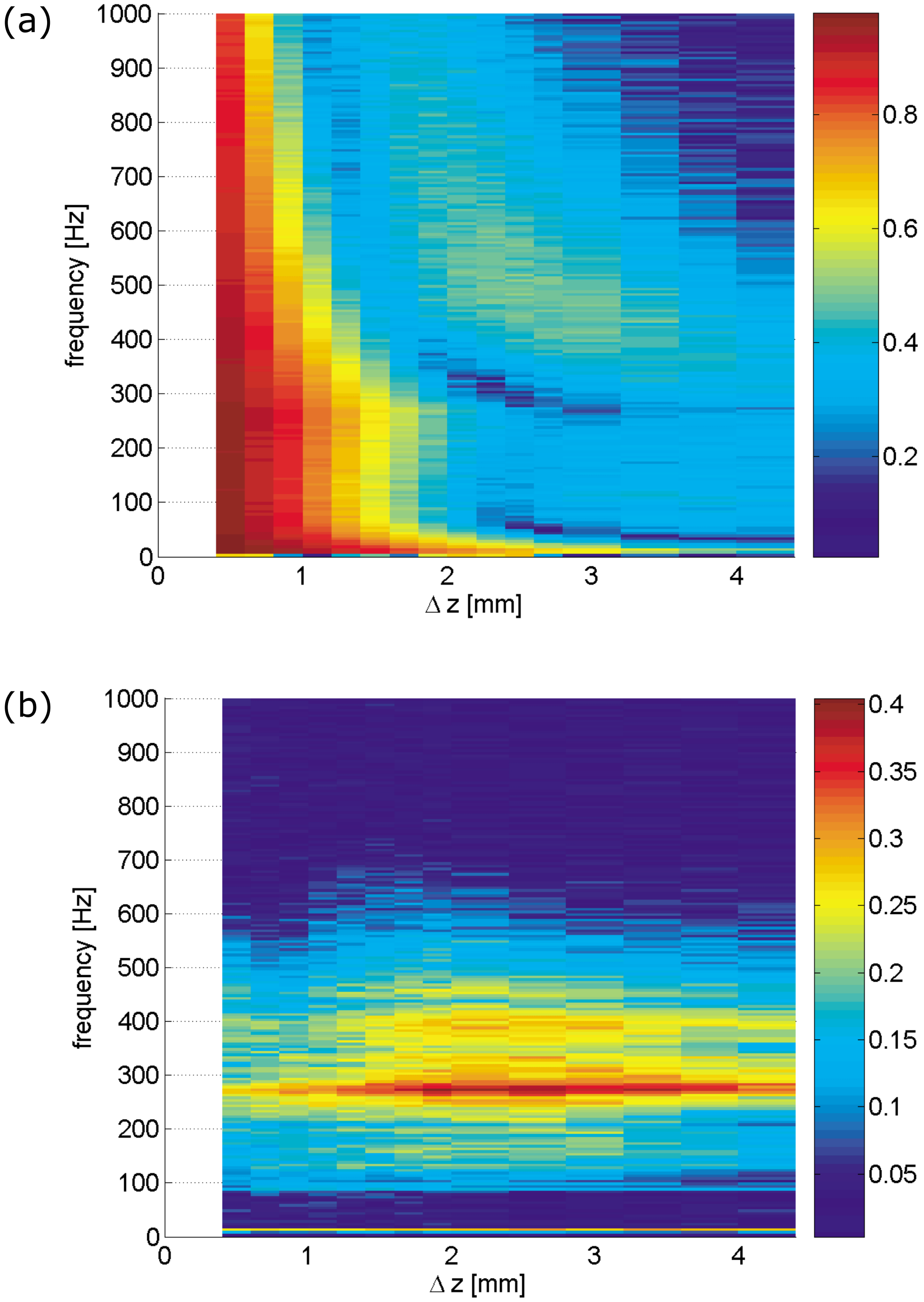

Figure 4.18: Cross spectra between; (a) velocity-velocity, (b) velocity-pressure.

the velocity-pressure correlation, our measurement with probe distance 2.5 mm is quite acceptable.

4.5 Improvement of the spatial resolution by TP- and X-probes

4.5.1 Motivation

It is well recognized that the velocity-pressure correlation largely contributes to the transport of the turbulent kinetic energy or the Reynolds stress, particularly in non-equilibrium turbulent flows. Yao et al. (2001) indicated that the pressure-diffusion term becomes significant in the wake of a thick rectangular plate. Suga (2004) proposed a turbulence model with the rapid part of the pressure-diffusion process taken into account. Complementary approaches by appropriate experimental techniques are also necessary in order to understand the pressure-diffusion process of turbulent flows.

Following the pioneering work by Toyoda et al. (1994), the miniature Pitot tube has been successfully applied to the measurement of fluctuating pressure in various turbulent flows, including a turbulent jet (Tsuji and Ishihara, 2003), a plane turbulent mixing layer (see Section 4.3), and a turbulent boundary layer (Tsuji et al., 2007). The local measurement of fluctuating static pressure presently belongs to standard experimental techniques.

In the previous Section 4.3, an attempt has been made to evaluate the pressure-diffusion transport of the Reynolds stresses. The simultaneous measurements of fluctuating velocity and pressure by an X-type hot-wire probe (X-probe) and a static pressure probe (SP-probe) were performed in a turbulent mixing layer. The estimated pressure-diffusion terms showed reasonable agreement with the available DNS data (Rogers and Moser, 1994) where flow achieved the self-similar state, though the reliable application of this technique was rather limited due to the spatial resolution of the combined probe system. The spatial resolution was of about 2.5 mm which was defined by the center-to-center distance between the SP-probe and the X-probe.

In order to improve the spatial resolution, we have developed a method where a miniature probe for measuring fluctuating total pressure (TP-probe) was combined

Table 4.4: Inlet conditions at $x = 0.5$ mm.

	U [m/s]	Tu$_f$ [%]	θ_b [mm]	Re	H
high speed side	6.78	0.86	0.88	398	1.41
low speed side	3.52	1.03	1.41	330	1.69

with the X-probe. Similar attempts have been made in the past by Giovanangeli (1988) and Nasseri and Nitsche (1991), though this method has yet to be assessed. Despite drawbacks involving the fact that the static pressure cannot be directly measured, this technique is capable of achieving spatial resolutions of about 1 mm cube – nearly equal to that of the X-probe itself.

In the present study, the above-mentioned techniques have been applied to the measurement in the developing region of a turbulent mixing layer and in the wing-tip vortex flow. In the former case, the reliability of the results obtained by the TP- and X-probes is examined in reference to the measurements undertaken by a combination of the SP- and X-probes.

4.5.2 Techniques for simultaneous measurement of total pressure and velocity

4.5.2.1 Instrumentation and data processing procedure

Experiments were performed in a mixing layer wind tunnel described in Section 4.2 which has 0.5×0.5 m^2 section. The origin of streamwise and transverse coordinates, x and y, were defined at the edge of the splitter plate. The spanwise coordinate z was taken with its origin being the center of the splitter plate. The inflow conditions of mixing layer, which are parameters of oncoming boundary layers on higher and lower velocity sides, are summarized in Table 4.4.

The TP- and X-probes were placed in the flow as described in Chapter 3. An X-type hotwire probe (Dantec 55P54) was operated by a CTA and the look-up table method by Lueptow et al. (1988) was employed to obtain two velocity components. The yaw-angles for building the look-up table ranged ±42° with the increment of 4.2°. Samples falling out of the calibration range (at most 0.45% of the total number of samples) were processed by the effective angle calibration method (Browne et al., 1989).

4.5.2.2 The effect of streamwise distance between probes

The interference of the distance between the TP- and X-probes was experimentally investigated. A series of measurements was undertaken for various locations of the TP-probe that was gradually moved along the probe axis. The streamwise distance between the virtual crossing point of the two wires in the X-probe and the tip of the TP-probe was defined as Δx, cf. Fig. 3.15. As shown in Fig. 4.19, the streamwise mean velocity U, the Reynolds stresses $\overline{u^2}$, $\overline{v^2}$, $\overline{uv}$, the fluctuating total pressure $\overline{p_t^2}$, the correlation of the velocity and the total pressure, $\overline{up_t}$ and $\overline{vp_t}$, are presented as functions of Δx. All variables were normalized by the reference value measured by each probe independently. The correlations $\overline{up_t}$ and $\overline{vp_t}$ were normalized by $\left(\sqrt{\overline{u^2}}\sqrt{\overline{p_t^2}}\right)$ and $\left(\sqrt{\overline{v^2}}\sqrt{\overline{p_t^2}}\right)$, respectively.

The streamwise mean velocity U decreases from unity to 0.97 as Δx decreases from $4D$ to $1.2D$ (D being the outer diameter of the pressure probe) before increasing to 1.02 at $\Delta x = 0$. Among the s-moments of fluctuation, $\overline{v^2}$ seems to be most sensitive to the probe interference, showing an increase at $\Delta x = 0$ by 10% relative to the value taken without the probe interference. The profiles of $\overline{u^2}$ and $\overline{uv}$ show the constant decrease as Δx changes from $4D$ to $1.2D$ followed by an increase in $\Delta x \leq 0.8D$. On the other hand, $\overline{up_t}$ and $\overline{vp_t}$ vary monotonically for the entire range of Δx. It is obvious that $\overline{up_t}$ increases linearly with the decreasing Δx but the slope changes at $\Delta x \simeq 4D$. A similar change of the slope is also seen in the variation of $\overline{vp_t}$.

According to these observations, the effect of the probe interference is estimated to be on the order of 3.5% for turbulence statistics when the probe distance is chosen for $2D \leq \Delta x \leq 4D$. In the subsequent measurements, the probe distance was set to $2D$, which corresponds to 1.0 mm.

4.5.3 Development of a turbulent mixing layer

4.5.3.1 Experimental conditions

A mixing layer wind tunnel employed in the present study was described in detail in Section 4.2. Simultaneous measurements of fluctuating velocity and pressure were undertaken at four different streamwise locations, $x = 25$, 50, 100 and 150 mm, and

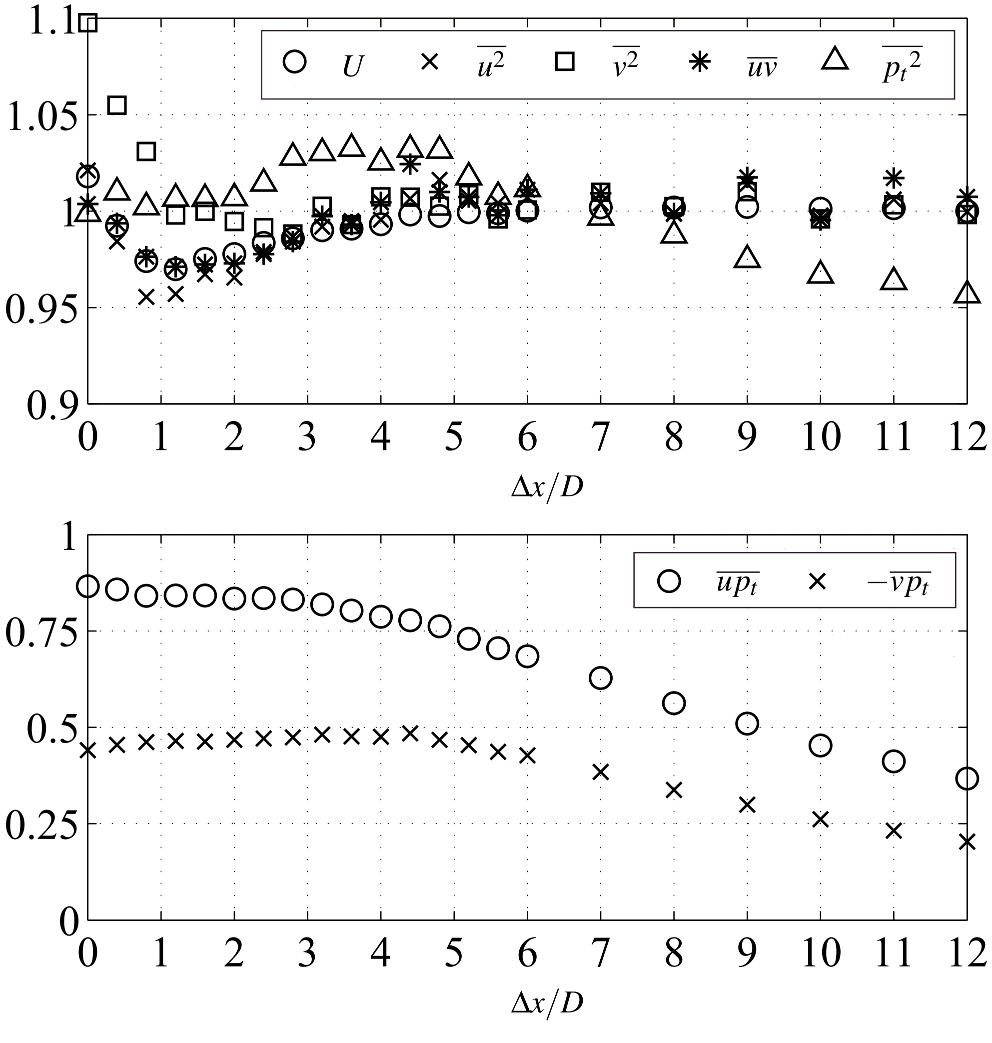

Figure 4.19: The effect of probe proximity; Mean streamwise velocity, Reynolds stress components and total pressure fluctuation (top), the correlation between velocity and total pressure (bottom).

the probes were traversed in the transverse direction over the range of -25.2 mm $\leq y \leq$ 25.2 mm. The origin of streamwise and transverse coordinates, x and y, were defined at the edge of the splitter plate. A non-dimensional transverse coordinate η $(= y/\theta)$ was defined by the momentum thickness θ at $x = 150$ mm ($\theta = 2.83$ mm). The velocity and pressure were also normalized by the free stream velocity difference ΔU and $\rho(\Delta U)^2$, respectively.

The sampling rate was set at 20 kHz and the cutoff frequency of the low-pass filter at 2 kHz. It was confirmed that this sampling rate was sufficiently high to evaluate time derivatives in Eq. (3.6). The sampling time was 180 s at each measurement position. The uncertainties in the measurement of U and $\overline{uv}$ at $(x, y) = (100 \text{ mm}, 0 \text{ mm})$ were estimated to be $\pm 0.7\%$ and $\pm 1.4\%$, respectively.

4.5.3.2 Results

The development of the distributions of the streamwise mean velocity and the Reynolds shear stress are shown in Fig. 4.20. At $x = 25$ mm, the distinct feature of the splitter plate wake is observed, e.g. a significant deficit of the mean velocity and the asymmetric shape of the profile of the Reynolds shear stress. The distributions gradually develop as they move downstream and eventually resulting in the conventional turbulent mixing layer. The profiles obtained by the two methods show good agreement with each other; the difference of $\overline{uv}$ is approximately 3.3% at the center of the mixing layer. It is fair to say that no significant probe interference exists in both experiments.

The rms value of the fluctuating pressure p' at the same locations are presented in Fig. 4.21, comparing the results measured by the SP- and the TP-probes. The static pressure fluctuation obtained by the TP-probe is approximately 1.7 times larger than that of the SP-probe. Figure 4.22 shows the distributions of the skewness of fluctuating static pressure. The results given by the TP-probe take significantly larger values compared to the SP-probe case. The negative value of the skewness observed throughout the mixing layer coincides with the observation in other simple flows such as the turbulent jet (Tsuji and Ishihara, 2003) and the turbulent channel flow (Kim, 1989). In Fig. 4.23, the velocity-pressure correlation shows reasonable agreement between two different methods, especially at the downstream locations $x = 100$ mm and 150 mm. The TP-probe provides consistently larger values than the SP-probe in the developing region, which is considered to be a favorable consequence of the improvement in the spatial resolution.

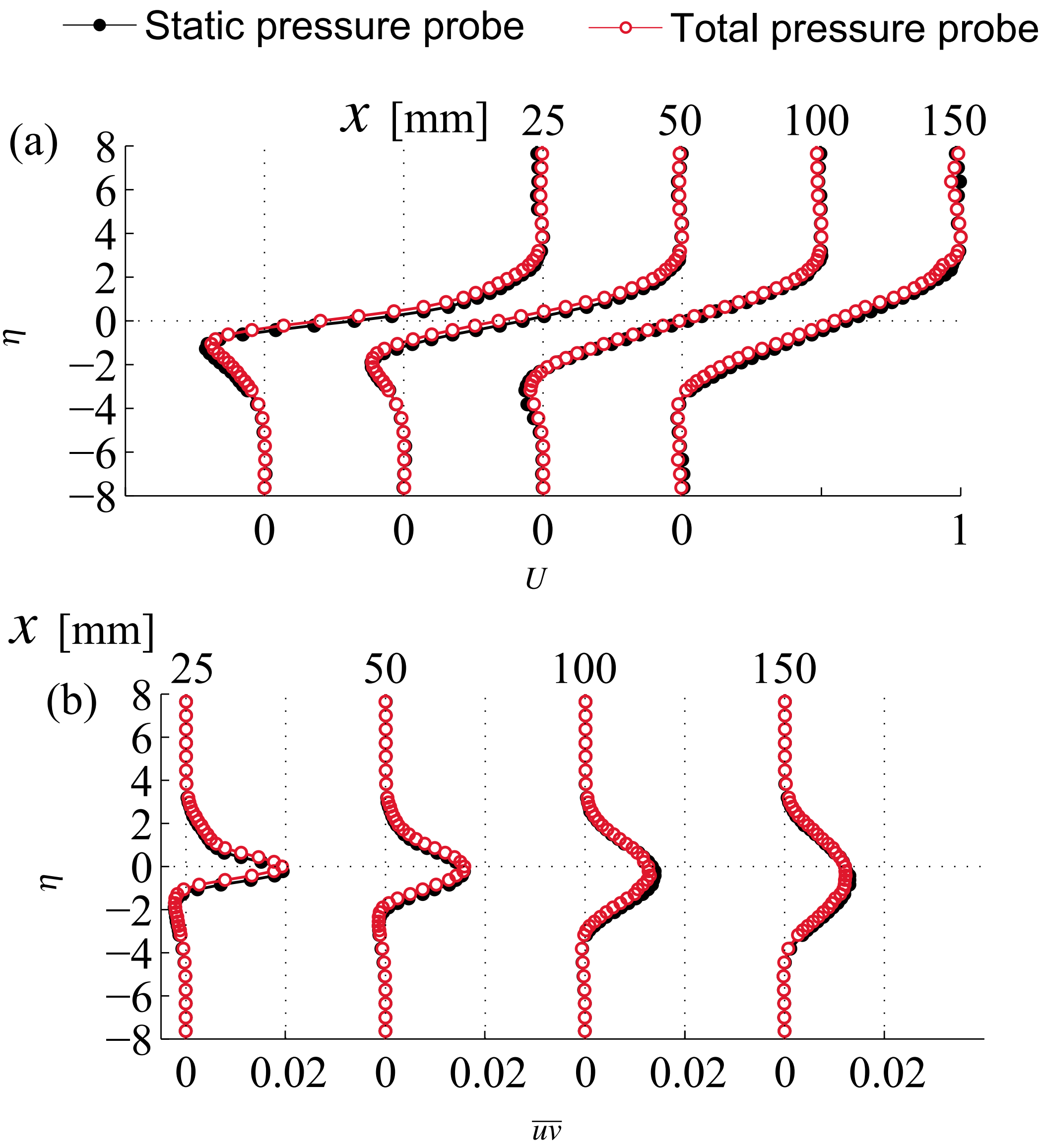

Figure 4.20: Profiles of (a) streamwise mean velocity $\overline{U}$ and (b) Reynolds shear stress $-\overline{uv}$.

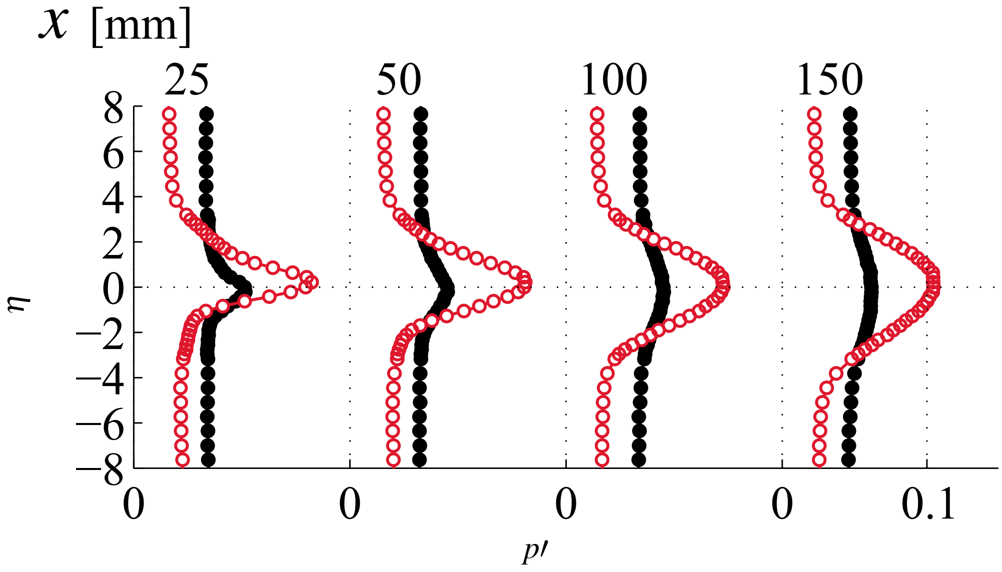

Figure 4.21: Profiles of static pressure fluctuation p'.

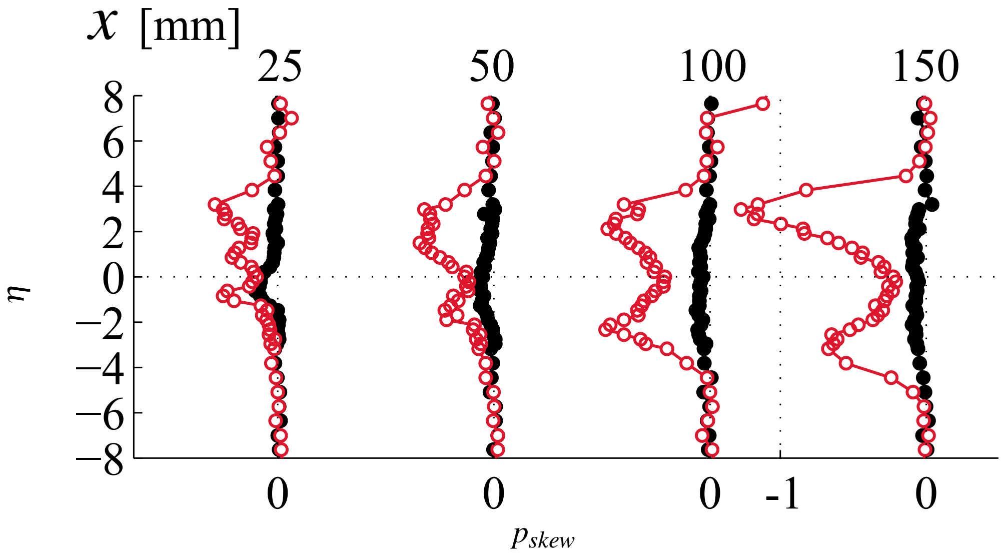

Figure 4.22: Profiles of the skewness of pressure fluctuation p_{skew}.

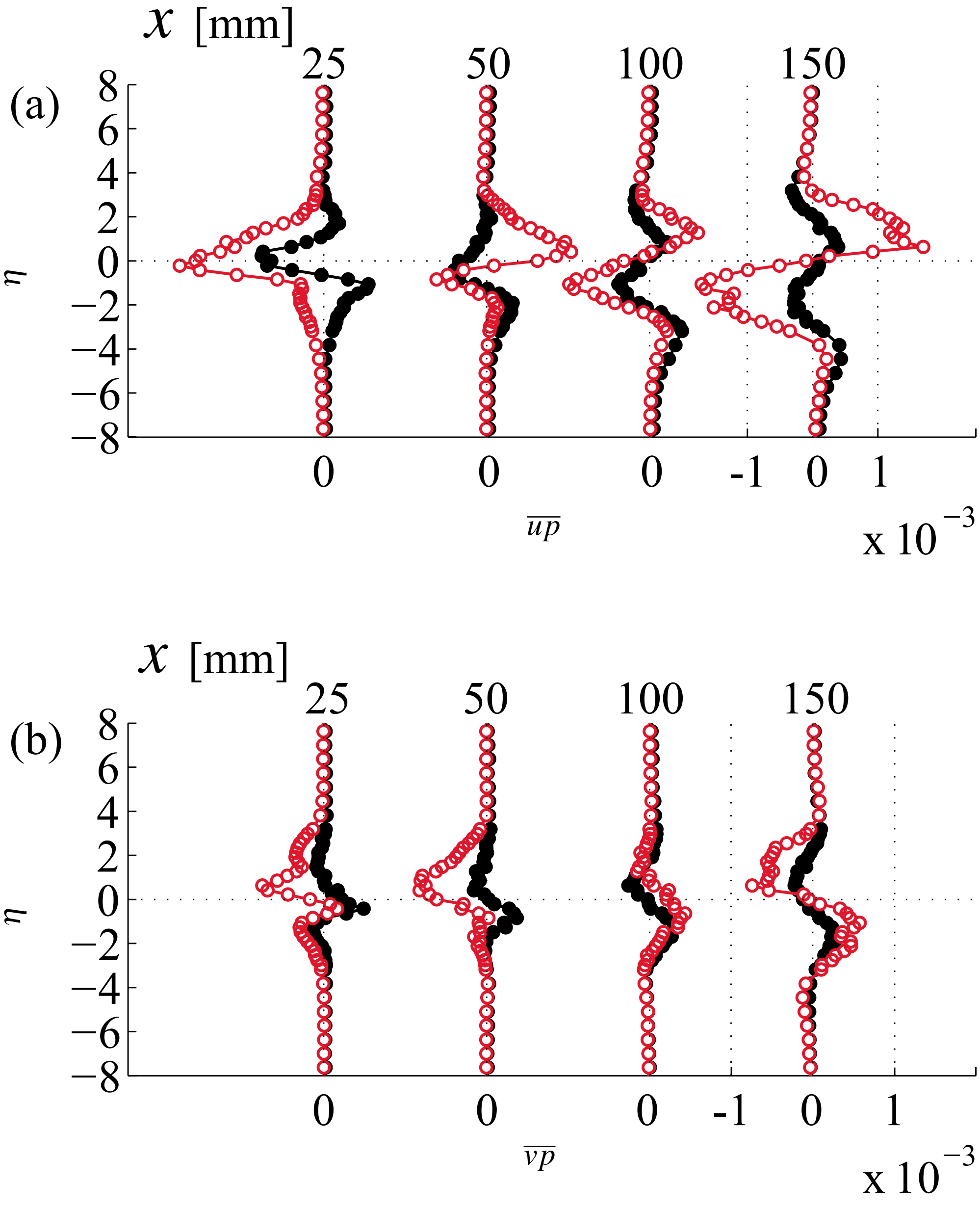

Figure 4.23: Profiles of velocity-pressure correlation; (a) $\overline{up}$, (b) $\overline{vp}$.

4.5.4 Discussion

The distributions of static pressure fluctuation obtained by the TP-probe show significantly larger than those measured by the SP-probe (cf. Fig. 4.21). The pressure fluctuation normalized by the local streamwise velocity fluctuation $p'/(\rho u'^2)$ are presented in Fig. 4.24. The profiles take minima near the center of the mixing layer approximately 1.7 and 3.0 for the data obtained by the SP- and TP-probes, respectively. These minima are not much affected by the streamwise locations.

In previous studies, Batchelor (1951) and Hinze (1975) theoretically gave 0.58 and 0.7 for the value of $p'/(\rho u'^2)$ under the assumption of idealized conditions. Tsuji et al. (2007) noted that some DNS results of isotropic turbulence suggest that the value of $p'/(\rho u'^2)$ takes from 0.8 to 1.0 for $Re_\lambda \leq 300$. Tsuji and Ishihara (2003) and Tsuji and Ishihara (2006) evaluated $p'/(\rho u'^2)$ to be approximately 0.7 for low Reynolds numbers from their experimental data at the centerline of the jet, where the turbulence becomes nearly isotropic. On the other hand, Tsuji et al. (2007) reported that $p'/(\rho u'^2)$ significantly varies across the turbulent boundary layer. It takes approximately 1.0 near the wall, and it rapidly increases to 5 in the wake region. It might depart from unity due to the existence of apparent vortical structures in the outer layer. Since no data is available for comparison in the mixing layer, it is difficult to facilitate a quantitative evaluation for the data obtained in the present study. At least we can say that the values obtained here by both the SP- and TP- are the order of unity.

The combined standard uncertainty of the static pressure calculated from Eq. (3.6) is estimated. The combined standard uncertainty ζ_c is:

$$\zeta_c = \sum_{i=1}^{N} \left[\frac{\partial f_p}{\partial q_i} \right]^2 \zeta^2(q_i), \tag{4.15}$$

where ζ is standard uncertainty of the target property, f_p is a function to estimate the property and q_i indicate the arbitrary quantity. The detailed procedure to calculate ζ_c is described in Appendix B. The ζ_c is estimated at the center of the mixing layer at $x =$ 150 mm; $\zeta_c/(\rho(\Delta U)^2) = 5.6\times10^{-3}$, which corresponds to 9.3% of the value measured by the SP-probe. The value is mostly originated from the uncertainty on the statistical estimation of the total pressure fluctuation and streamwise mean velocity because they are significantly greater than the static pressure fluctuation in magnitude.

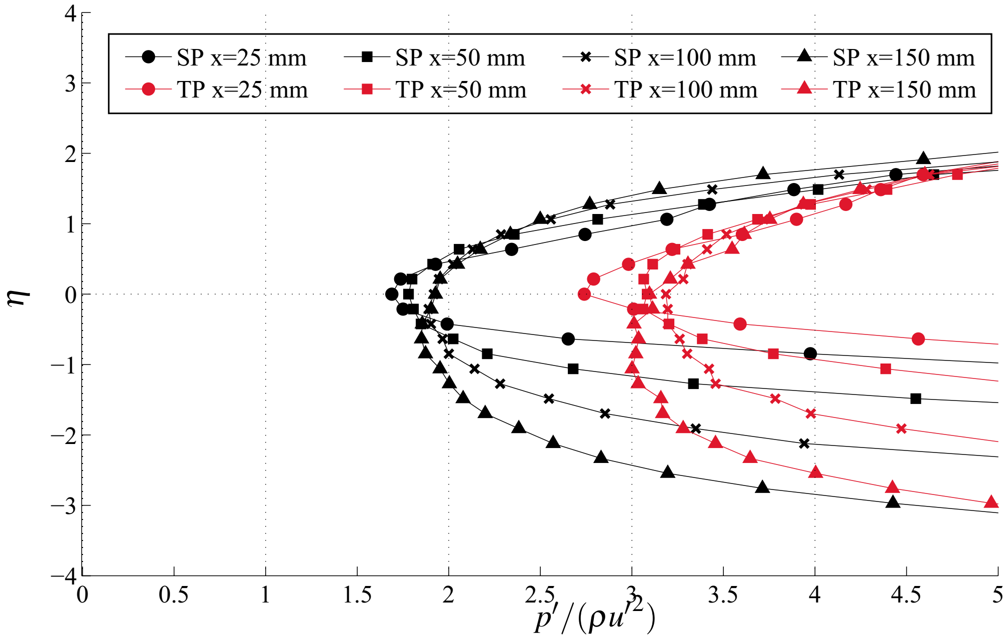

Figure 4.24: Profiles of $p'/(\rho u'^2)$.

4.5.5 Summary

The simultaneous measurements of fluctuating velocity and pressure have been performed in the turbulent mixing layer. The X-probe is combined with either the SP- or the TP-probe designed for pressure measurements. The velocity-pressure correlations measured by the two methods agree fairly well as the flow approaches the self-similar state. The TP-probe provides consistently larger value than that of the SP-probe in the developing region, which is considered as favorable consequence of the improvement in spatial resolution.

Chapter 5

Measurements in a wing-tip vortex

5.1 Measurements in three different streamwise locations

5.1.1 Motivation

The swirling motion of the wing-tip vortex creates a significant pressure distribution and velocity gradients, and as a consequence, it is expected that the strong velocity and pressure fluctuations take place. In addition, the meandering of the wing-tip vortex causes the extra velocity and pressure fluctuations. We consider therefore the wing-tip vortex may serve as a good test case for the investigation on the relationship between the large-scale vortical structure and the contribution of the velocity-pressure correlation in the balance of turbulence characteristics, e.g. the turbulent kinetic energy and the Reynolds stress.

The meandering of the wing-tip vortex was experimentally observed in the past and several different possible reasons were proposed to account for its origin. Devenport et al. (1996) concluded that the meandering was caused by wind-tunnel unsteadiness. Studies performed by Bailey and Tavoularis (2008) suggested that the higher free stream turbulence levels introduces the larger amplitude of the meandering. Heyes et al. (2004) indicated that meandering is entirely responsible for the distribution of the Reynolds stress.

In order to evaluate the velocity-pressure correlation, simultaneous measurements

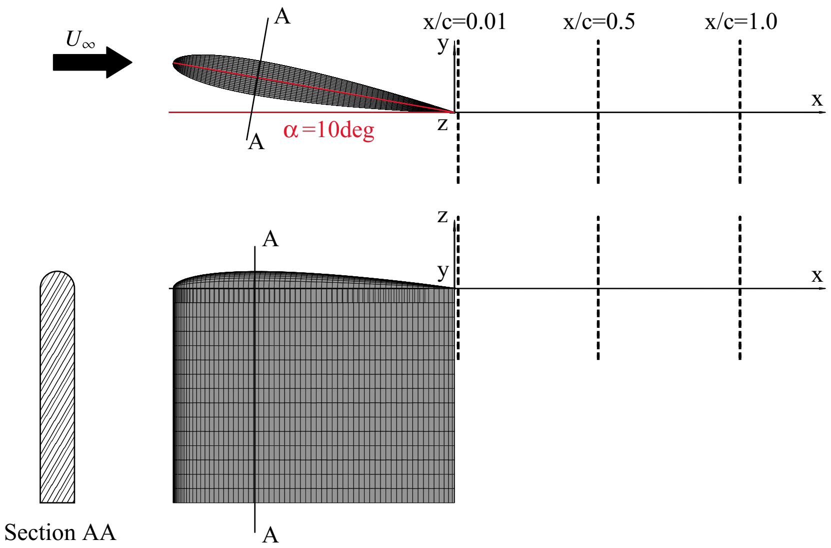

Figure 5.1: Schematic of the experimental configurations.

of fluctuating velocity and pressure at arbitrary locations are necessary. Although the measurement of the fluctuating pressure has been a challenging problem, the local measurement of fluctuating static pressure using the miniature pressure probe developed by Toyoda et al. (1994) becomes popular according to several successful reports Tsuji et al. (2007); Tsuji and Ishihara (2003). We also have confirmed the applicability of the technique of the simultaneous measurement of fluctuating velocity and pressure with the combination of this probe and the X-type hotwire probe in a plane turbulent mixing layer.

Here, simultaneous measurements of fluctuating velocity and pressure are performed in the near-field of the wing-tip vortex where the vortex is under the development. Through the developing region of the wing-tip vortex, the contribution of a large longitudinal vortex on the distributions of the pressure fluctuation and the velocity-pressure correlation are investigated.

5.1.2 Experiments

Experiments were performed in a blowing wind-tunnel with a 0.35 m × 0.35 m cross section. The free stream velocity was 9.3 m/s and the free stream turbulence level was approximately 0.6%. A NACA 0012 half-wing model with semi-span $b/2$ and chord

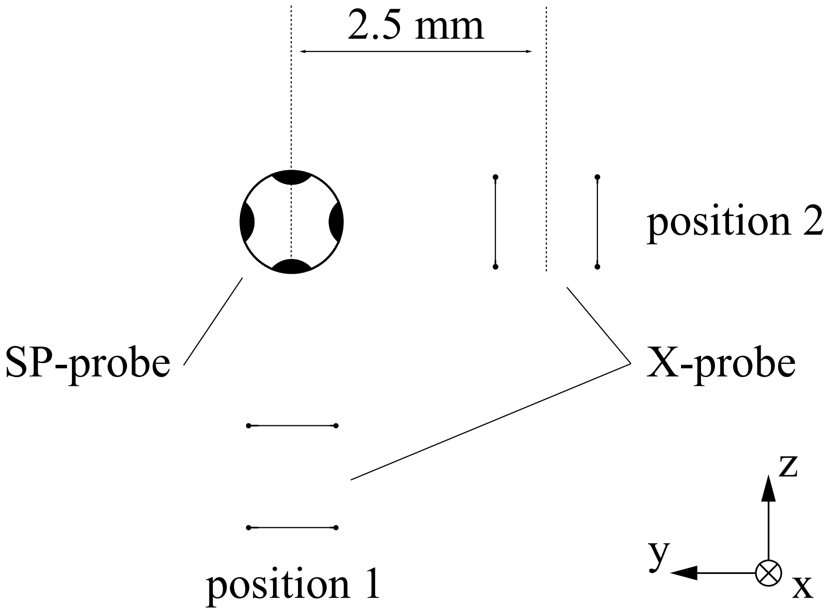

Figure 5.2: Arrangements of the X- and SP-probes; position 1 u, v and p, position 2 u, w and p.

c of lengths 150 mm and 200 mm respectively, was mounted immediately behind the nozzle exit at an angle of 10° against the free stream direction. The Reynolds number of $Re_c = 1.24 \times 10^5$ was given based on the chord length c and the free stream velocity U_∞. The end of the wing was rounded in the shape of a half circle with a radius varying according to the local thickness of the wing. The Cartesian coordinates were defined with respect to the trailing edge of the wing, with x-, y- and z-axes taken in the streamwise, transverse and spanwise directions.

Simultaneous measurements of fluctuating static pressure and velocity were performed using an X-probe (Dantec 55P64) and SP-probe. In order to achieve the simultaneous measurement of velocity and pressure, these two probes were placed parallel to the free stream direction as shown in Fig. 5.1. Two different probe positions as illustrated in Fig. 5.2 were employed so that three mean velocity and five Reynolds stress components could be obtained by the X-probe. The center-to-center distance between the SP- and X-probes was set to 2.5 mm. The streamwise velocity component u could be measured in both positions, hence the mean velocity U and the rms value of velocity fluctuation u' were calculated as an average of the results obtained by the two probe

Table 5.1: Measurement conditions.

Probe setting	x/c	Δy, Δz [mm]
X-probe	0.01	1.5
	0.5	3.0
	1.0	3.0
triple-probe	0.01	1.5
	0.5	1.2
	1.0	1.2
X-HWP & SP-probe	0.1	1.5
	0.5	1.2
	1.0	1.2
X-HWP & SP-probe	1.0	1.2

positions.

Measurements were undertaken in different combinations of probe configurations and streamwise locations summarized in Table 5.1. The combined probe was traversed in both the y- and z-directions over the region consisting of 24 mm × 24 mm with increments of 1.2 mm in each direction providing 441 measurement points. The traversing systems in y and z directions were controlled by a PC with a resolution of ± 10 μm while the position in x direction was adjusted by hand. The sampling rate was 10 kHz and the sampling time was 30 s at each point.

The effective angle technique Browne et al. (1989) was used for converting the signal from the CTA into velocity. The yaw-angle calibration was carried out in order to determine the effective angle. Since the X-probe was applied to three dimensional flows such as the wing-tip vortex, we performed the calibration to check the apparent increase of velocity due to the pitch angle (defined by the angle between the velocity vector and the X-probe plane). The velocity measured in the wing-tip vortex was corrected according to the pitch angle which was obtained by the time-averaged axial and tangential velocity components.

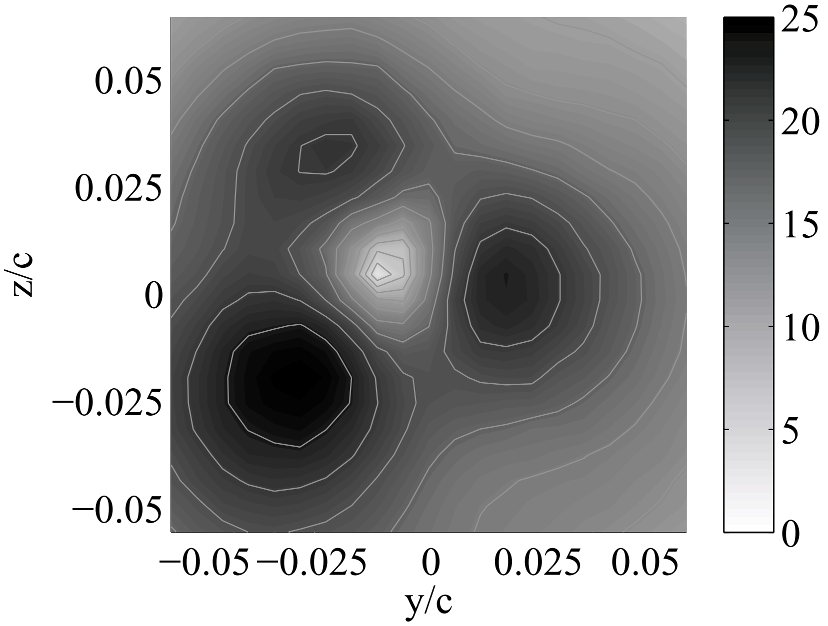

Figure 5.3: Angle of velocity vector against *x*–axis.

5.1.3 The effect of flow angle attack

The measurement uncertainty caused by the yaw-angle response of the SP-probe is estimated. Figure 5.3 shows the contour of the angle of velocity vector against the streamwise axis computed from the time-averaged three velocity components. The time-averaged flow angle indicates roughly 20°–25° in the outer region of the vortex. Based on the yaw-angle response of the SP-probe (see section 3.1.1), the error caused by this inclination of time-averaged flow can be estimated to be approximately 7%–11%. As for the TP-probe, it rises up to approximately 4%.

5.1.4 Results

5.1.4.1 Characteristics of the wing-tip vortex

Figure 5.4 presents the perspective view of the mean velocity. The contour indicates the magnitude of the streamwise mean velocity and the transverse velocity components are presented by arrows. Significant velocity deficit is observed the just behind of the wing, and the wake gradually disappears in downstream locations.

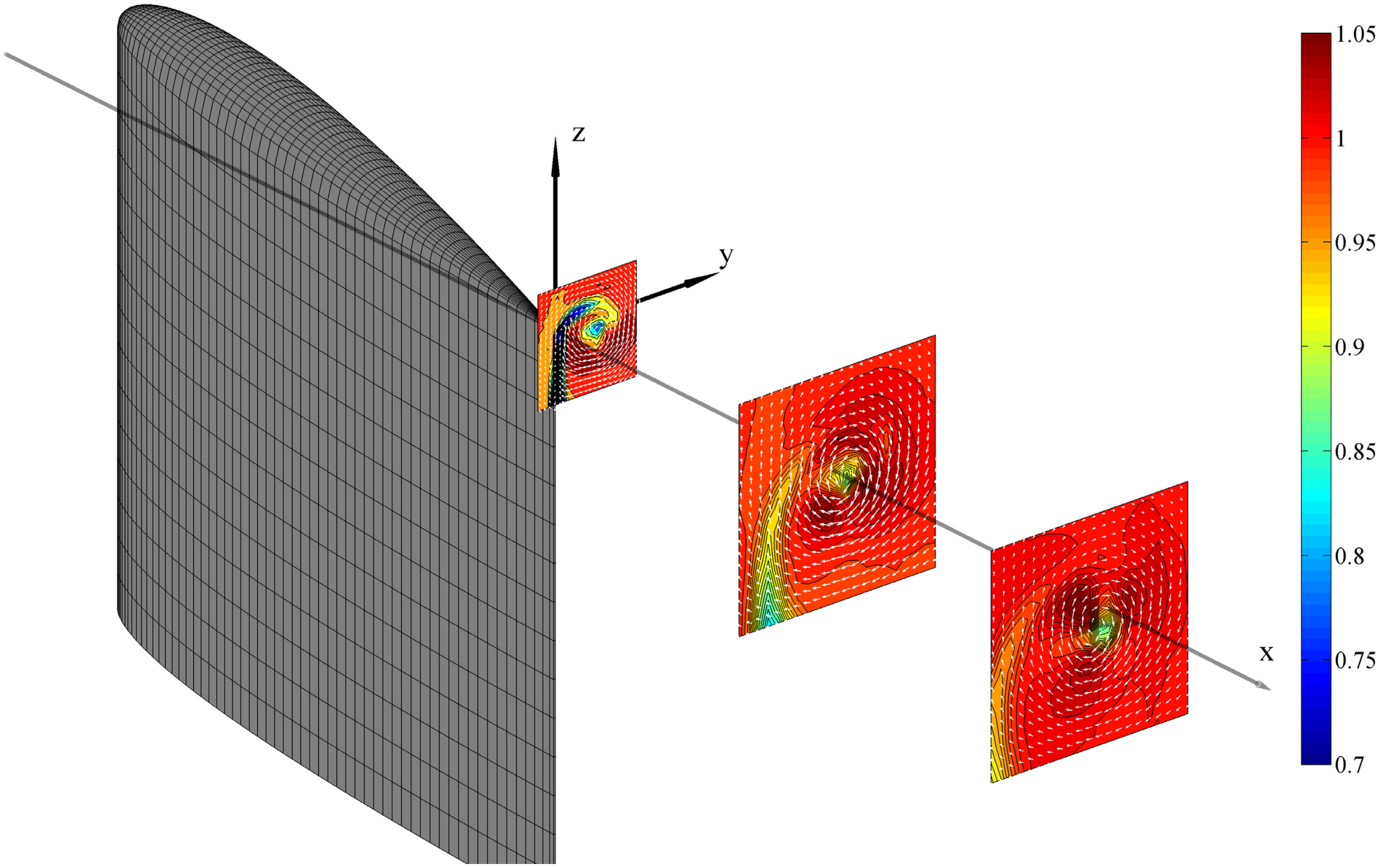

Figure 5.4: Perspective view of mean velocity.

The velocity distribution inside the vortex shows the deficit, which is approximately 25% of the free stream velocity. Perspective views of other statistics, e.g. Reynolds stresses, the fluctuating pressure, the PDF of zero-crossing samples, are presented in Appendix C.

Figure 5.5 shows the distributions of axial and circumferential velocity components U, V and streamwise vorticity Ω_x across the vortex. The origin of the coordinate z is adjusted to the center of the primary vortex (y_c, z_c), defined as the location where the magnitude of time-averaged circumferential velocity $\sqrt{V^2+W^2}$ reaches a minimum. The variables are normalized by the free stream velocity U_∞ and the chord length c.

As shown in Fig. 5.5(a), the profiles of the axial velocity at three different streamwise positions exhibit wake-like profiles. The profile at $x/c = 0.01$ indicates a 25% velocity deficit against the free stream velocity, recovering to 15% at $x/c = 0.5$. In addition, two local minima are found at $x/c = 0.01$. The minimum near $(z-z_c)/c = 0.03$ is due to the shear layer rounding up from the pressure side of the wing. The time-averaged circumferential velocity reaches about 55% of free stream velocity at $x/c = 0.01$ as shown in Fig. 5.5(b).

Figure 5.5(c) shows the profiles of the streamwise vorticity Ω_x. The magnitude at the vortex center decreases in the downstream direction. At $x/c = 1.0$, the peak value is reduced to nearly a half of that at $x/c = 0.01$. The decrease of the magnitude of vorticity indicates that the wing-tip vortex is weaker downstream. As indicated in Anderson and Lawton (2003), the circulation parameter $\Gamma/U_\infty b$ is proportional to the axial velocity at the core of the vortex. In the present case, the circulation parameter $\Gamma/U_\infty b = 0.052$, corresponds to the case of deceleration in Anderson and Lawton (2003).

5.1.4.2 Meandering of the vortex

According to previous experimental observations, e.g. Chow et al. (1997), the time-averaged vortex center moves downstream as it develops due to something known as the "vortex kink" which can happen even in the near field. Figure 5.6 presents the positions of the vortex center and their radii at three streamwise locations. The radius of the vortex is given as a half of the distance between the positions where the time-averaged circumferential velocity distribution takes maximum and minimum. The radius of the

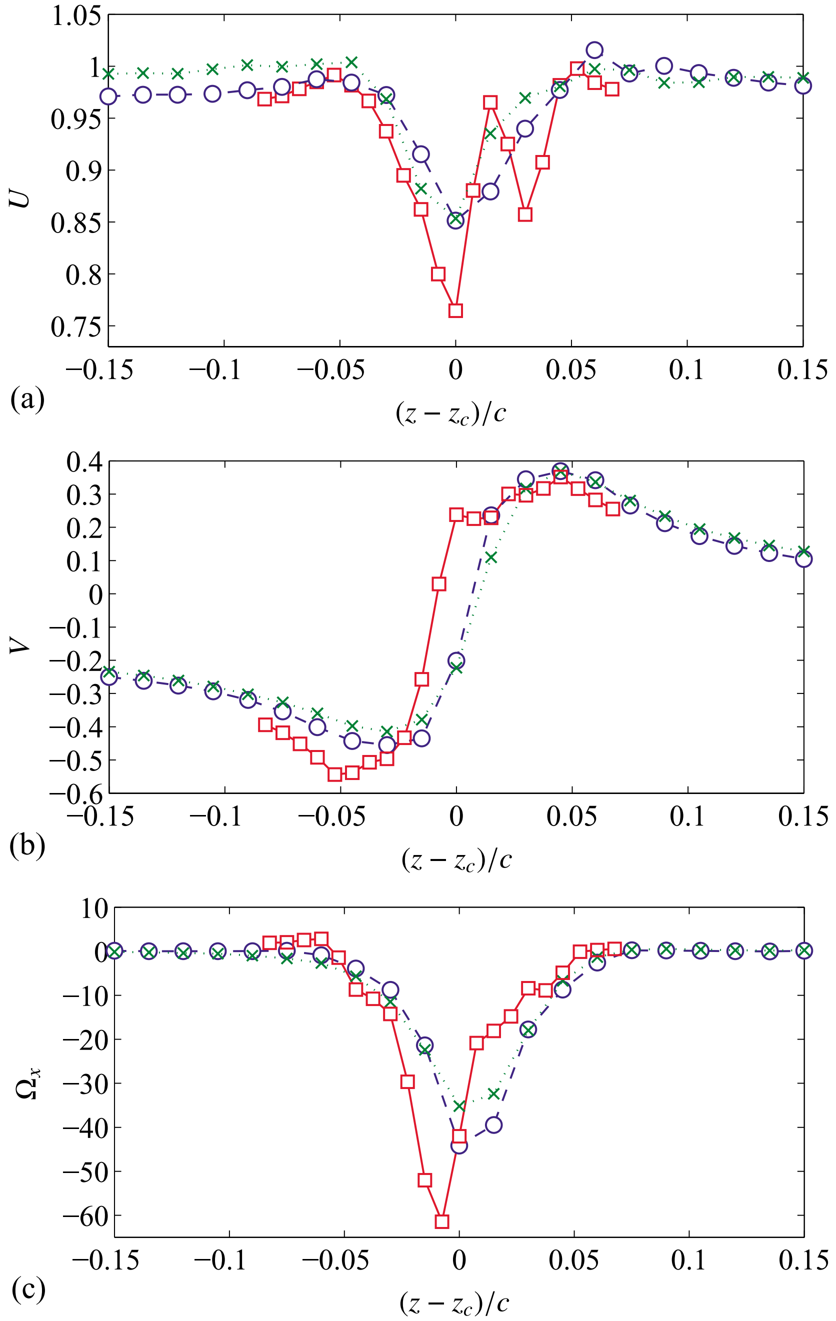

Figure 5.5: Line-plots in z direction through the vortex center; (a) U, (b) V and (c) Ω_x. □: $x/c = 0.05$, ○: $x/c = 0.5$, ×: $x/c = 1.0$.

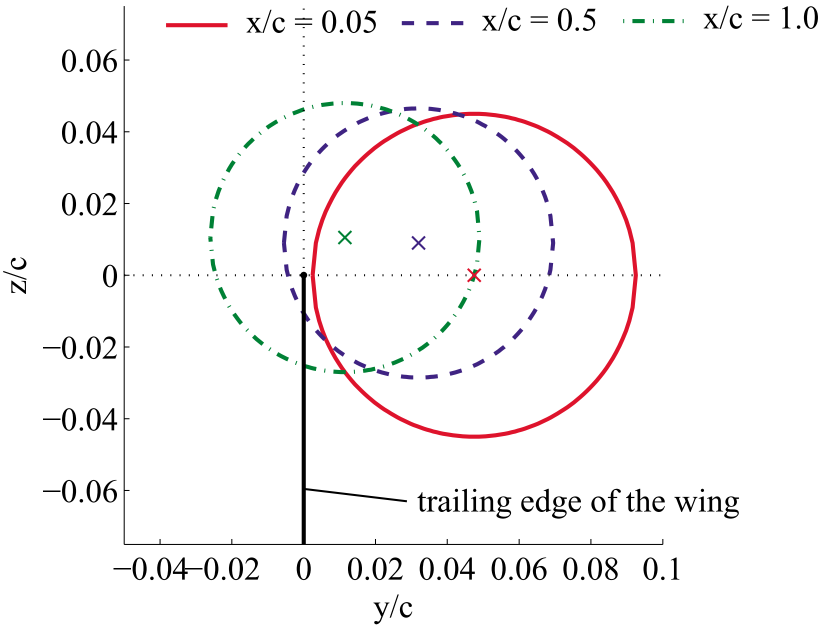

Figure 5.6: Positions of the vortex center and its radius.

main vortex becomes slightly smaller and its center moves closer to the trailing edge in y direction and slightly outward in z direction.

Figure 5.7 shows the streamwise development of the rms value of velocity fluctuations u', v', w' at the vortex center. The transverse components v' and w' increase remarkably with x/c. Figure 5.8 shows the PSD of fluctuating velocity component v measured at the vortex center. The PSD in lower frequency range increases in the downstream region. The peak near 650 Hz found at $x/c = 0.01$ disappears in downstream locations $x/c = 0.5$ and 1.0. This peak at relatively higher frequency is caused by the wake of the thin-trailing edge of the wing. The perturbation in high-frequency decays quickly and does not penetrate into the center of the wing-tip vortex at downstream locations. Figure 5.9(a) shows the contour of static pressure fluctuation normalized by $\rho {U_\infty}^2/2$. In the distribution of $\overline{p^2}$, two local peaks are found slightly off the vortex center. In Fig. 5.9(b), $\overline{p^2}$ is plotted in z direction. As it moves to downstream, the two peaks become distinct and the distance between them increases.

The observations noted above indicate that the meandering of the vortex grows in the downstream direction. The increase of transverse velocity fluctuation v' and the two peaks in the distribution of $\overline{p^2}$ can be attributed to the unsteady vortex motion in

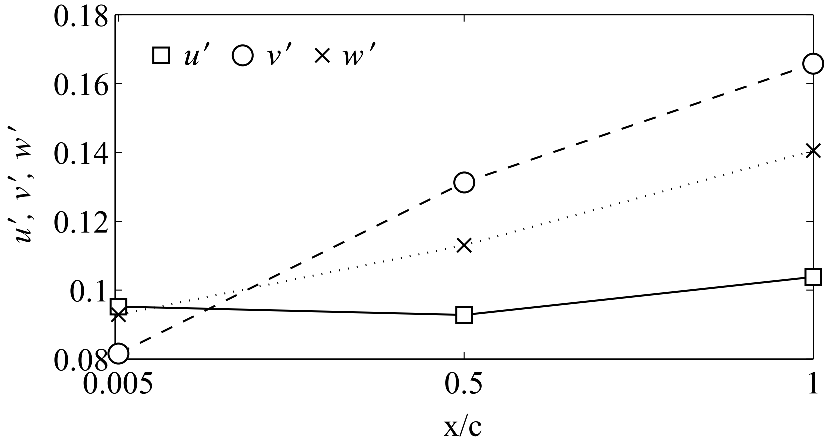

Figure 5.7: Variation of velocity fluctuations; u', v' and w'.

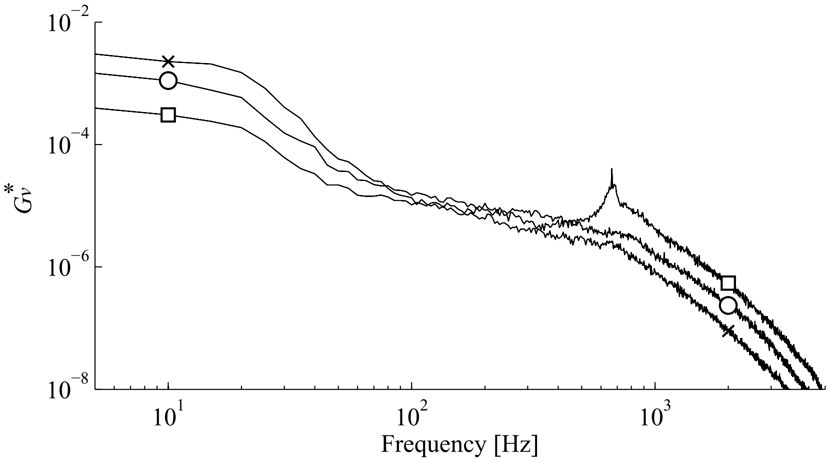

Figure 5.8: PSD of transverse velocity v at the vortex center (same symbols notation as Fig. 5.5).

the direction of wing-span z. The profiles of PSD at three different locations indicate that the vortex meandering takes place in a frequency range lower than 100 Hz.

5.1.4.3 Velocity-pressure correlation

In Fig. 5.10(a) and 5.10(b), $\overline{up}$ and $\overline{vp}$ measured by the probe position 1 (illustrated in Fig. 5.2) are plotted along a line in the z direction through the vortex center, and in Fig. 5.10(c) and (d), $\overline{up}$ and $\overline{wp}$ measured by the probe position 2 are plotted in y direction.

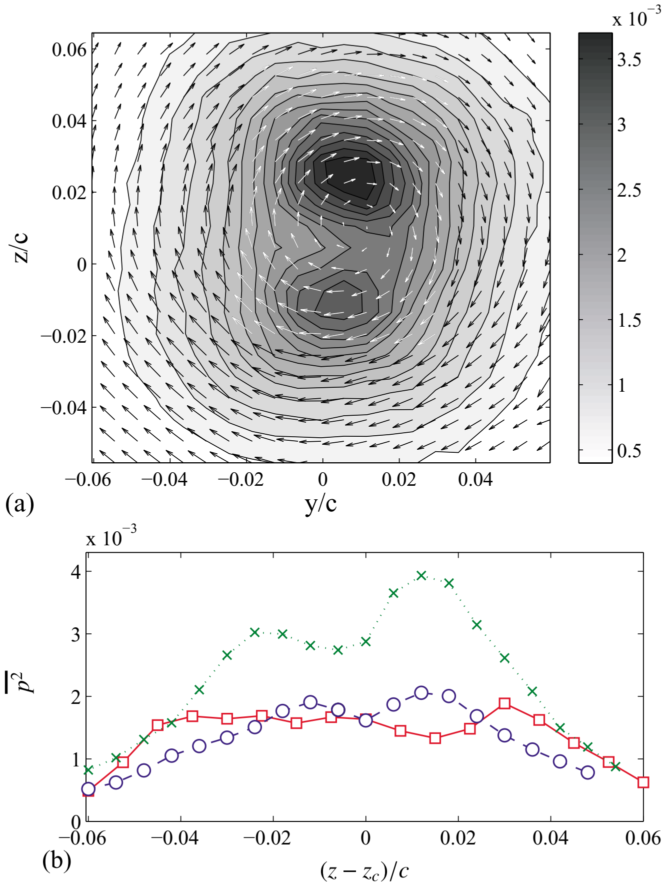

Figure 5.9: Distributions of the pressure fluctuation; (a) contour plot at $x/c = 1.0$, (b) line plots in z direction (same symbols notation as Fig. 5.5).

The peaks of $\overline{up}$, $\overline{vp}$ and $\overline{wp}$ increase with streamwise location, and their positions in the y and z directions relative to the vortex center are nearly constant. The increase in the velocity-pressure correlation can be attributed to the meandering of the vortex similar to the increase of the velocity and pressure fluctuation shown in Figs. 5.7 and 5.9. Although the significant variation of the velocity-pressure correlation might indicate a contribution from the pressure-diffusion terms to the balance of turbulence properties, it should be further investigated by the comparison with other terms.

To facilitate a discussion on the velocity-pressure interaction, the correlation coefficient is now examined. Figure 5.11 shows the correlation coefficient of fluctuating velocity and pressure (R_{up} and R_{vp}) across the vortex. Distributions at $x/c = 0.5$ and 1 agree well with each other, indicating that the flow tends to develop into a self-similar

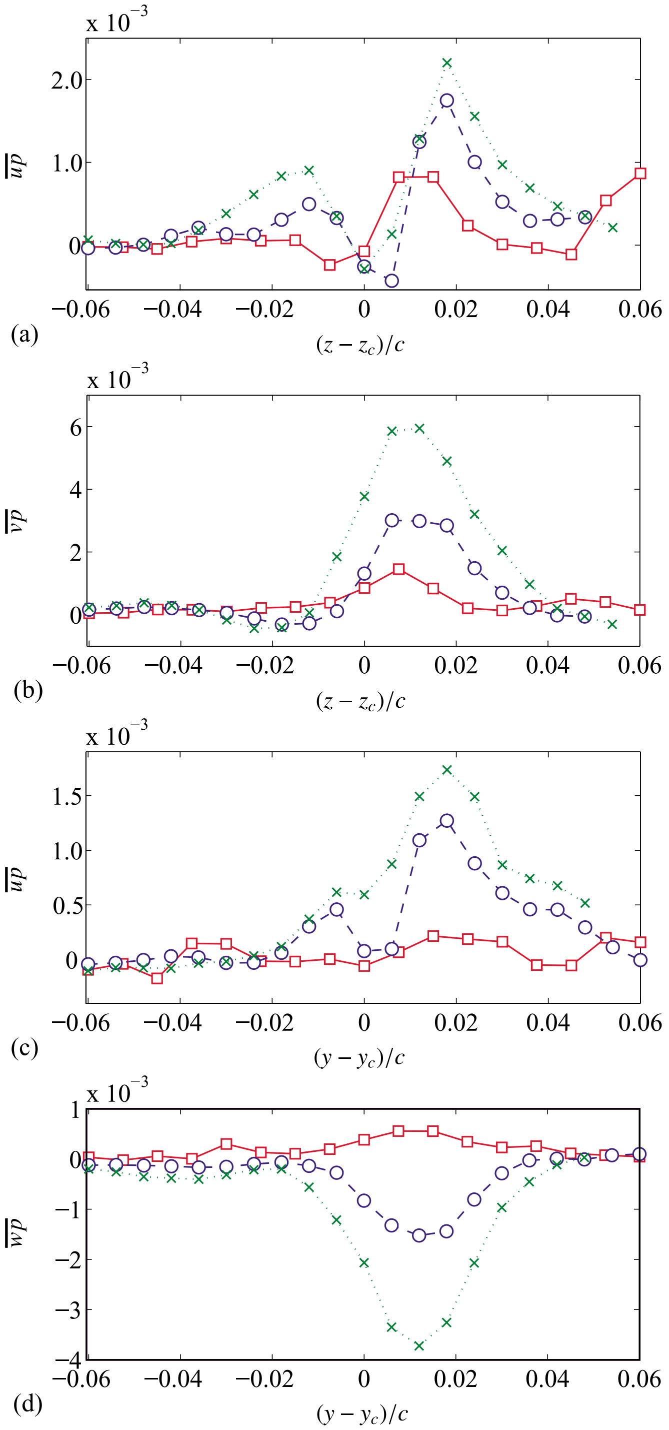

Figure 5.10: Profiles of velocity-pressure correlation thorough the vortex center; (a) $\overline{up}$, (b) $\overline{vp}$, (c) $\overline{up}$, (d) $\overline{wp}$ (same symbols notation as Fig. 5.5).

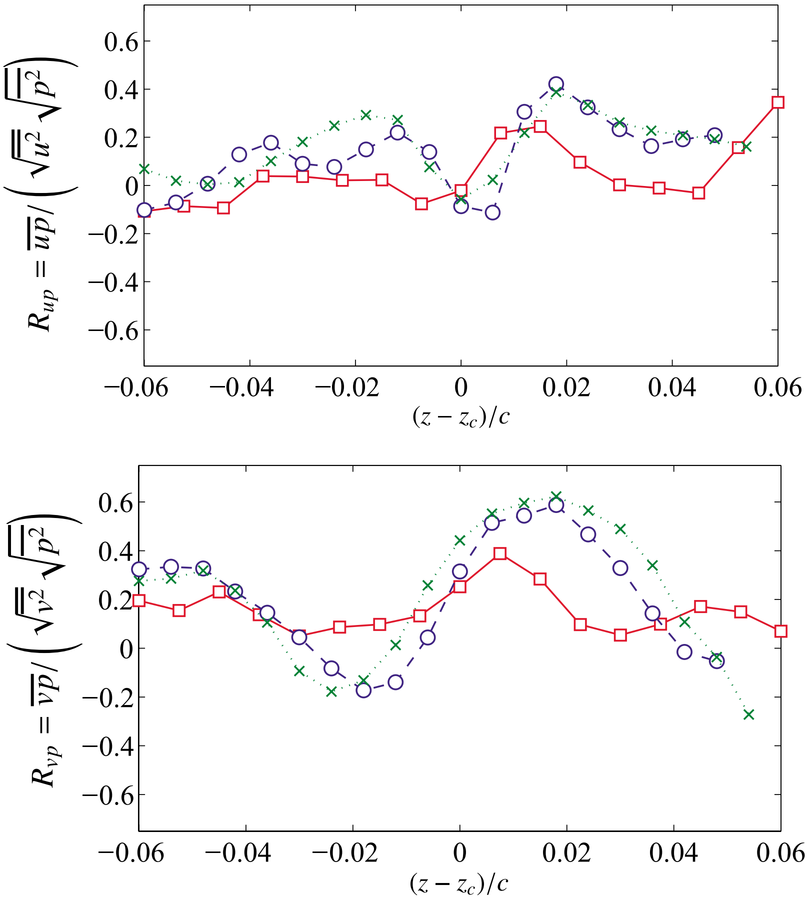

Figure 5.11: Profiles of the correlation coefficient of velocity and pressure thorough the vortex center; (a) $\overline{up}$, (b) $\overline{vp}$ (same symbols notation as Fig. 5.9).

state. R_{up} has two positive peaks and the correlation rises up to 0.4, while R_{vp} has negative and positive peaks near the vortex center and the correlation reaches 0.6. These profiles of correlation coefficients may be related to the unsteady motion of the wing-tip vortex in z direction as indicated in the $\overline{p^2}$ distribution, shown in Fig. 5.9(a), which is elongated in the z-direction.

5.1.5 Summary

Simultaneous measurements of fluctuating velocity and pressure were conducted in the wing-tip vortex trailing from a NACA 0012 wing.

The present experimental observations indicate that the meandering of the vortex grows in the downstream direction and that the transverse velocity fluctuation increases in the vortex core. The peaks of pressure fluctuation appear slightly off center in the vortex and become clear further downstream. The PSD of transverse velocity fluctuation indicates that the vortex meandering occurs in the frequency range lower than 100 Hz.

The profiles of the velocity-pressure correlation $\overline{up}$, $\overline{vp}$ and $\overline{wp}$ show distinct peaks near the vortex center. The significant gradient of the velocity-pressure correlation can be attributed to a contribution of the velocity-pressure correlation to the balance of turbulence properties.

5.2 Application of TP-probe in a wing-tip vortex

5.2.1 Motivation

In the previous chapter, the combination of the TP- and X-probes has validated in a turbulent mixing layer, and the results of two methods agree well each other. Here, the TP-probe is applied to a wing-tip vortex. The wing-tip vortex provides a challenge because of its three-dimensional nature and strong pressure fluctuations due to the development of a streamwise vortex.

5.2.2 Experimental conditions

The same blowing wind tunnel and the configurations of the NACA 0012 half-wing as previous Section 5.1.2 were used. The measurements were undertaken at one streamwise position $x/c = 1.0$, and the combined probe was traversed in both the y- and z-directions for the range of -12.1 mm $\leq y \leq$ 11.9 mm, -11.1 mm $\leq z \leq$ 12.9 mm with an increment of 1.2 mm in each direction, providing 441 measuring points.

Similarly with the case of the combination of the SP- and X-probe, the measurements provided by the TP- and X-probes were performed in two different configurations, as illustrated in Fig. 5.12, in order to measure three components of the mean velocity and five components of the Reynolds stress. The configuration of Fig. 5.12(a)

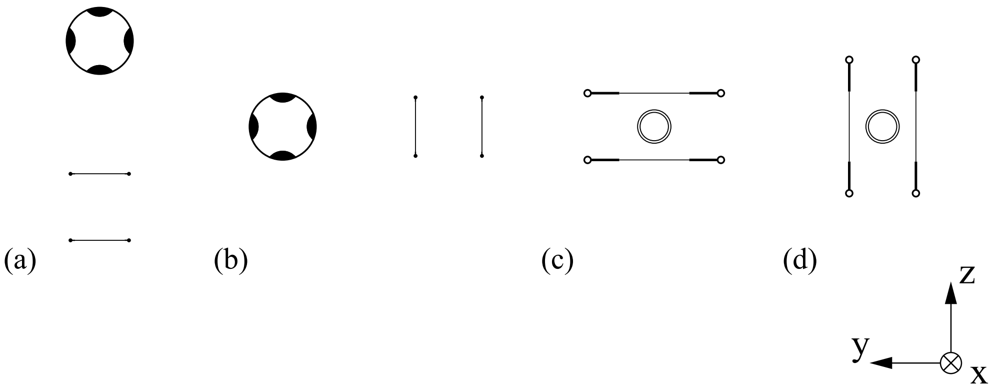

Figure 5.12: Configurations of the SP- and X-probes (a) for u, v, and p measurement; (b) for u, w, and p measurement. Configurations of the TP- and X-probes (c) for u, v, and p_t measurement; (d) for u, w, and p_t measurement.

was used for the simultaneous measurement of u, v and p_t, while that in (b) was employed for u, w and p_t measurement. The results obtained by the SP- and X-probes are employed for the comparison.

The signals from the CTA and the condenser microphone were acquired at a 10 kHz sampling rate after low-pass filtered at 5 kHz by an analogue filter circuit. The sampling time at each location was 30 s.

5.2.3 Results

Figure 5.13 shows the streamwise velocity fluctuation u' measured by various combinations of the probes and their configurations. (a) and (b) indicate the results by the SP- and X-probes combination, and (c) and (d) by the TP- and X-probes. These symbols correspond to those of probe arrangements indicated in Fig. 5.12 and (e) shows the results by the triple-probe. The values are normalized by U_∞. The distributions of u' in Fig. 5.13(a) and (b) show broad shapes but are skewed in either the y- or z-direction according to the configuration of the probes. This is most likely due to the fact that the X-probe sensor is influenced by the wake of the SP-probe. In the case of the TP-probe, (c) and (d), the distributions are less skewed, being closer to those obtained by the triple-probe, (e). The slightly larger value obtained by the X-probe compared to the triple-probe may be caused by the velocity component that is out of the X-probe plane.

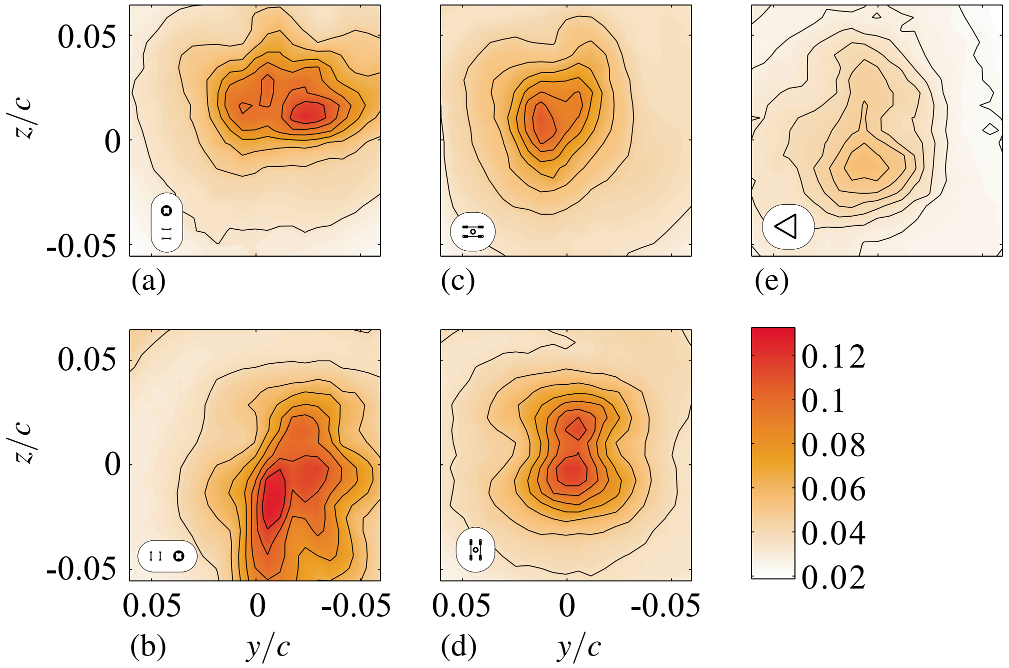

Figure 5.13: Streamwise velocity fluctuation u' measured by various combinations of the probes and their configurations. The arrangements of the probes are indicated bottom-left of each figure, cf. Fig. 5.12. The scales of these configurations are comparable to the size of the measurement domain.

Figure 5.14 shows the contour of the streamwise mean velocity component together with the cross-flow pattern indicated by vectors. It is noted that the streamwise mean velocity taken by the X-probe is calculated by averaging the values taken in two different configurations, cf. Fig. 5.12. In the result obtained by the SP- and X-probes, Fig. 5.14(a), the effect of the flow disturbance is clearly found in the skewed contour of the axial velocity. In contrast, the axial velocity distribution measured by the TP- and X-probes shown in Fig. 5.14(b) and that by the triple-probe in Fig. 5.14(c) indicate the wake-like profile which has the minimum value of about 0.75 U_∞, where the magnitude of the time-averaged circumferential velocity is close to zero. Here the magnitude of the time-averaged circumferential velocity reaches 0.41 U_∞ and the flow angle of attack to the probes reaches a maximum at approximately 25°. Based on the yaw-angle effect calibration shown in Fig. 3.3, the total pressure may be estimated by approximately 4%.

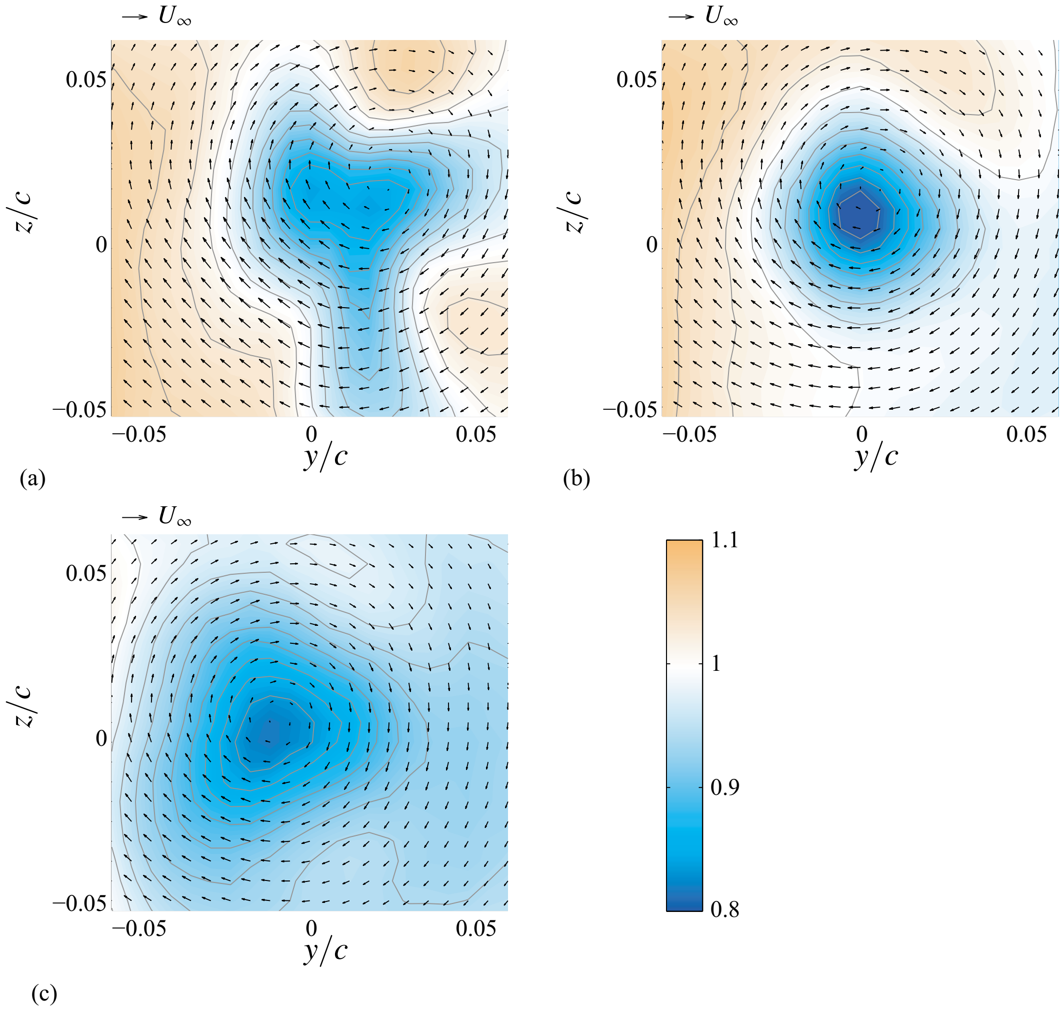

Figure 5.14: Contour plots of the streamwise mean velocity and vectors for the cross-flow mean velocity pattern; (a) the SP- and X-probes, (b) the TP- and X-probes, (c) the triple-probe.

Figure 5.15 shows the five Reynolds stress components measured by the combination of the TP- and X-probes. It is seen that the three normal stress components are concentrated near the center of the wing-tip vortex, while the two shear stress components are distributed across the flow. The corresponding results obtained by the triple-probe are presented in Fig. 5.16. The distributions of each Reynolds stress component are in good agreement with those shown in Fig. 5.15.

Among the three normal components of the Reynolds stresses measured by the

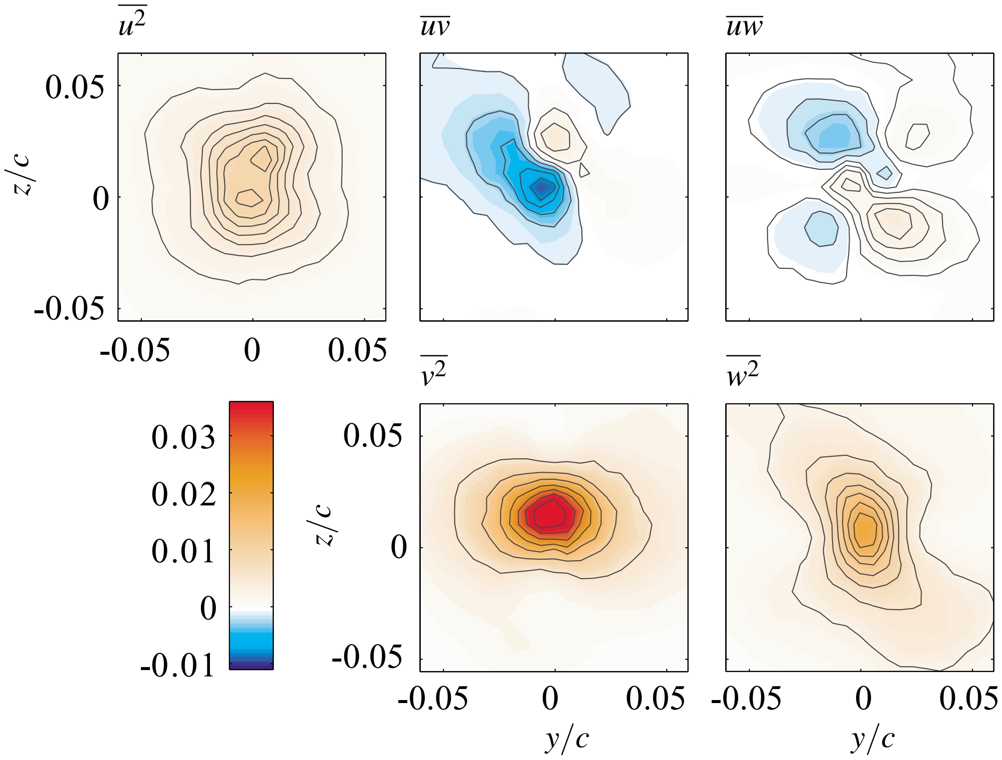

Figure 5.15: Reynolds stress components measured by the X- and TP-probes.

triple-probe presented in Fig. 5.16, transverse components $\overline{v^2}$ and $\overline{w^2}$, equal to 0.036 and 0.020, respectively, take significantly larger values than $\overline{u^2}$ which is only 0.0033. In addition, among the shear stress components, $\overline{vw}$ is substantially larger than $\overline{uv}$ and $\overline{uw}$. This strong anisotropy of the Reynolds stress is considered to be related to the large gradient of the tangential velocity across the primary vortex and its meandering.

Figure 5.17 shows the contours of the pressure fluctuation obtained by the SP- and TP-probes. Both distributions are elongated in the z direction and there are multiple maxima. On the other hand, measurements of the skewness of the pressure fluctuation (see Fig. 5.18) are slightly different - where the SP-probe indicates a positive value near the center of the primary vortex, the TP-probe does not.

The velocity-pressure correlations obtained by the two methods are compared in Fig. 5.19. The velocity-pressure correlations are normalized by $0.5\rho {U_\infty}^3$. The distribution of $\overline{up}$ is qualitatively different between the two methods, while the $\overline{vp}$ and $\overline{wp}$ appear to be insensitive to the difference in probes.

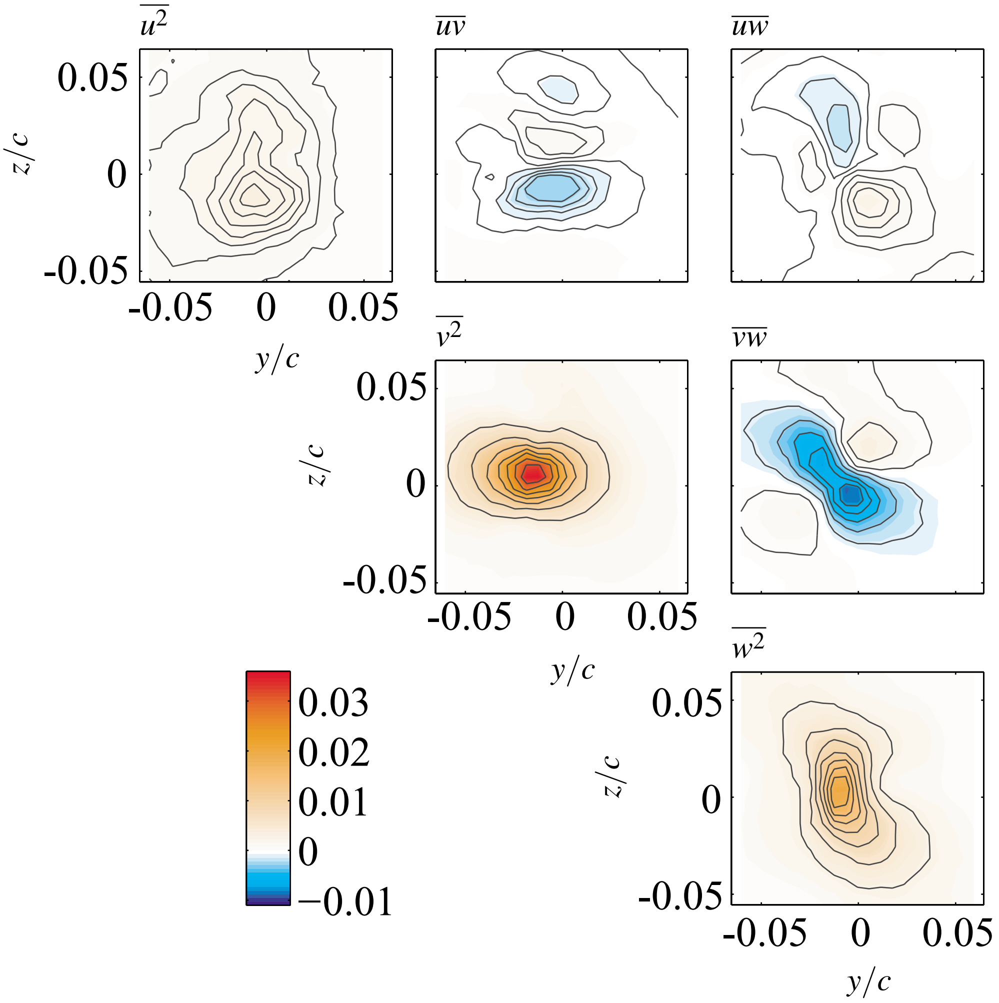

Figure 5.16: Reynolds stress components measured by the triple-probe.

This difference of $\overline{up}$ is caused by various reasons, though the major effect comes from the violation of the assumptions made for Eq. (3.6) or from the errors in instantaneous velocity measurement. It is demonstrated that the combination of the TP- and X-probes effectively avoids probe interference, though the effect of the velocity component out of the X-probe plane is remarkable and may contaminate the velocity

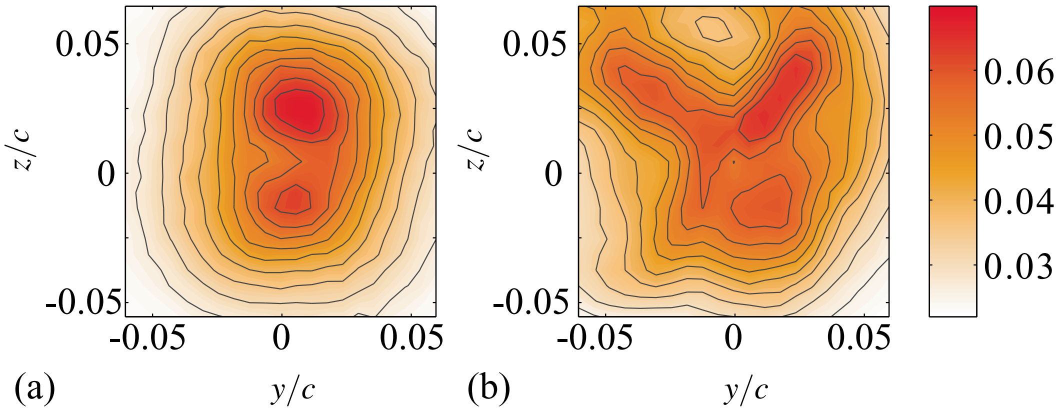

Figure 5.17: Pressure fluctuation p'; (a) the SP- and X-probes, (b) the TP- and X-probes.

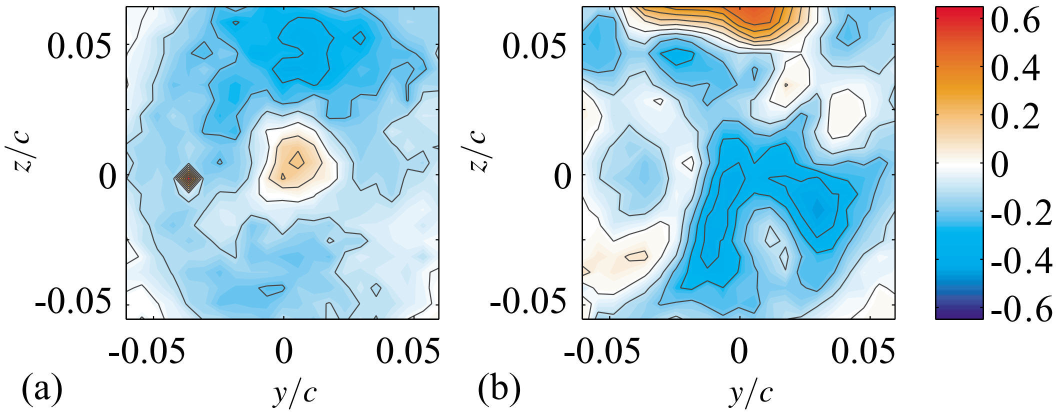

Figure 5.18: Skewness of pressure fluctuation p_{skew}; (a) the SP- and X-probes, (b) the TP- and X-probes.

measurement necessary for calculating the static pressure from the total pressure.

5.2.4 Discussion

Here, the meandering of the wing-tip vortex is identified by the zero-crossing technique proposed by Bailey and Tavoularis (2008). In the time-series for the signals of instantaneous cross-stream velocity $\hat{v}$ and $\hat{w}$ at one measurement point, both $\hat{v}$ and $\hat{w}$ can be close to zero at the same time the center of the vortex exists on the measurement

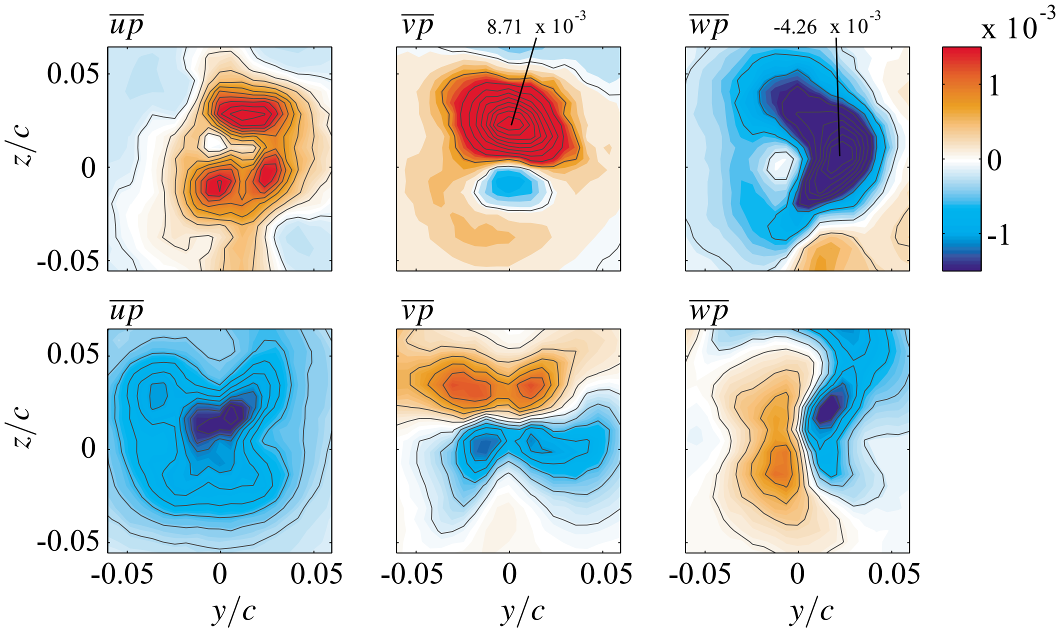

Figure 5.19: Velocity pressure correlation $\overline{up}$, $\overline{vp}$ and $\overline{wp}$ measured by the SP- and X-probes (top), measured by the TP- and X-probes (bottom).

location. The samples that achieve $\hat{v} \simeq \hat{w} \simeq 0$ are called "zero-crossing samples". Figure 5.20 shows the distribution of probability of these particular samples. The contour line showing the probability 0.32% is elliptical in shape measuring 4.7 mm in the y direction and 6.6 mm in the z direction.

The elongated shape of the joint probability density function of the zero-crossing-samples can be associated with the vortex meandering in the z direction. Heyes et al. (2004) indicated that the distributions of the Reynolds stress were entirely subject to the meandering. The statistical feature of the wing-tip vortex observed here such as the large $\overline{v^2}$ among the Reynolds stress normal components shown in Fig. 5.16 and the multiple peaks of the static pressure fluctuation in Fig. 5.17 can also be related to the vortex meandering.

The diffusion terms in the transport equation of the turbulent kinetic energy are evaluated. Here, it is reasonable to assume that the streamwise gradient $\partial/\partial x$ is suffi-

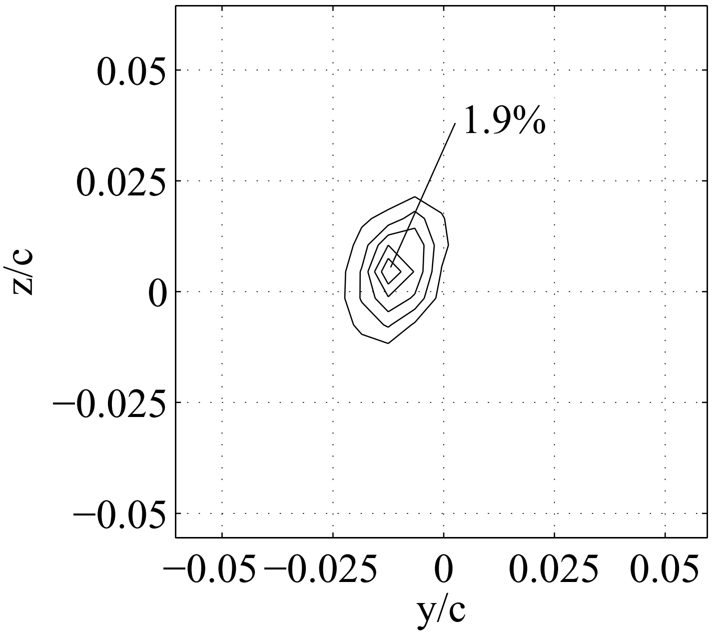

Figure 5.20: PDF of zero-crossing samples.

ciently small compared to the gradient in the cross stream directions $\partial/\partial y$ and $\partial/\partial z$; therefore, the turbulent- and pressure-diffusion terms are calculated as follows:

$$D^k{}_t \simeq -\frac{1}{2}\left(\frac{\partial \overline{u^2 v}}{\partial y}+\frac{\partial \overline{v^3}}{\partial y}+\frac{\partial \overline{vw^2}}{\partial y}+\frac{\partial \overline{u^2 w}}{\partial z}+\frac{\partial \overline{v^2 w}}{\partial z}+\frac{\partial \overline{w^3}}{\partial z}\right), \tag{5.1}$$

$$D^k{}_p \simeq -\frac{1}{\rho}\left(\frac{\partial \overline{vp}}{\partial y}+\frac{\partial \overline{wp}}{\partial z}\right). \tag{5.2}$$

Figure 5.21 shows the distribution of the turbulent- and the pressure-diffusion terms D^k_t and D^k_p. The origin of the coordinate is adjusted to the vortex center where the time-averaged circumferential velocity takes the minimum ($\sqrt{V^2+W^2} \simeq 0$). The magnitude of two diffusion terms is comparable, and the pressure-diffusion contributes over a broader range compared to the turbulent-diffusion. These terms are plotted in the y and z directions through the vortex center in Fig. 5.22(a) and (b), respectively. In Fig. 5.22(a), the turbulent- and pressure-diffusion terms take opposite signs from each other. On the other hand, along the other direction z, the pressure-diffusion term takes a similar distribution to the turbulent diffusion term as shown in Fig. 5.22(b).

It is believed that the pressure-diffusion term is negligibly small except very near the wall and the pressure-diffusion term is modeled as the counterpart of the turbulent-

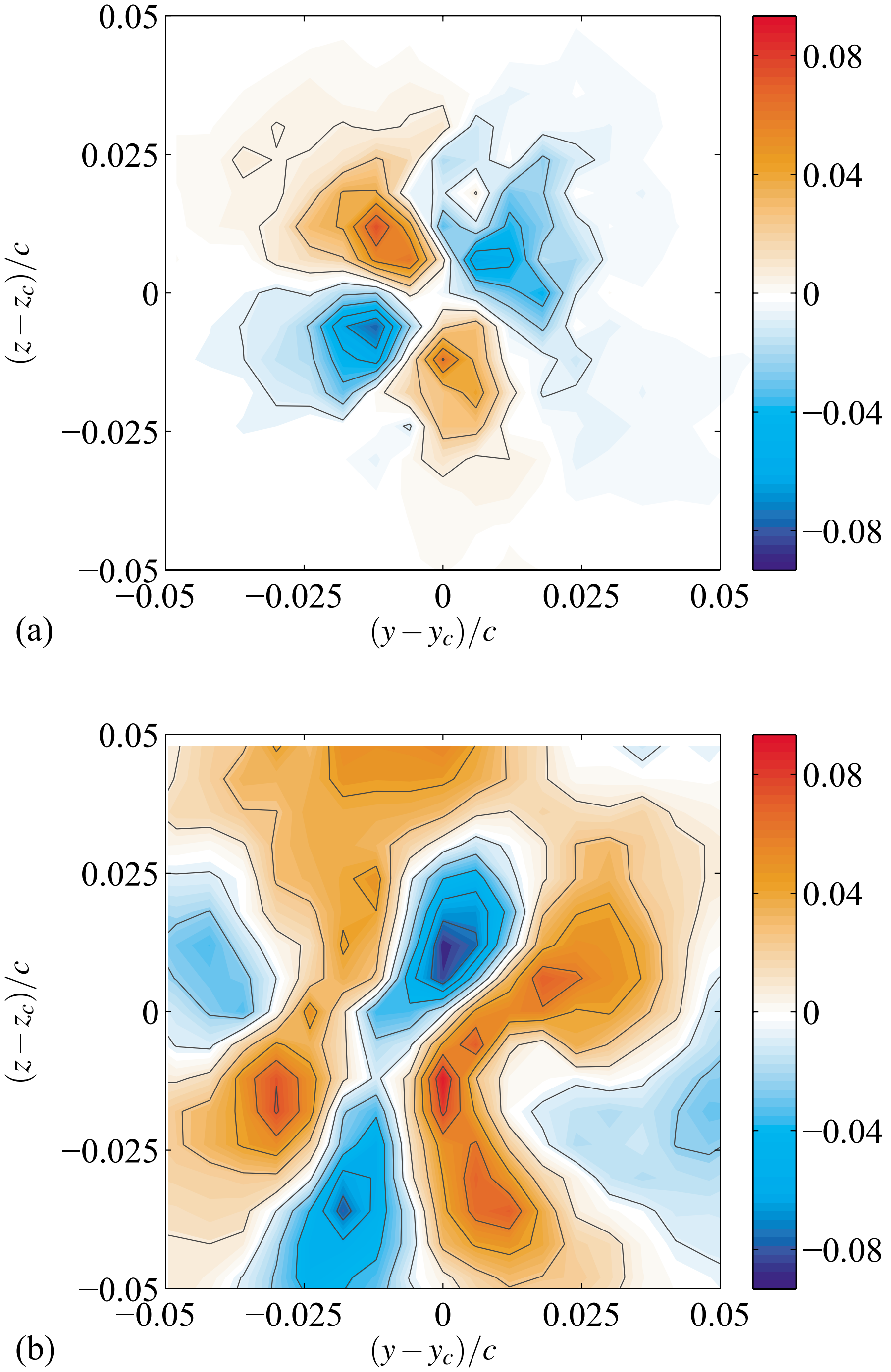

Figure 5.21: Contour plot of the diffusion terms; (a) the turbulent-diffusion, (b) the pressure-diffusion.

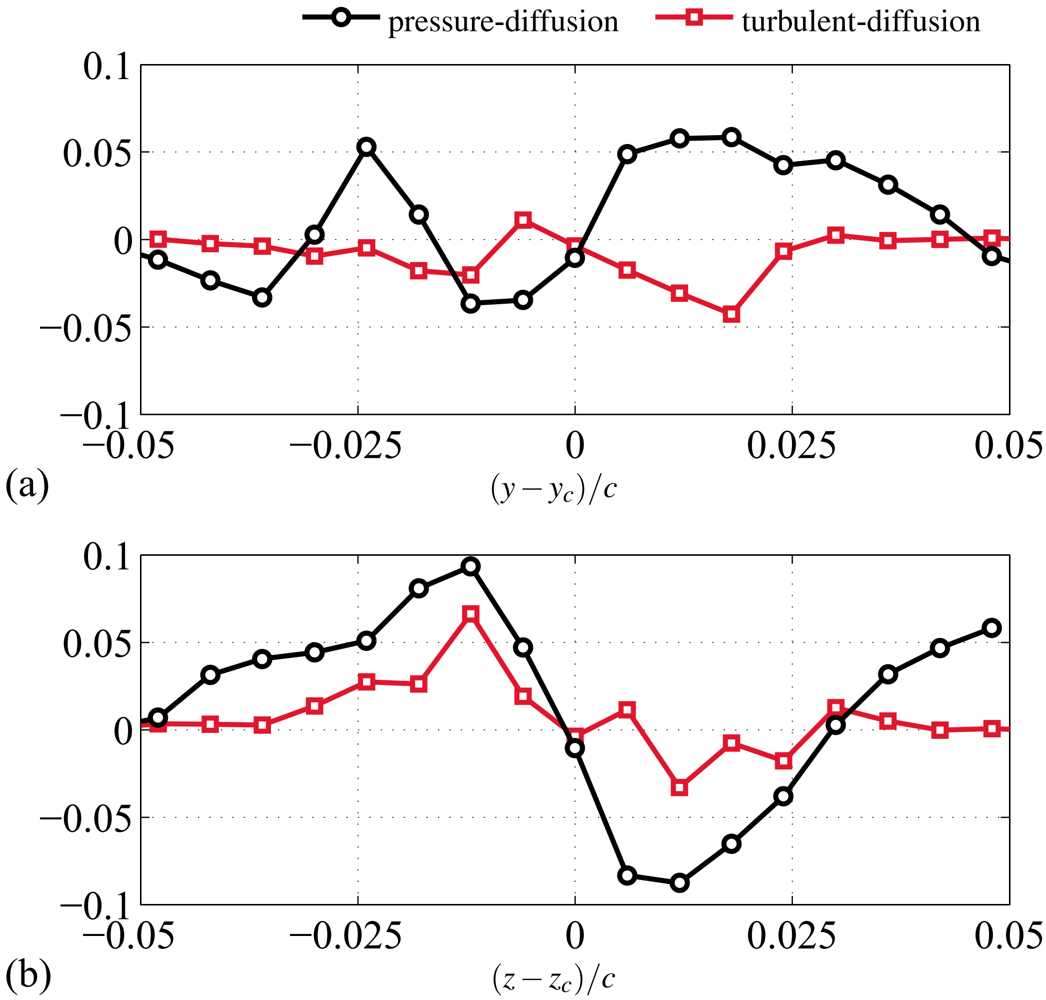

Figure 5.22: Line-plot of turbulent- and pressure-diffusion terms; (a) in y-direction, (b) in z-direction.

diffusion in the simple shear flow as in model proposed by Lumley (1978). However, such a relationship may be violated in a non-equilibrium flow and especially with the contribution of the large vortices such as the wing-tip vortex. As shown in Fig. 5.22(a) and (b), the relationship between the turbulent- and pressure-diffusion terms reflects the unsteady motion of the wing-tip vortex. In order to fully understand the mechanism of the link between the dynamics of the vortex and the statistical features of turbulence properties such as the diffusion terms, the time-resolved orbit of the vortex, which can be examined by the high-repetition rate stereo PIV measurement, must be obtained

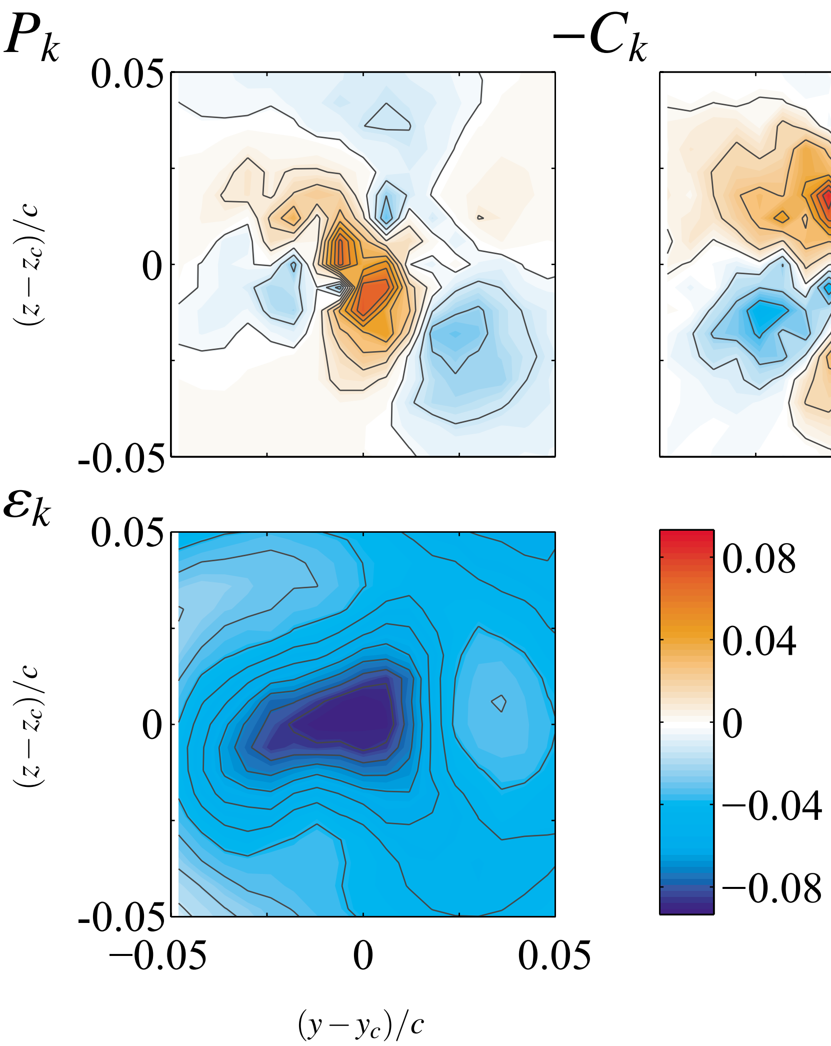

Figure 5.23: Contour of the production, convection and dissipation terms.

simultaneously with fluctuating pressure.

In Fig. 5.23, other terms in the transport equation of the turbulent kinetic energy, e.g. the production, convection and dissipation terms are estimated using following equations:

$$P_k \simeq -\left(\frac{\partial V}{\partial x}\overline{uv} + \frac{\partial V}{\partial y}\overline{v^2} + \frac{\partial W}{\partial y}\overline{vw} + \frac{\partial W}{\partial x}\overline{uw} + \frac{\partial W}{\partial y}\overline{vw} + \frac{\partial W}{\partial z}\overline{w^2}\right), \tag{5.3}$$

$$-C_k \simeq V\frac{\partial k}{\partial y} + W\frac{\partial k}{\partial z}, \tag{5.4}$$

$$\begin{aligned}
\varepsilon_k \simeq -\nu \Bigg[& \overline{\left(\frac{\partial u}{\partial x}\right)^2} + \overline{\left(\frac{\partial v}{\partial x}\right)\left(\frac{\partial u}{\partial y}\right)} + \overline{\left(\frac{\partial w}{\partial x}\right)\left(\frac{\partial u}{\partial z}\right)} \\
& + \overline{\left(\frac{\partial u}{\partial y}\right)\left(\frac{\partial v}{\partial x}\right)} + \overline{\left(\frac{\partial v}{\partial y}\right)^2} + \overline{\left(\frac{\partial w}{\partial y}\right)\left(\frac{\partial v}{\partial z}\right)} \\
& + \overline{\left(\frac{\partial u}{\partial z}\right)\left(\frac{\partial w}{\partial x}\right)} + \overline{\left(\frac{\partial v}{\partial z}\right)\left(\frac{\partial w}{\partial y}\right)} + \overline{\left(\frac{\partial w}{\partial z}\right)^2} \Bigg], \qquad (5.5)
\end{aligned}$$

$$\sim -15\nu \overline{\left(\frac{\partial u}{\partial x}\right)}, \qquad (5.6)$$

$$\sim -15\nu \overline{\left(\frac{\partial u}{\partial t}\right)} / U_\infty{}^2. \qquad (5.7)$$

The streamwise gradient of the time-averaged quantities was not taken into account here same as the estimation of D_p^k and D_t^k.

In addition, the velocity fluctuation was band-pass filtered with its passing frequency from 500 Hz to 600 Hz for the estimation of the dissipation term ε_k. This frequency range was determined from the inverse of the Taylor micro scale, which is approximately 2 ms. It should be noted that the residual of the budget is the same order of terms estimated here.

About the balance of the turbulent kinetic energy shown in Figs. 5.21 and 5.23, the pressure diffusion term is not balanced only with the turbulent diffusion term, and the magnitude of the pressure-diffusion term is comparable to other terms. In order to facilitate a discussion in quantitative point of view, further improvements for the reliability of results are necessary.

5.3 Summary

The combination of the TP- and X-probes has been tested in the wing-tip vortex flow, the probe interference effect on the X-probe can be reduced by using the TP-probe in comparison with the SP-probe. The distribution of static pressure fluctuation shows similar results by both methods. The velocity-pressure correlation, $\overline{vp}$ and $\overline{wp}$, exhibits a qualitatively similar profile, though the distribution of $\overline{up}$ is remarkably different. Further considerations are necessary to improve the performance of these techniques particularly in the flow with large angles of attack.

We have made an attempt to evaluate the turbulent- and pressure-diffusion terms in the transport equation of the turbulent kinetic energy. The two diffusion terms give similar distributions when they are plotted in the z-direction (along direction vortex movement). On the other hand, each diffusion term gives the opposite sign to the other when plotted in the y-direction. The present experimental observations indicate that the relationship between the turbulent- and the pressure-diffusion terms is changed by the unsteady motion of the large vortex.

Chapter 6

Summary and conclusion

In the series of work presented in this thesis, the techniques for the simultaneous measurement of fluctuating velocity and pressure have been developed. The measurements have been carried out in the turbulent mixing layer and the wing-tip vortex as the test cases of simple and complex free shear flows, respectively. Here, the important findings and major contributions of the present study will be summarized.

6.1 Achievements

6.1.1 Measurement techniques

Techniques for the simultaneous measurements of fluctuating velocity and pressure have been developed by two different combinations of probes for the velocity and pressure measurements: either a total pressure probe (TP-probe) or a static pressure probe (SP-probe) is combined with an X-type hot-wire probe (X-probe). Fundamental performances of these techniques such as the yaw-angle performance, the frequency response and the effect of the probe proximity and the spatial resolution, have carefully been checked.

- The yaw-angle performance of the SP- and TP-probes are ±7.5% and ±2%, respectively, at 20°of the yaw-angle.
- The phase-delays of the pressure signal arising from both the response of the air inside of the probe and the electric circuit of the condenser microphone are identified and successfully corrected.

- The effect of the probe interference is experimentally investigated. The distances between the velocity and pressure probes are determined for achieving both as small interference as possible, and as good correlation as possible.

6.1.2 Measurement in the turbulent mixing layer

The simultaneous measurement of fluctuating velocity and pressure was performed in the developing region of a turbulent mixing layer. The development of the fundamental statistics indicated the rapid transition from the two parallel turbulent boundary layers to a turbulent mixing layer. The balance of the transport equation of the Reynolds stress was evaluated. The directly measured pressure-related statistics show in good agreement with the available DNS result under the similar condition. The present experimental results show the analogy between the turbulent diffusion and pressure diffusion in the self-similar region of the mixing layer. On the other hand, such relationship does not seem to hold in the region where the turbulence structure departs from that in the energy equilibrium state.

The results obtained by the combination of the TP- and X-probes presented the satisfactory agreement with the result with the SP- and X-probes in the developing region of the mixing layer. The TP-probe provides consistently larger value for the velocity-pressure correlation than that of the SP-probe in the developing region, which is considered as favorable consequence of the improvement in spatial resolution.

6.1.3 Measurement in the wing-tip vortex

Simultaneous measurements of fluctuating velocity and pressure were conducted in the wing-tip vortex trailing from a NACA 0012 wing. It is shown that the TP-probe can reduce the effect of the probe interference existing in the case of the SP-probe. The present experimental observations indicate that the meandering of the vortex grows in the downstream direction and that the transverse velocity fluctuation increases in the vortex core. The peaks of pressure fluctuation appear slightly off center in the vortex and become clear further downstream. The PSD of transverse velocity fluctuation indicates that the vortex meandering occurs in the lower frequency range.

The profiles of the velocity-pressure correlation $\overline{up}$, $\overline{vp}$ and $\overline{wp}$ show distinct peaks near the vortex center. The significant gradient of the velocity-pressure correlation can be attributed to a contribution of the velocity-pressure correlation to the balance of turbulence properties.

The combination of the TP- and X-probes has been tested in the wing-tip vortex flow. The static pressure fluctuation measured by two methods, i.e., using the SP- or TP-probes, agree well with each other. The velocity-pressure correlation, $\overline{vp}$ and $\overline{wp}$, exhibits a qualitatively similar profile, though the distribution of $\overline{up}$ is remarkably different.

The turbulent- and pressure-diffusion terms in the transport equation of the turbulent kinetic energy are evaluated. The two diffusion terms give similar distributions when they are plotted in the z-direction (along the direction of vortex motion). On the other hand, each diffusion term gives the opposite sign to the other when plotted in the y-direction. The present experimental observations indicate that the relationship between the turbulent- and the pressure-diffusion terms depends on the direction of the unsteady motion of the large vortex.

6.2 Direction for future research

1. Toward the improvement of quantitative reliability, further assessments of techniques presented in the present thesis are necessary:
    - Further investigations on the effect of the spatial resolution;
    - Further assessments of the applicability of Eq. (3.6) calculating the fluctuating static pressure;
    - Efforts to decrease the measurement uncertainty of the total pressure fluctuation and the streamwise mean velocity, which largely contributes to the estimated static pressure fluctuation;
2. The available data of static pressure fluctuations and pressure related statistics are still limited. It is demanded to build the database of the pressure fluctuation in various turbulent flows by means of both experimental and computational approaches.
3. The combination of the SP- and TP-probes with other velocity measurement techniques will bring several benefits.

- The use of LDV in combination with the TP-probe provides accurate estimation of dynamic pressure, and the flow disturbance caused by prongs of hot-wire probe can also be avoided.
- The velocity field measured by PIV will help to understand the relationship between the vortical structure of the turbulent flows and its contribution to pressure fluctuation and the pressure-related statistics.

Appendix A

List of instruments

Table A.1: List of instruments

Name	Manufacturer	Model	Specification
thermometer	Nakamura-Rika-Kogyo	TA-5N	min scale: 1°C
mercury barometer	Shimadzu Seisakusho		Fortin type min scale: 0.1 mmHg, 0.5°C
blowing mixing layer wind tunnel	self-built		FST 1%
blowing wind tunnel	self-built		FST 0.6%
standard Pitot-tube	Okano-Seisakusho	LK-1	coefficient: 1.00
precision pressure difference sensor	Validyne	DP45-18	pressure range: 0-35 mmH_2O
precision pressure difference sensor amplifier	KRONE	PA-501	
constant temperature anemometer (CTA)	Kanomax	1010	
constant temperature anemometer (CTA)	Kanomax	1011	
temperature unit	Kanomax	1020	
I-type hot-wire probe	self-fabricated		tungsten wire:, length: 1.0 mm, diameter: 5μm
I-type hot-wire probe	Kanomax	0251R-T5	
X-type hot-wire probe	Dantec	55P64	
X-type hot-wire probe	Dantec	55P54	
triple hot-film probe	Dantec	55R91	
temperature compensation probe	Kanomax		

Name	Manufacturer	Model	Specification
support for dual sensor probe	Dantec	55H24	
support for triple sensor probe	Dantec	55H27	
traversing mechanism	self-fabricated		for calibration of X-wires probe
static pressure probe	self-fabricated		
total pressure probe	self-fabricated		
condenser microphone	RION	UC-29	Sensitivity: 4.02 mV/Pa, frequency range: 5-100 kHz
conversion Adapter	RION	UA-12	
pre-amp.	RION	NH-05	
main-amp.	RION	UN-04	
traversing unit	self-built		y-direction
low-pass filter	NF corp.	3344	6th order Chevishev
A/D converter board	National Instruments	PCI-MIO-16XE-10	multifunction DAQ board, resolution: 16bit
BNC terminal	National Instruments	BNC-2120	
digital micro scope	Keyence	VH-6200	
USB sound unit	onkyo	SE-30	
loudspeaker	YAMAHA	HS80M	
quasi-anechoic box	self-built		
measurement software	National Instruments	LabView 8™	
signal processing software	MathWorks	Matlab 2008a™	
PC	HPC systems	Rack-Mount PC-500	CPU: Pentium4 2.66GHz, main memory: 1GB

Appendix B

Estimation of combined standard uncertainty

The combined standard uncertainty on calculating the fluctuating pressure using Eq. (3.6) is estimated. Here, the function f_p corresponds to Eq. (3.6):

$$f_p = p_t - \rho U u - \frac{\rho}{2} u^2 + \frac{\rho}{2} \overline{u^2} + \frac{\rho}{2} \frac{du}{dt} \Delta x. \tag{B.1}$$

The derivatives of f_p are calculated as follows:

$$\frac{\partial f_p}{\partial p_t} = 1, \tag{B.2}$$

$$\frac{\partial f_p}{\partial U} = -\rho u, \tag{B.3}$$

$$\frac{\partial f_p}{\partial u} = -\rho U - \rho u, \tag{B.4}$$

$$\frac{\partial f_p}{\partial \overline{u^2}} = \frac{\rho}{2}, \tag{B.5}$$

$$\frac{\partial f_p}{\partial \frac{du}{dt}} = \frac{\rho}{2} \Delta x, \tag{B.6}$$

$$\frac{\partial f_p}{\partial \rho} = -U u - \frac{1}{2} u^2 + \frac{1}{2} \overline{u^2} + \frac{1}{2} \frac{du}{dt} \Delta x, \tag{B.7}$$

$$\frac{\partial f_p}{\partial \Delta x} = \frac{\rho}{2} \frac{du}{dt}. \tag{B.8}$$

The combind standard error:

$$\zeta_c^2 = \left(\frac{\partial f_p}{\partial p_t}\right)^2 \zeta^2(p_t) + \left(\frac{\partial f_p}{\partial U}\right)^2 \zeta^2(U) + \left(\frac{\partial f_p}{\partial u}\right)^2 \zeta^2(u) + \left(\frac{\partial f_p}{\partial \overline{u^2}}\right)^2 \zeta^2(\overline{u^2})$$
$$+ \left(\frac{\partial f_p}{\partial \frac{du}{dt}}\right)^2 \zeta^2\left(\frac{du}{dt}\right) + \left(\frac{\partial f_p}{\partial \rho}\right)^2 \zeta^2(\rho) + \left(\frac{\partial f_p}{\partial \Delta x}\right)^2 \zeta^2(\Delta x), \tag{B.9}$$

where $\zeta(q_i)$ is the uncertainty of the target quantity.

It is demonstrated that the combined standard uncertainty is estimated at the center of the mixing layer at $x = 150$ mm; U =5.5 m/s ±0.9%, u' =0.59 m/s ±0.75% p' =0.79 Pa ±0.6%, ${p_t}'$ =3.38 Pa ±1.5%, ρ =1.2 kg/m^3 ±1%, Δx =1.0 mm ±1%. Hence, ζ_c is calculated using Eq. (B.9) to be 0.073 Pa.

Appendix C

Development of statistics in a wing-tip vortex

Here, the perspective views of statistics in the wing-tip vortex are presented: the Reynolds stress components $\overline{u^2}$, $\overline{v^2}$, $\overline{w^2}$, $\overline{uv}$, $\overline{uw}$ and $\overline{vw}$ are shown in Fig. C.1–C.6; PDF of the zero-crossing samples is shown in Fig. C.7; the rms value of the fluctuating pressure p' is shown in Fig. C.8.

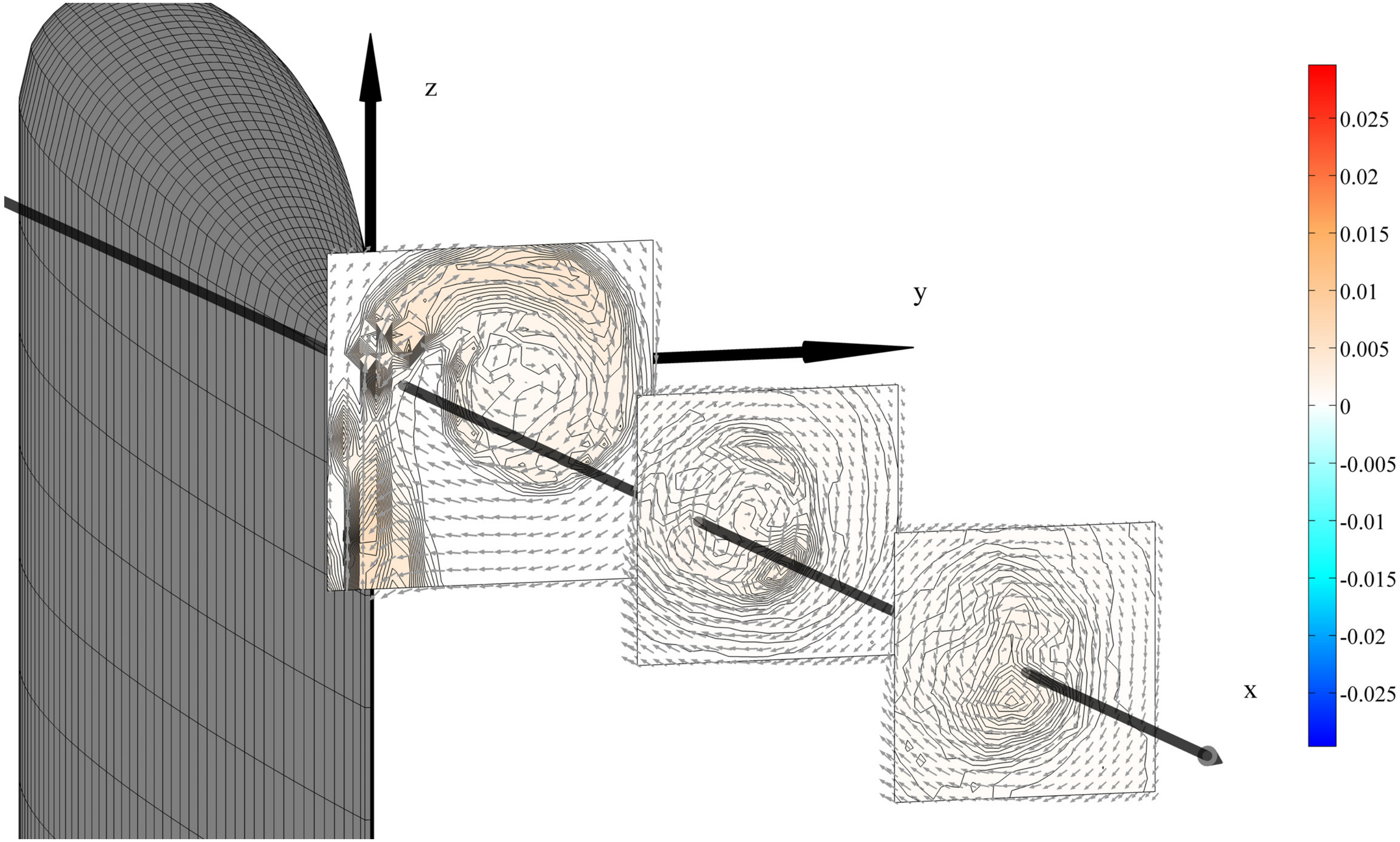

Figure C.1: Perspective view of $\overline{u^2}$.

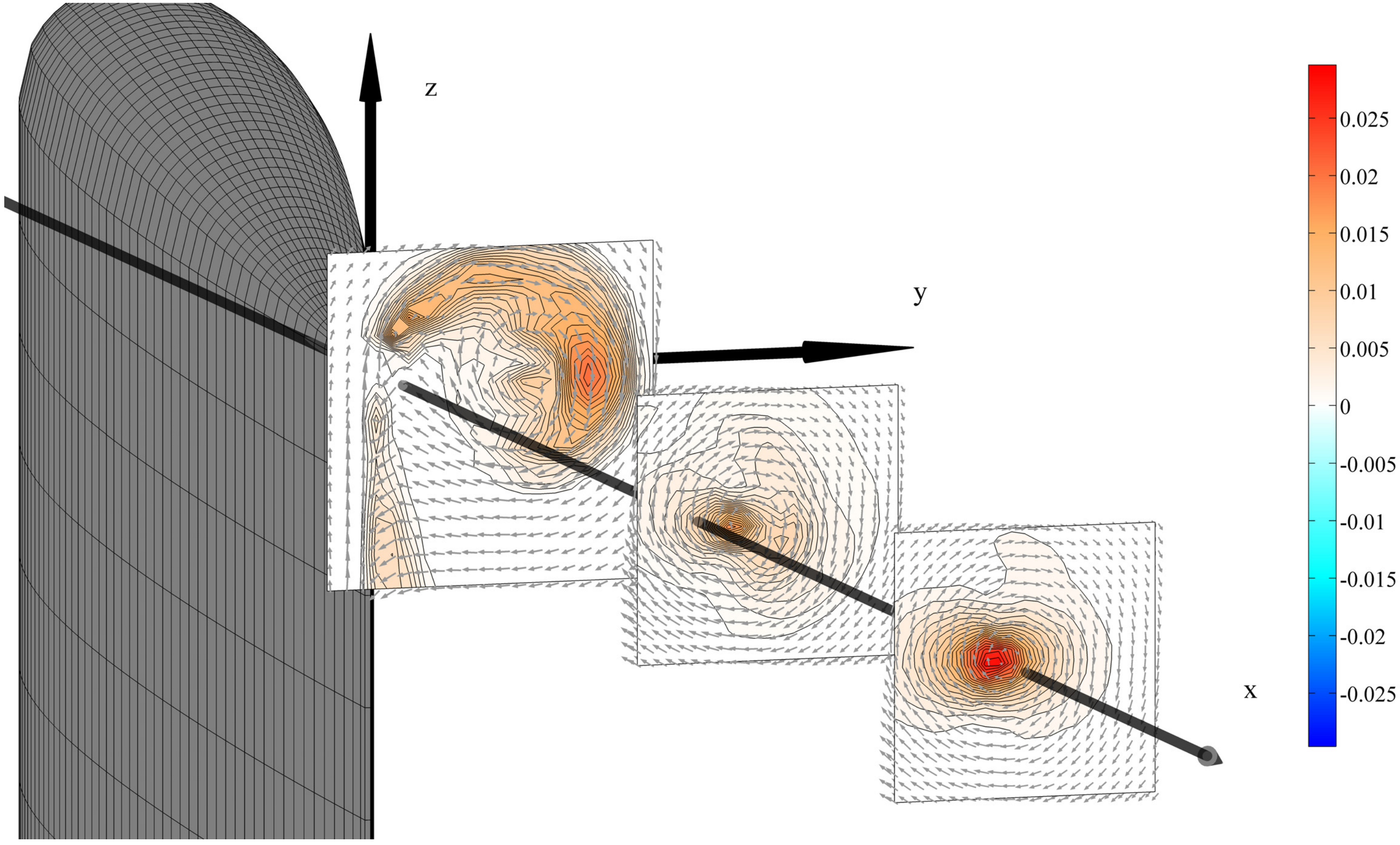

Figure C.2: Perspective view of $\overline{v^2}$.

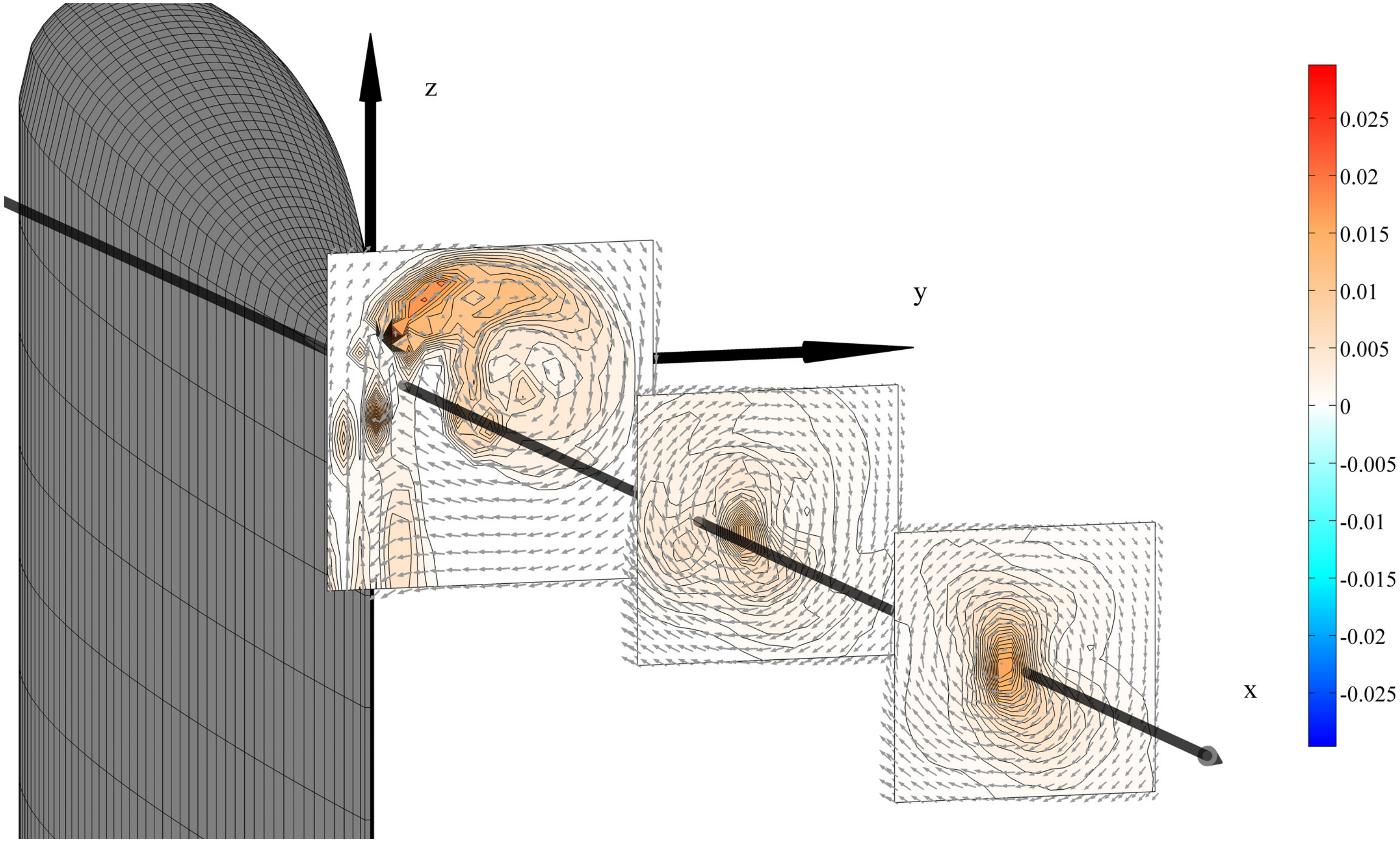

Figure C.3: Perspective view of $\overline{w^2}$.

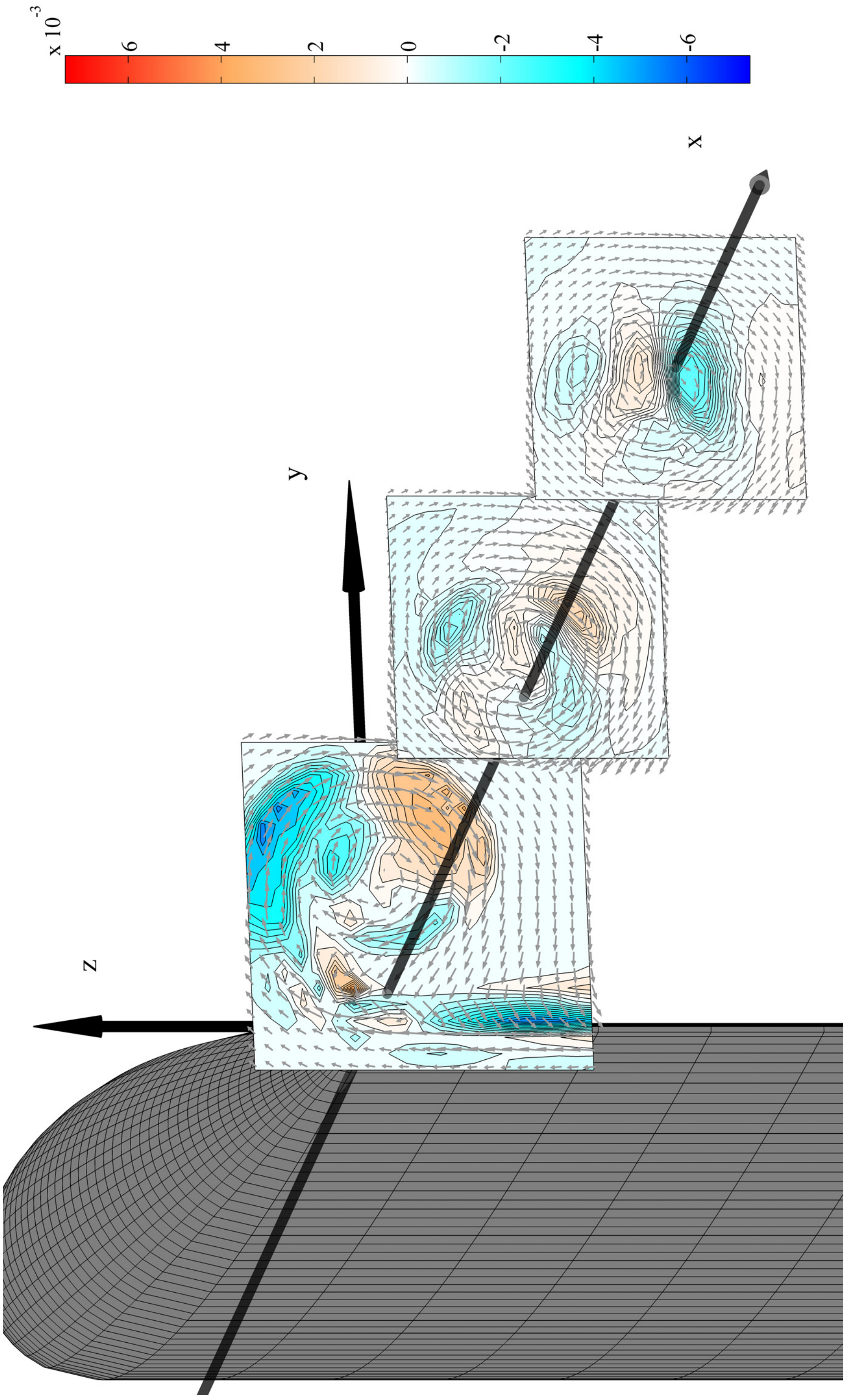

Figure C.4: Perspective view of $\overline{uv}$.

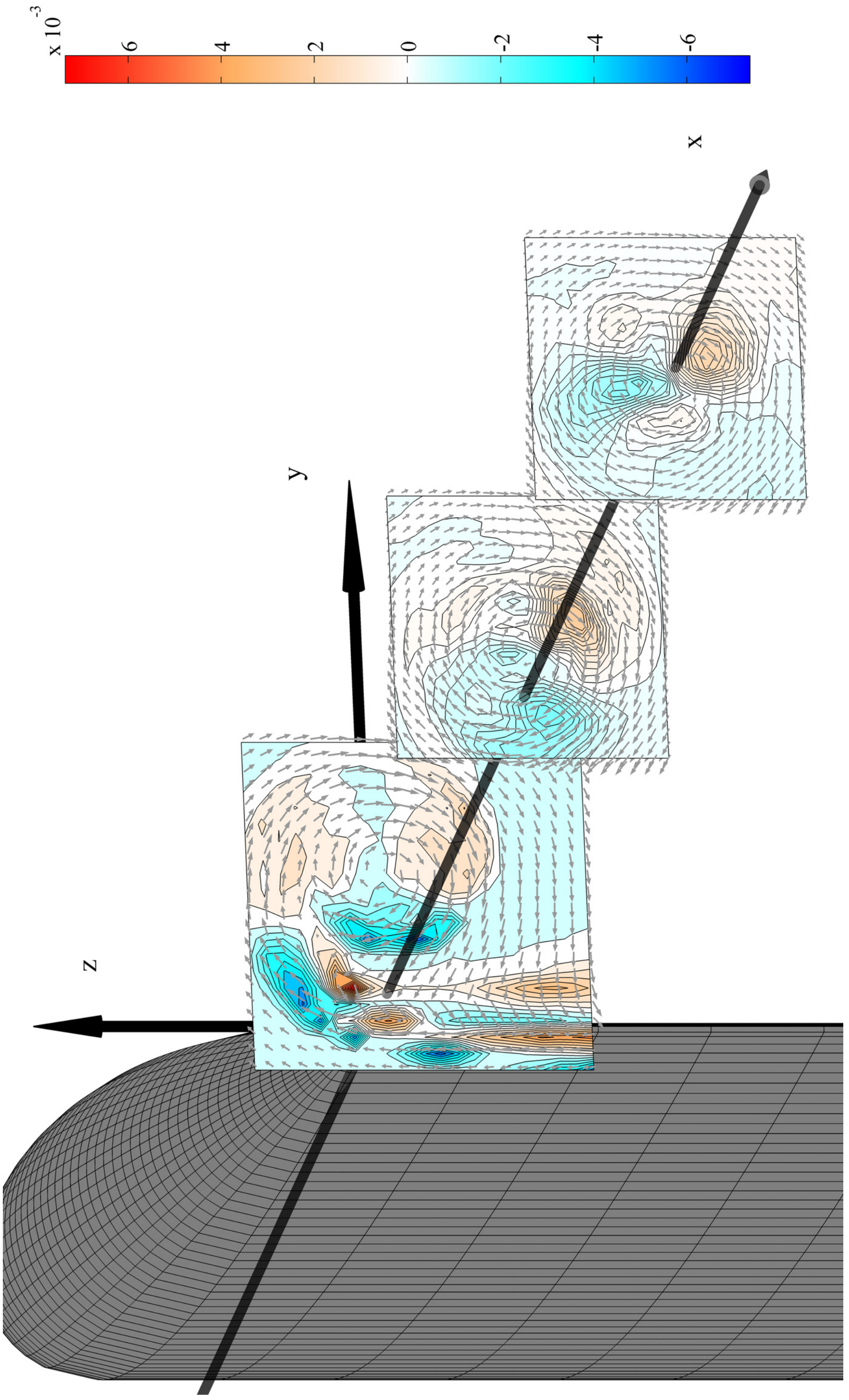

Figure C.5: Perspective view of $\overline{uw}$.

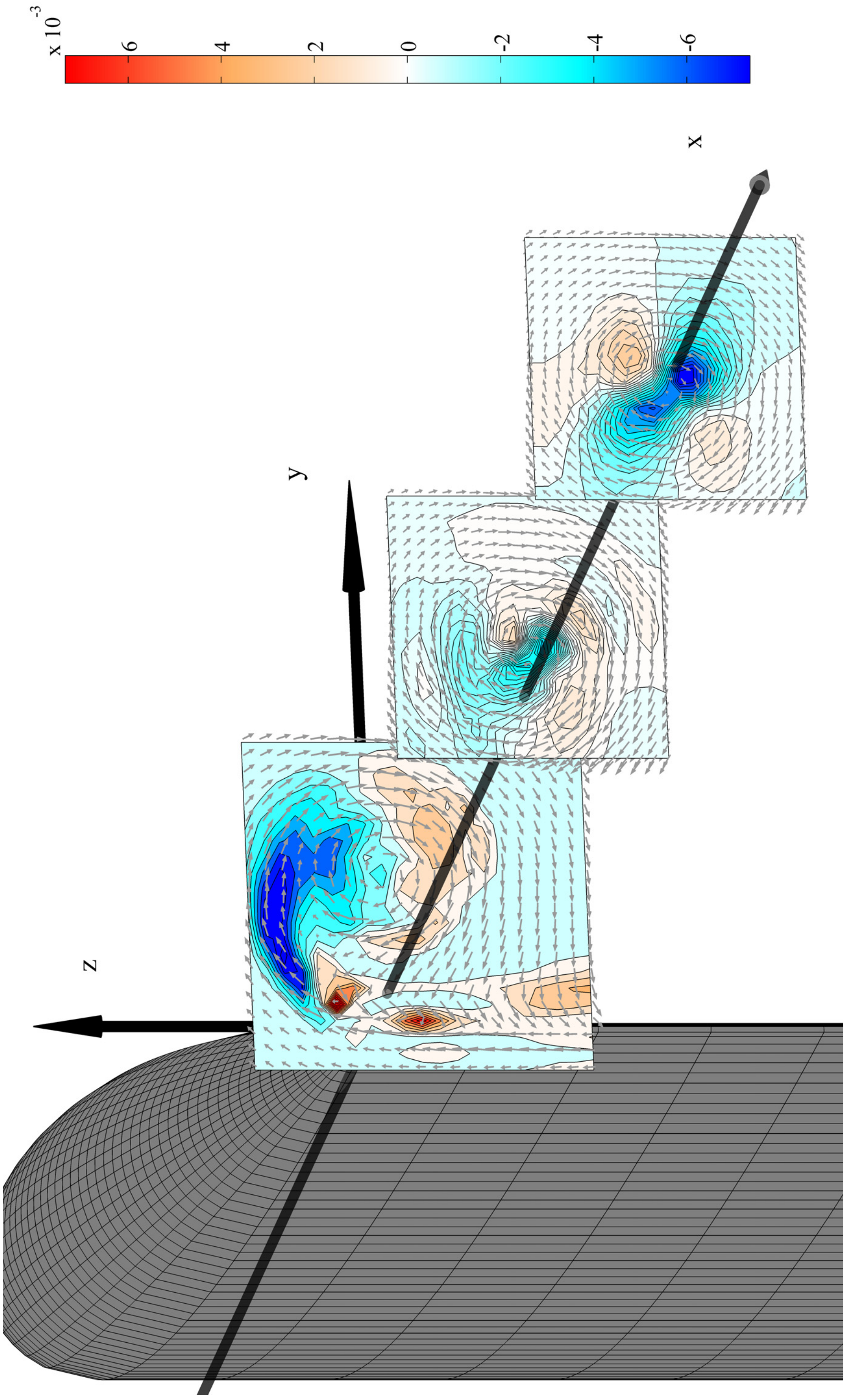

Figure C.6: Perspective view of $\overline{vw}$.

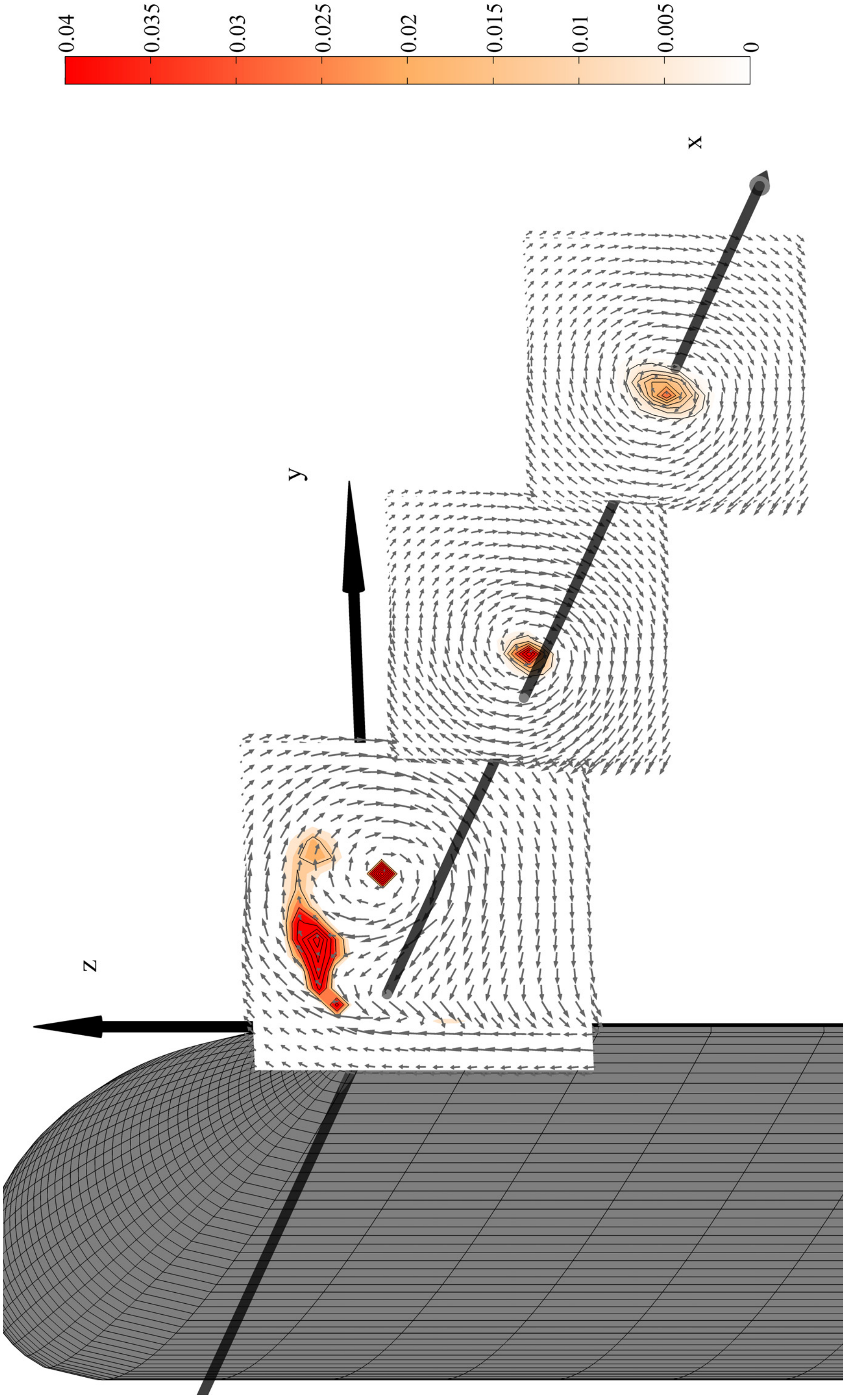

Figure C.7: Perspective view of PDF of zero-crossing samples.

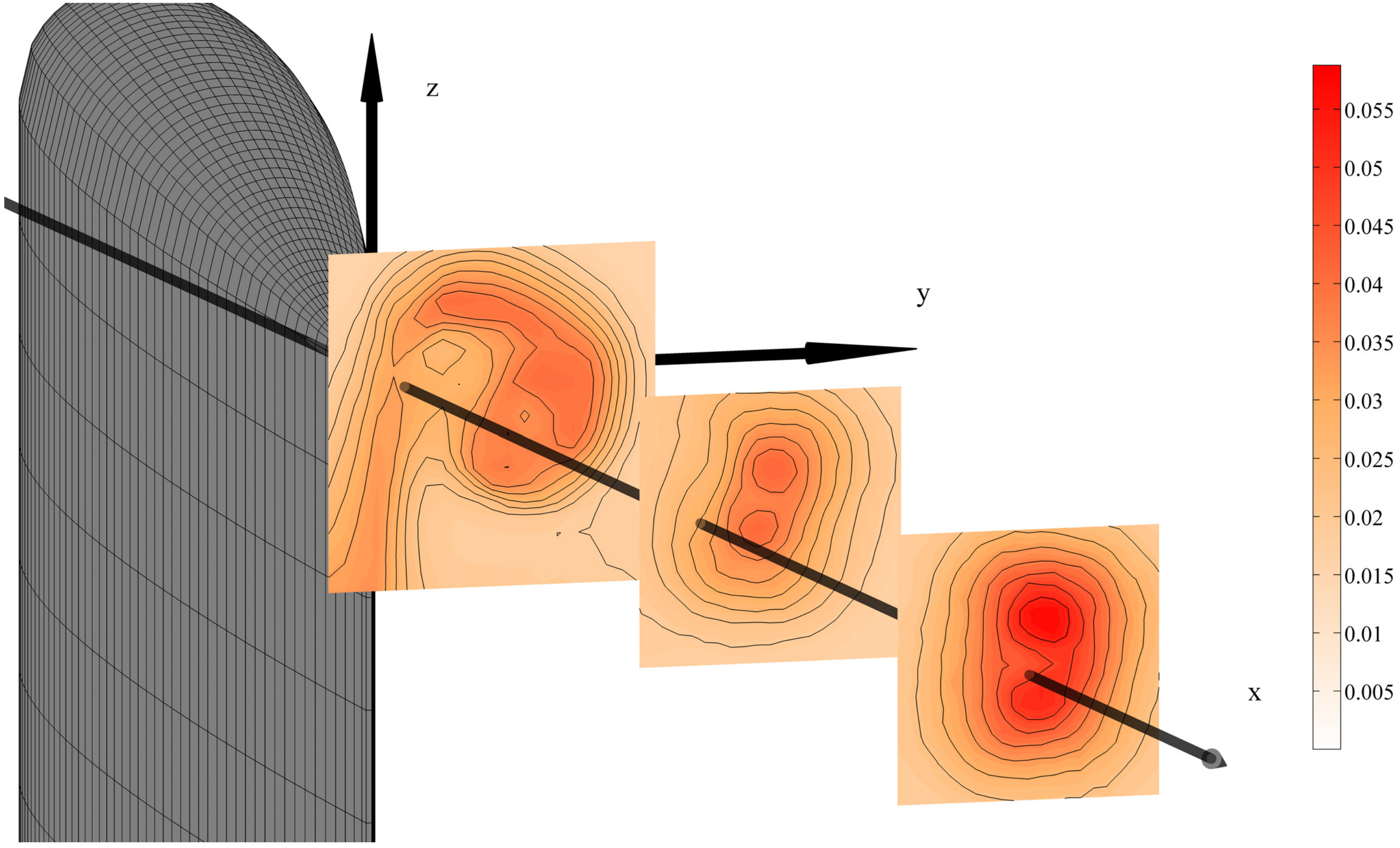

Figure C.8: Perspective view of p'.

Bibliography

Aditjandra, A., Trosin, B. J., Naguib, A. M., 2009. Array measurements of the surface pressure beneath a forced axi-symmetric separation bubble. Exp. in Fluids 46, 297–308. 5

Alvelius, K., Johansson, A. V., 2000. LES computations and comparison with Kolmogorov theory for two-point pressure-velocity correlations and structure functions for globally anisotropic turbulence. J. Fluid Mech. 403, 23–36. 3

Anderson, E., Lawton, T. A., 2003. Correlation between vortex strength and axial velocity in a trailing vortex. J. Aircraft 40, 699–704. 89

Arndt, R. E. A., Nilsen, A. W., 1971. On the measurement of fluctuating pressure in the mixing zone of a round jet. ASME Paper 71-FE, 31. 6

Arndt, R. E. A., Tran, N. C., Barefoot, G. L., 1974. Turbulence and acoustic characteristics of screen perturbed jets. AIAA J. 12, 261–262. 6

ASME PTC 19.1, 1986. Measurement uncertainty. 41

Bailey, S. C. C., Tavoularis, S., 2008. Measurements of the velocity field of a wing-tip vortex, wandering in grid turbulence. J. Fluid Mech. 601, 281–315. 83, 102

Barlow, J. B., Rae, W. H., Pope, A., 1999. Low-Speed Wind Tunnel Testing. Wiley-Interscience. 47

Batchelor, G. K., 1951. Pressure fluctuations in isotropic turbulence. Proc. Cambridge Philos. Soc. 47, 359–374. 2, 80

Batchelor, G. K., 1964. Axial flow in trailing line vortices. J. Fluid Mech. 20, 645–658. 4

Bell, J. H., Mehta, R. D., 1990. Development of a two-stream mixing layer from tripped and untripped boundary layers. AIAA Journal 28, 2034–2042. 3, 55

Bendat, J. S., Piersol, A. G., 2000. Random Data, 3rd Edition. John Wiley & Sons, Inc. 69

Bergh, H., Tijdeman, H., 1965. Theoretical and experimental results for the dynamic response of pressure measuring systems. Tech. Rep. F.238, NLR-TR. 21

Bradshaw, P., 1978. Topics in applied physics 12 Turbulence. Springer Verlag. xi, 16, 17

Braud, C., Heitz, D., Arroyo, G., Perret, L., Delville, J., Bonnet, J.-P., 2004. Low-dimensional analysis, using POD, for two mixing layer-wake interactions. Int. J. Heat and Fluid Flow 25, 351–363. 3

Brown, G. L., Roshko, A., 1974. On density effects and large structure in turbulent mixing layers. J. Fluid Mech. 64, 775–816. 3

Browne, L. W. B., Antonia, R. A., Chua, L. P., 1989. Calibration of X-probes for turbulent flow measurements. Exp. in Fluids 7, 201–208. 33, 73, 86

Bruun, H. H., 1995. Hot-Wire Anemometry: Principles and Signal Analysis. Oxford University Press. 33

Cantwell, B. J., 1981. Organized motion in turbulent flow. Annual Review of Fluid Mechanics 13, 457–515. 3

Chigier, N. A., Corsiglia, V. R., 1971. Tip vortices - velocity distributions. Tech. rep., NASA TM X-62.087. 4

Chow, J., Zilliac, G., Bradshaw, P., 1997. Turbulence measurements in the near field of a wingtip vortex. Tech. rep., NASA Technical Memorandum, 110418. 4, 89

Craft, T., Gerasimov, A., Launder, B., Robinson, C., 2006. A computational study of the near-field generation and decay of wingtip vortices. Int. J. Heat and Fluid Flow 27, 684–695. 4

Dejoan, A., Leschziner, M., JUN 2006. Separating the effects of wall blocking and near-wall shear in the interaction between the wall and the free shear layer in a wall jet. Phys. Fluids 18 (6), 065110. 4

Dejoan, A., Wang, C., Leschziner, M. A., NOV 2006. Assessment of turbulence models for predicting the interaction region in a wall jet by reference to les solution and budgets. Flow Turbulence and Combustion 77 (1-4), 229–255. 4

Devenport, W. J., Rife, M. C., Stergios, I. L., Follin, G. J., 1996. The structure and development of a wing-tip vortex. J. Fluid Mech. 312, 67–106. 83

Dimotakis, P. E., Brown, G. L., 1976. The mixing layer at high Reynolds number: large-structure dyamics and entrainment. J. Fluid Mech. 78, 535–560. 3

Durbin, P. A., 1993. A reynolds stress model for near-wall turbulence. J. Fluid Mech 249, 465–498. 18

Durbin, P. A., Reif, B. A. P., 2001. Statistical Theory and Modeling for Turbulent Flows. John Wiley & Sons Inc. 5

Dziomba, B., Fiedler, H. E., 1985. Effect of initial conditions on two-dimensional free shear layers. J. Fluid Mech. 152, 419–442. 3

Eckelmann, H., 1989. A review of knowledge on pressure fluctuations. Hemisphere, New York. 5

Elliot, J. A., 1972. Micro scale pressure fluctuations measured within the lower atmospheric boundary layer. J. Fluid Mech. 3, 351–383. 7, 11

Fuchs, H. V., 1970. Uber die messung von druck-schwankungen mit umstromten mikrofonen in freistrahl. Tech. rep., DFVLR Tech. Rep. DLR-FB70-22. 6

Fuchs, H. V., 1972. Measurement of pressure fluctuations within subsonic turbulent jets. J. Sound Vib. 22, 361–378. 5, 6

George, W. K., Beuther, P. D., Arndt, R. E. A., 1984. Pressure spectra in turbulent free shear flows. J. Fluid Mech. 148, 155–191. 5, 7, 11

Giovanangeli, J.-P., 1988. A new method for measuring static pressure fluctuations with application to wind-wave interaction. Exp. in Fluids 6, 156–164. 7, 10, 73

Gotoh, T., Fukayama, D., 2001. Pressure spectrum in homogeneous turbulence. Physical Review Letters 86, 3775–3778. 3

Gotoh, T., Nakano, T., 2003. Role of pressure in turbulence. Journal of Statistical Physics Journal of Statistical Physics, 855–874. 3

Gotoh, T., Rogallo, R., 1999. Intermittency and scaling of pressure at small scales in forced isotropic turbulence. J. Fluid Mech. 396, 257–285. 2

Green, S. I., Acosta, A. J., 1991. Unsteady flow in trailing vortices. J. Fluid Mech 227, 107–134. 4

Guo, Y., Wood, D. H., 2001. Instantaneous velocity and pressure measurements in turbulent mixing layers. Exp. Themal Fluid Sci. 24, 139–150. 7

Gylfason, A., Ayyalasomayajula, S., Warhaft, Z., 2004. Intermittency, pressure and acceleration statistics from hot-wire measurements in wind-tunnel turbulence. J. Fluid Mech. 501, 213–229. 2

Hanjalić, K., Launder, B. E., 1972. A reynolds stress model of turbulence and its application to thin shear flows. J. Fluid Mech 52, 609–638. 16

Hayes, M. H., 1996. Statistical Digital Signal Processing And Modeling. John Wiley & Sons, Inc. 32

Herpin, S., Wong, C. Y., Stanislas, M., Soria, J., 2008. Stereoscopic piv measurements of a turbulent boundary layer with a large spatial dynamic range. Exp. in Fluids 45, 745–763. 9

Heyes, A. L., Jones, R. F., Smith, D. A. R., 2004. Wandering of wing-tip vortices. In: Proc. of 12th Intl Symp. on the Applications of Laser Techniques to Fluid Mechanics, Lisbon, Portugal. 83, 103

Hinze, 1975. Turbulence, 2nd Edition. McGraw-Hill Companies. 2, 80

Ho, C. M., Huerre, P., 1984. Perturbed free shear layers. Annual Review of Fluid Mechanics 16, 365–424. 3

Huang, L. S., Ho, C. M., 1990. Small-scale transition in a plane mixing layer. J. Fluid Mech. 210, 475–500. 3

Hudy, L. M., Naguib, A., Humphreys, W. M., FEB 2007. Stochastic estimation of a separated-flow field using wall-pressure-array measurements. Phys. Fluids 19 (2), 024103. 5

Hussain, A. K. M. F., 1983. Coherent structures - reality and myth. Phys. Fluids 26, 2816–2850. 3

Hussain, A. K. M. F., Zaman, K. B. M. Q., 1985. An experimental study of organized motions in the turbulent plane mixing layer. J. Fluid Mech. 159, 85–104. 3

Iida, A., Ootaguro, T., Kato, C., Shimode, S., 1999. Analysis of aerodynamic sound source with measurement of static pressure fluctuation. JSME International Journal, Series B 42-4, 596–604. 8

Ishii, T., Alexandre, S., Obi, S., 2008. The pressure-velocity correlation in the turbulent wingtip vortex flow. In: Proc. 7th JSME-KSME Thermal and Fluids Engineering Conference. 8

ISO GUM, October 1993. Guide to the expression of uncertainty in measurement: Gum. 41

Johansen, E. S., Rediniotis, O. K., 2005a. Unsteady calibration of fast-response pressure probes, part 1: Theoretical studies. AIAA J. 43, 816–826. 8

Johansen, E. S., Rediniotis, O. K., 2005b. Unsteady calibration of fast-response pressure probes, part 2: Water-tunnel experiments. AIAA J. 43, 827–834. 8

Johansen, E. S., Rediniotis, O. K., 2005c. Unsteady calibration of fast-response pressure probes, part 3: Air-jet experiments. AIAA J. 43, 835–845. 8, 11

Johansson, P. S., Andersson, H. I., 2005. Direct numerical simulation of two opposing wall jets. Physics of Fluids 17 (5), 055109. 4

Jørgensen, F. E., 2002. How to measure turbulence with hot-wire anemometers - a practical guide. DANTEC Dynamics. 33

Kim, J., 1989. On the structure of pressure fluctuations in simulated turbulent channel flow. J. Fluid Mech. 205, 421–451. 4, 76

Kline, S. J., Reynolds, W. C., Schraub, F. A., Runstadler, P. W., 1967. The structure of turbulent boundary layers. J. Fluid Mech. 30, 741–773. 3

Kobashi, Y., 1957. Measurement of pressure fluctuation in the wake of cylinder. J. Phys. Soc. Jpn 12-5, 533–543. 6, 8, 11, 50

Kobashi, Y., Kono, N., Nishi, T., 1960. Improvements of a pressure pickup for the measurements of turbulence characteristics. J. Aerospace Sci. 27, 149–151. 6

Launder, B. E., Reece, G. J., Rodi, W., 1975. Progress in the development of a reynolds stress turbulence closure. J. Fluid Mech. 68, 537–566. 18

Launder, B. E., Sandham, N. D., 2002. Closure Strategies for Turbulent and Transitional Flows. Cambridge University Press. 5

Le, H., Moin, P., Kim, J., 1997. Direct numerical simulation of turbulent flow over a backward-facing step. J. Fluid Mech. 330, 349–374. 4

Lee, I., Sung, H. J., 2002. Multiple-arrayed pressure measurement for investigation of the unsteady flow structure of a reattaching shear layer. J. Fluid Mech. 463, 377–402. 5

Liu, X., Katz, J., 2006. Instantaneous pressure and material acceleration measurements using a four-exposure piv system. Exp. in Fluids 41, 227–240. 8

Lueptow, R. M., Breuer, K. S., Haritonidis, J. H., 1988. Computeraided calibration of X-probes using a look-up table. Exp. in Fluids 6, 115–118. 33, 73

Lumley, J. L., 1978. Computational modeling of turbulent flows. Advances in Applied Mechanics 18, 123–176. 18, 60, 63, 106

Michalke, A., Fuchs, H. V., 1975. On turbulence and noise of an axisymmetric shear flow. J .Fluid Mech. 70, 179–205. 6

Miksad, R. W., 1976. Omni-directional static pressure probe. J. Appl. Met. 15, 1215–1225. 7

Moin, P., 2001. Fundamentals of Engineering Numerical Analysis. Cambridge University Press. 35

Murai, Y., Nakada, T., Suzuki, T., Yamamoto, F., 2007. Particle tracking velocimetry applied to estimate the pressure field around a savonius turbine. Meas. Sci. Technol. 18, 2491–2503. 8

Nagano, Y., Tagawa, M., 1990. A structural turbulence model for triple products of velocity and scalar. J. Fluid Mech 215, 639–657. 18

Naguib, A. M., Gravante, S. P., Wark, C. E., 1996. Extraction of turbulent wall-pressure time-series using an optimal filtering scheme. Exp. in Fluids 22, 14–22. 30

Nasseri, M., Nitsche, W., 1991. A probe for measuring pressure fluctuations in flows. In: Proc. Instrumentation in Aerospace Simulation Facilities (ICIASF ’91), Rockville, MD. pp. 25–33. 7, 10, 11, 73

Nishiyama, R. T., Bedard, A. J., 1991. A “quad-disc” static pressure probe for measurement in adverse atmospheres: With a comparative review of static pressure probe designs. Rev. Sci. Instrum. 62(9), 2193–2204. 7

Obi, S., Tokai, N., 2006. The pressure-velocity correlation in oscillatory turbulent flow between a pair of bluff bodies. Int. J. Heat and Fluid Flow 27, 768–776. 8

Omori, T., Obi, S., Masuda, S., 2003. Experimental study on velocity-pressure correlation in turbulent mixing layer. In: Proc. the fourth International Symposium on Turbulence, Heat and Mass Transfer (THMT4), Antalya, Turkey. pp. 253–260. 9, 51

Orloff, K. L., 1974. Trailing vortex wind-tunnel diagnostics with a laser velocimeter. Journal of Aircraft 11, 477–482. 4

Planchon, H. P., Jones, B. G., 1974. A study of the local pressure field in turbulent shear flow and its relation to aerodynamic noise generation. In: In Proc. 2nd Interagency Symp. on University. Vol. 1. pp. 21–35. 7

Pope, S. B., 2000. Turbulent flows. Cambridge University Press. 5, 56

Revelly, A., Iaccarino, G., Wu, X., 2006. Advanced rans modeling of wingtip vortex flows. Tech. rep., Center for Turbulence Research. 4

Reynolds, O., 1895. On the dynamical theory of incompressible viscous fluids and the determination of the criterion. Philos. Trans. R. Soc. Ser. A 186, 123–164. 14

Rogers, M. M., Moser, R. D., 1994. Direct simulation of a self-similar turbulent mixing layer. Phys. Fluids 6, 903–923. 3, 51, 57, 63, 72

Rotta, J., 1951. Statistische theorie nichthomogener turbulenz. Z. Phys. 129, 547–572. 17

Rouse, H., 1953. Cavitation in the mixing zone of a submerged jet. Tech. rep., Houille Blanche 8, 9. 6, 11

Rouse, H., 1954. Measurement of velocity and preaaure fluctuations in the turbulent flow of air and water. Tech. rep., Extrait des Memoires sur la Mecanique des Fluides offerts a M. D. Raibouchinsky a L'Occasion de son Jubile Scientifique, Publ. Sci. et Tech. du Ministere de L'Air. 6, 11

Sakai, Y., Moriguchi, Y., Tanaka, N., Yamamoto, M., Kubo, T., Nagata, K., 2007. On characteristics of velocity and pressure field in two-dimensional turbulent jet. Journal of Fluid Science and Technology 2, 611–622. 8

Sami, S., 1967. Balance of turbulence energy in the region of jet-flow establishment. J. Fluid Mech. 29, 81–92. 6

Sami, S., T, C., Rouse, H., 1967. Jet diffusion in the region of flow establishment. J. Fluid Mech. 27, 231–252. 6, 11

Sauret, E., Vallet, I., 2007. Near-wall turbulent pressure diffusion modeling and influence in three-dimensional secondary flows. Journal of Fluids Engineering 129 (5), 634–642. 18

Shir, C., 1973. A preliminary numerical study of atmospheric turbulent flows in the idealized planetary boundary layer. Journal of the Atmospheric Sciences 30, 1327–1339. 16

Shirahama, Y., Toyoda, K., 1993. Development of the probe to measure static-pressure fluctuations. Trans. JSME, Series B 59, 3381–3387. 6, 8, 11

Siddon, T. E., 1969. On the response of pressure measuring instrumentation in unsteady flow. Tech. rep., Univ. Toronto Inst. Aerospace Rep. 136. 6, 7

Spalart, P. R., 1988. Direct simulation of a turbulent boundary layer up to $R_\theta = 1410$. J. Fluid Mech. 187, 61–98. xii, 47, 49

Spencer, B. W., 1970. Statistical investigation of turbulent velocity and pressure fields in a two stream mixing layer. Ph.D. thesis, University of Illinois at Urbana. 7

Spencer, B. W., Jones, B. G., 1971. A bleed-type pressure transducer for in-stream measurement of static pressure fluctuations. Rev. Sci. Instrum. 42, 450–454. 7, 11

Speziale, C. G., Sarker, S., Gatski, T. B., 1991. Modeling the pressure-strain correlation of turbulence: an invariant dynamical systems approach. J. Fluid Mech. 227, 245–272. 18

Strasberg, M., 1963. Measurements of fluctuating static and total head pressure in a tunbulent wake. Tech. rep., NATO AGARD Rept. 464. 6, 11

Strasberg, M., Cooper, R. D., 1965. Measurements of fluctuating pressure and velocity in the wake behind a cylinder. In: Proc. 9th Inst. Cong. Appl. Mech., Brusaels, Belgium. pp. 384–393. 6

Suga, K., 2004. Modeling the rapid part of the pressure-diffusion process in the Reynolds stress transport equation. J. Fluids Eng. 126, 634–641. 19, 72

Tanahashi, M., Hirayama, T., Taka, S., Miyauchi, T., 2008. Measurement of fine scale structure in turbulence by time-resolved dual-plane stereoscopic piv. Int. J. Heat and Fluid Flow 29, 792–802. 3

Taylor, G. I., 1935. Statistical theory of turbulence. iv. diffusion in a turbulent air stream. Proceedings of the Royal Society of London. Series A, Mathematical and Physical Sciences 151, 465–478. 2

Thompson, D. H., 1983. A flow visualization study of tip vortex formation. Tech. rep., Aeronautical Research Labs Melbourne. 4

Toyoda, 2007. Private communication. 23

Toyoda, K., Okamoto, T., Shirahama, Y., 1994. Eduction of vortical structures by pressure measurements in noncircular jets. Applied Scientific Research 53, 237–248. 8, 9, 11, 23, 50, 72, 84

Tropea, C., Yarin, A. L., Foss, J. F., 2007. Springer Handbook of Experimental Fluid Mechanics. Springer. 9

Tsuji, Y., Fransson, J. H. M., Alfredsson, P. H., Johansson, A. V., 2007. Pressure statistics and their scaling in high-Reynolds-number turbulent boundary layers. J. Fluid Mech. 585, 1–40. 8, 11, 51, 72, 80, 84

Tsuji, Y., Ishihara, T., 2003. Similarity scaling of pressure fluctuation in turbulence. Phys. Rev. E 68, 026309. 8, 50, 72, 76, 80, 84

Tsuji, Y., Ishihara, T., October 2006. Pressure statistics in turbulence. In: IUTAM Symposium on Elementary Vortices and Coherent Structures: Significance in Turbulence Dynamics. Springer, Kyoto, pp. 163–170. 80

Uberoi, M. S., 1954. Correlations involvingpressure fluctuations inhomogeneous turbulence. Tech. rep., NACA. 2

Uzun, A., Hussaini, M. Y., Streett, C. L., 2006. Large-eddy simulation of a wing tip vortex on overset grids. AIAA Journal 44, 1229–1242. 4

Wang, Y., Tanahashi, M., Miyauchi, T., 2007. Coherent fine scale eddies in turbulence transition of spatially-developing mixing layer. Int. J. Heat and Fluid Flow 28, 1280–1290. 4

Willmarth, W. W., 1975. Pressure fluctuations beneath turbulent boundary layers. Annual Review of Fluid Mechanics 7 (1), 13–36. 5

Wygnanski, I., Fiedler, H. E., 1970. The two-dimensional mixing region. J. Fluid Mech. 41, 327–361. 3

Yakhot, V., 2003. Pressure-velocity correlations and scaling exponents in turbulence. J. Fluid Mech. 495, 135–143. 3

Yao, Y. F., Thomas, T. G., Sandham, N. D., Williams, J. J. R., 2001. Direct numerical simulation of turbulent flow over a rectangular trailing edge. Theore. Comput. Fluid Dynamics 14, 337–358. 4, 18, 51, 60, 72

Yoshizawa, A., 2002. Statistical analysis of mean-flow effects on the pressure-velocity correlation. Phys. Fluids 14, 1736–1744. 18